EVALUATION OF A DESKTOP COMPUTED RADIOGRAPHY SYSTEM FOR IMRT DOSIMETRY

A Thesis

Submitted to the Graduate Faculty of the
Louisiana State University and
Agricultural and Mechanical College
in partial fulfillment of the
requirements for the degree of
Master of Science in Medical Physics and Health Physics

in

The Department of Physics and Astronomy

by
Ines-Ana Jurkovic
B.S., University of Zagreb, 1992
M.S., University of Zagreb, 1998
December 2004

Acknowledgments

I am deeply thankful to Dr. Oscar Hidalgo-Salvatierra, my major advisor, for the support and encouragement that made this study possible. A special thanks goes to my committee member, Kenneth L. Matthews II, PhD, for the advice and time given me. At several points during my thesis work, Dr. Matthews put my interests as a student ahead of his own. Without his help, these pages would not have been written and my thoughts would never find a way to progress beyond inception. I am exceedingly grateful to Prof. Erno Sajo, for his enormous help, support and encouragement along the way. I thank all of the remaining medical physics faculty, especially Prof. Mark Williams, for giving me a chance to participate in this program, and to all the LSU staff, especially Ms. Yvonne Thomas, who made dreams come true. Special thanks go to Mary Bird Perkins Cancer Center staff, physicians, dosimetrists, therapists and physicists for their contribution and help during my research. In particular, I thank Dr. Johnson, Dr. King, and Dr. Henkelmann, for taking time to answer my questions. I also thank Dan Neck, Angela Stam, Kara Ferachi, and Dr. William Bice for teaching me the practical side of being a medical physicist. I would also like to thank all members of my committee - not only for their time and extreme patience, but also for their intellectual contributions to my development as a scientist. My deepest thanks go to all my friends, colleagues and family for their understandi ng and support. Finally, but not least, I want to thank my

husband Miljenko Markovic, who has endured me during the research, for his constant support and encouragement.

Table of Contents

List of Tables

List of Figures

Abstract

Different techniques have been developed and used to evaluate dose distribution calculation accuracy and dose delivery reproducibility as a part of patient-specific IMRT QA – e.q. film dosimetry, ionization chambers, and diode arrays. To verify that the calculated dose distribution is delivered accurately during treatment, film dosimetry is usually used. The accuracy and reproducibility of film optical density as an indicator of dose is influenced by several variables, including the chemical processing and scanning conditions. This study investigates the possibility to use a desktop computed radiography (CR) system for patient-specific intensity modulated radiation therapy (IMRT) quality assurance (QA).

A study was done at Mary Bird Perkins Cancer Center, Baton Rouge, LA; where phantom IMRT plans are calculated using an ADAC Pinnacle^3 treatment planning system. A Kodak ACR-2000i system is used for the study together with Kodak flexible phosphor screens (plates).

In this study, 778 CR plate exposures were done. Several tests were performed including evaluation of the CR plate response dependency when exposed to changes in either setup or scan conditions.

Calibration curves were generated for three different energies: 4 MV, 6 MV and 10 MV. Using these calibration curves, the CR plates' response and behavior as an IMRT tool was analyzed using 10 different patients' IMRT plans for each energy

with approximately 7 fields per patient. Analysis of film was done with commercial IMRT analysis software. Analysis of CR plate data was done in IDL (Research Systems, Inc.), with programs written in house, and included several separate algorithms including automatic image registration. This algorithm uses the Fourier-Mellin transform for automatic image registration.

It was found that CR plates showed generally good agreement with the planned values with some significant over-response in the low dose regions, which can be reduced by filtration and improved calibration curves.

In view of the results presented, a CR system stands as a potentially fast and practical tool for IMRT patient-specific treatment QA.

Introduction

Intensity Modulated Radiation Therapy (IMRT)

IMRT refers to a form of conformal radiation therapy in which the intensity of a radiation beam is modulated across the treatment field, i.e. nonuniform fluence is delivered to the patient to optimize the dose distribution.[1] The treatment criteria for plan optimization are specified by the planner and the optimal fluence maps (intensity profiles) for a given set of beam directions are determined through inverse planning, which starts with the definition of treatment goal and constraints. Beams are optimized to deliver a high dose to the target volume and acceptably low dose to the surrounding critical normal structures. In the treatment planning program each beam is divided into a large number of beamlets and their optimum fluence or weight is determined. The optimization of inverse planning involves adjusting beamlet weights to satisfy predefined dose distribution criteria for the composite plan.

Inverse planning differs from conventional forward planning in its basic approach. In conventional forward planning, the planner directly tries different solutions and compares the result (dose distribution) to the desired outcome. When doing inverse planning, the planner tries different problem statements that the optimizer then turns into solutions.[2] The dose optimization process is very much dependent on the set of parameters used as input to the optimization algorithm. Thus the planner's selection of input parameters influences the result indirectly. If the

resulting dose distribution does not satisfy the clinical goal, the planner needs to change the way the problem is described so that the optimizer returns a better solution. The planner chooses beams (gantry positions, field size) and enters objectives; then discrete or continuously varying intensity profiles for each defined beam direction represent the calculated output.

In a multisegmented static field delivery, each field is subdivided into subfields that have uniform beam intensity levels. These subfields are created by the multileaf collimator (MLC) and delivered in a stack arrangement one at a time in sequence without operator intervention. While MLC leaves are moving to shape the next subfield, the accelerator is turned off. The final intensity profile is a composite of dose increments delivered by each subfield (Figure 1). This method of IMRT delivery is also called "step and shoot".

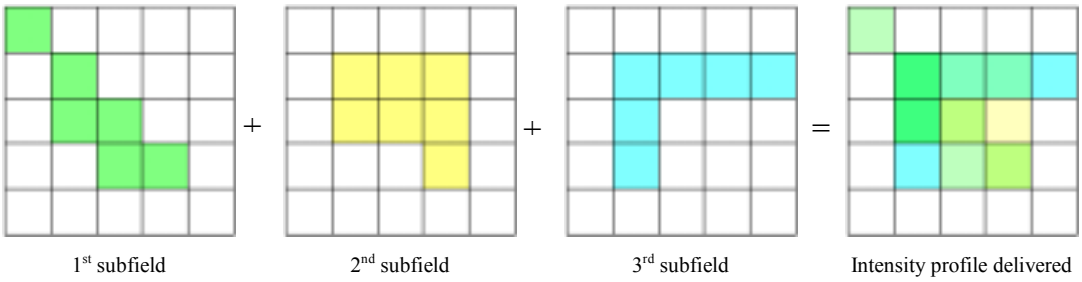

Figure 1. Intensity profile delivered from MLC sequence

For the clinical implementation of IMRT at least three systems are required:

- A treatment planning computer system;
- A system that transfers planning information to the delivery system; and

- A system for delivering the intensity profiles as planned.

Figure 2 presents a flow chart for an IMRT procedure. The process of IMRT treatment includes treatment setup (patient positioning), patient immobilization, image acquisition (CT mostly), treatment planning, treatment verification and actual treatment.

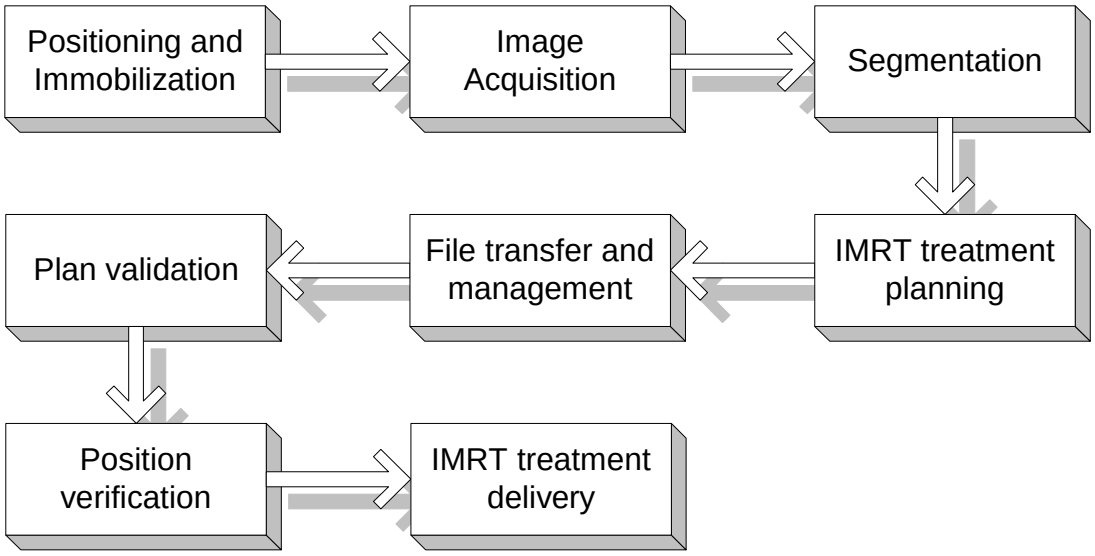

Figure 2. The overall process of IMRT planning and delivery

Quality Assurance (QA) of IMRT

Systematic commissioning and quality assurance are integral to the implementation of IMRT. QA of IMRT delivery systems consists of two separate issues – machine related QA and patient related QA. Machine related QA includes leaf position accuracy, field symmetry and flatness, and dose linearity and dose

accuracy; patient-specific QA includes phantom plan measurement, fluence (intensity) map check, and absolute dose verification. In general, QA of IMRT has three aspects: commissioning and testing of the treatment planning and delivery systems, routine QA of the delivery system, and patient-specific validation of treatment plans. The first aspect is concerned mainly with the integrity of the inverse planning and IMRT delivery system. The second one is concerned with the normal operation of the MLC delivery system. The third one ensures an accurate and safe treatment of a patient.

IMRT QA requires an advanced understanding of mathematical principles of dose optimization, computer-controlled delivery systems and issues that relate to the dosimetry of small and complex-shaped radiation fields. It also requires understanding of treatment setup, planning and delivery uncertainties, and their impact on patients treated with IMRT. Treatment planning optimization for IMRT is based on dose-volume constraints and dose limits for critical structures and target tissues. Therefore, understanding these concepts is also important. Overall, QA for IMRT is much more complex than QA for conventional radiation therapy.

The goal of IMRT plan validation is to verify that the correct dose and dose distribution will be delivered to the patient as calculated by the treatment planning system. To ensure proper IMRT delivery, one needs to check that the plan has been computed properly and that the leaf sequence files and treatment parameters charted and/or stored in the Read/Verify system are correct and will be executable. Items that

need to be validated include: monitor units (or absolute dose to a point), MLC leaf sequences or fluence maps, dose distribution, and collision avoidance. The first three items represent patient-specific IMRT QA.

IMRT brings improved dose sparing of normal tissues and possibility of dose escalation, but also there is a risk to the patient from a dose error. Patient-specific QA captures the integrated results of image acquisition, segmentation, planning, agreement with the prescribed dose, and geometric and dosimetric calibration of the treatment planning and delivery systems. So in this approach, the performance of the combined system is validated and QA is aimed at identifying problems in the overall procedure.[3]

When it comes to patient-specific QA, the ideal test is to do true in vivo dosimetry and place detectors inside the patient, which does not sound like a desirable solution from the patient point of view. Instead, a patient-specific phantom study is done. In this study the IMRT plan is first generated with the patient CT scan and then patient-optimized fluences are applied to a CT scan of a water equivalent phantom. The IMRT system recalculates doses for the phantom geometry. The dosimetry verification compares the calculated and measured doses for the phantom. In implementing this process, it is assumed that if $Dose_{measured}$ / $Dose_{calculated}$ for a phantom agrees within a few percent, then $Dose_{delivered}$ / $Dose_{calculated}$ in a patient should also agree within a few percent.[4] A bonus feature of this study is that it

verifies whether an accelerator and/or MLC controls are behaving properly, at least for the day of the study. Typical techniques used for this verification are

- film dosimetry;
- ionization chamber measurement; and
- diode array measurements.

To verify that the calculated dose distribution is delivered accurately during treatment, film dosimetry is usually used. In this case the IMRT plan verification procedure includes phantom plan calculation (extraction of planar dose distributions), phantom and film irradiation, film developing, scanning and calibration, and finally plan/film comparison.

Our question is, can a desktop computed radiography (CR) system be used for the patient-specific IMRT QA? Computed radiography is a well established process for digital radiographic imaging. In comparison to film, the main CR benefits are non-chemical development of images, image quality that does not depend on processing conditions, and immediate digital storage of images. This project investigates using a CR system for patient-specific IMRT QA.

Materials and Methods

The devices, procedures and processes used during this research are briefly explained in this chapter. Where necessary, basic design and operational details are given.

Linear Accelerator

The linear accelerator (LINAC) uses high-frequency electromagnetic waves to accelerate charged particles such as electrons to high energies through a linear accelerator tube. The high energy electron beam is itself used for the treatment of superficial tumors, or it can be made to strike a target to produce x-rays for the treatment of deep-seated tumors.

There are several types of LINAC designs. Figure 3 shows the block diagram of a typical medical LINAC with some major components.

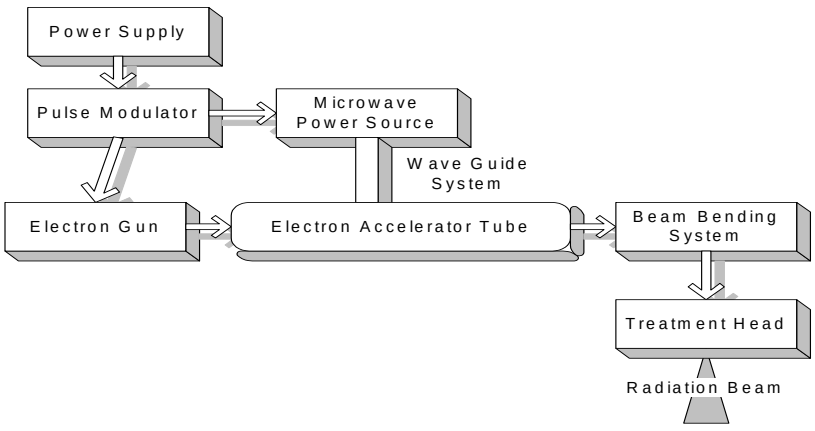

Figure 3. Block diagram of typical medical LINAC

A power supply provides direct current (DC) power to the modulator. High-voltage pulses from the modulator section are flat-topped DC pulses of a few microseconds in duration. These pulses are simultaneously delivered to the microwave power source (magnetron or klystron) and the electron gun. Pulsed microwaves produced in the microwave power source are injected into the accelerator tube via a waveguide system. At the proper instant electrons produced by the electron gun are also pulse injected into the accelerator structure. The accelerator tube consists of a copper tube with its interior divided by copper diaphragms of varying aperture and spacing. This whole section is evacuated to a high vacuum. As the electrons are injected into the accelerator tube with an initial energy of about 50 keV, the electrons interact with the electromagnetic field of the microwaves. The electrons are bunched together and accelerated along the accelerator tube.

As the high energy electrons emerge from the exit window of the accelerator structure, they form a pencil beam of about 3 mm in diameter. The electrons are then bent under the action of a transverse magnetic field through the angle between the accelerator tube and the target – this bend is simply a way of reducing the overall length of the machine.[1]

In electron mode the electron beam is allowed to pass through a vacuum window at the end of the accelerator and thence on towards the patient. When operating in photon mode, the electrons impinge upon a high atomic number target where bremsstrahlung photons are produced. Finally the electron or photon beam

passes through a segmented radiation detector and a variety of beam modifiers in the accelerator head before reaching the patient. Figure 4 illustrates medical LINACs operating in photon mode and electron mode.[1]

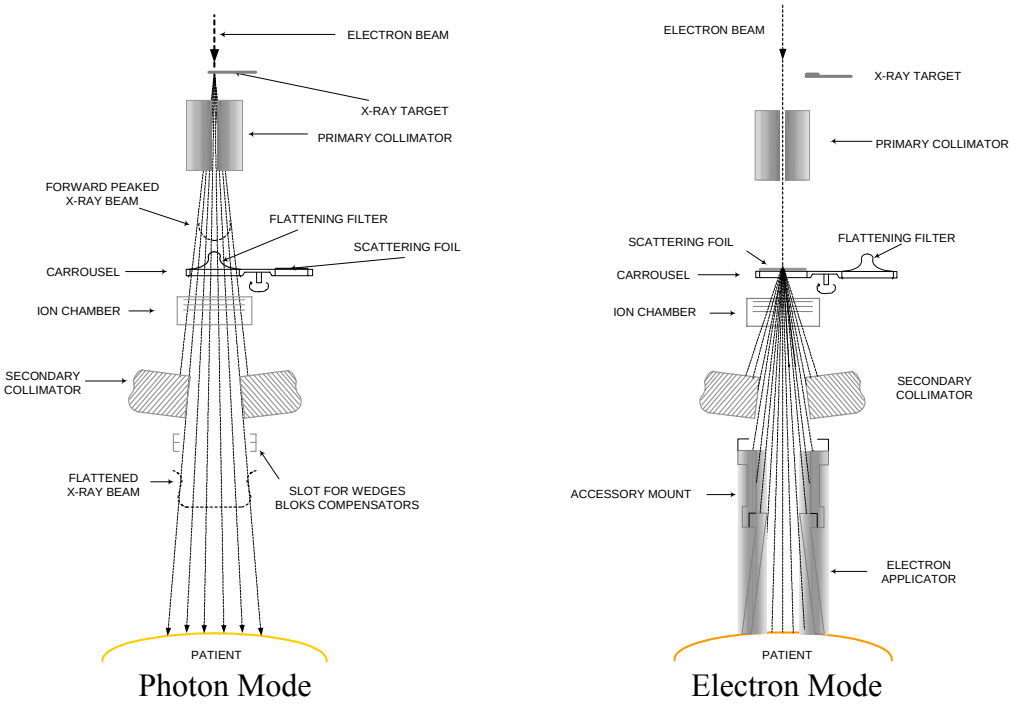

Figure 4. Accelerator head

A thick shell of high density shielding material such as lead or tungsten surrounds the accelerator head. The accelerator head contains the x-ray target, scattering foil, flattening filter, ion chamber, fixed and movable collimator (jaws), and light localizer system.[1]

Two Varian Clinac 21EX linear accelerators have been used in this study. The 21EX (4-10) produces 4 MV and 10 MV photons while the 21EX (6-18)

produces 6 MV and 18 MV photons; both produce five energies (6 MeV, 9 MeV, 12 MeV, 16 MeV, and 20 MeV) when used in electron mode. The 21EX model is equipped with MLCs and capable of delivering IMRT treatments. Photographs of the components of the treatment head and gantry of a Varian LINAC 21EX (6-18) are shown in Appendix A.

Multileaf Collimator (MLC)

An MLC for photon beams consists of a large number of collimating blocks or leaves that can be driven automatically, independent of each other to generate a field of almost any shape. A typical MLC system consists of 80 leaves or more arranged in opposed pairs. The 21EX MLCs have 120 leaves. An individual leaf has a projected width of 1 cm or less at the isocenter. The leaves are made of tungsten alloy and have thickness in the beam direction ranging from 6 cm to 7.5 cm, depending on accelerator type. The leaf thickness is sufficient to attenuate primary x-ray transmission through the leaves to less than 2% (compared with about 1% for collimator jaws and 3.5% for Cerrobend blocks). The interleaf transmission is usually less than 3%.[1]

Although there are similarities in MLC design among different manufacturers, significant differences can be identified as well. For example in the Varian LINACs, used for this study, the MLC is positioned as a tertiary system below the standard adjustable jaws; in comparison Elekta replaces the upper jaw of

the standard collimator with the MLC. Each approach has advantages and disadvantages.

MLCs can be used as a field shaper and blocking device (instead of custom blocks made of lead or Cerrobend). The use of MLCs in blocking and field shaping is ideally suited for treatments requiring large numbers of fields because automation of the blocking procedure results in a significant reduction of set-up time. MLCs can practically eliminate the use of Cerrobend blocking except for shaping small fields or "island" blocking in which an area within the open portion of the fields needs to be blocked.

The importance of MLCs is not just the replacement of Cerrobend blocking. MLCs are an essential part of beam intensity modulation for IMRT deliveries. In multisegmented static field delivery, each field is divided into subfields that are irradiated with uniform beam intensity. The subfields are created by the MLC and delivered in a segmented stack arrangement. The accelerator is turned off while the leaves move to create the next subfield. The sum of dose increments delivered by each subfield creates the intensity modulated beam as it was planned by the treatment planning system (see Figure 1). This method of IMRT delivery is called "step-and-shoot".[1]

Treatment Planning System (TPS)

At Mary Bird Perkins Cancer Center, patient and phantom IMRT plans are calculated using an ADAC Pinnacle^3 treatment planning system.

IMRT Planning and Planar Dose Extraction

The IMRT planning process consists of two components:

- Optimisation
    - During the optimisation process, desired fluences are calculated for each field to get an optimised dose distribution from the user-specified dose and DVH (dose-volume histogram) constraints for target and organs at risk.
- Conversion
    - In the conversion process, desired field fluence profiles (from the optimisation step) are translated to MLC motion patterns. Expected fluence profiles for every field are created, that take into account physical and mechanical aspects of the MLC and LINAC. These realistic profiles are used for the calculation of the final dose distribution.

After the IMRT treatment plan is approved by the physician, planar dose files for the IMRT QA are created. The planar dose option in the Pinnacle system allows generation of the dose distribution for any beam at a given depth in either a flat water phantom or the current image set. Computation of dose to a plane and extraction of the planar dose files are done by the ADAC software.[5]

These TPS planar images represent the dose delivered by each beam (field) used in the IMRT plan. These images, referred to in this paper as plan images, are compared to the measured planar dose distributions delivered to the phantom.

Computed Radiography System

Computed radiography is a radiographic technique that replaces x-ray film with photostimulable phosphor plates; it is a generic term applied to an imaging system comprised of:

- photostimulable storage phosphor - for acquisition of the x-ray projection image;
- CR reader - for extraction of the electronic latent image; and
- digitizer system - for conversion of the signals to digital form and image storage.

Computed radiography (CR) is a practical, efficient and economical method of capturing and converting radiographic images into digital form. The medium for capturing the x-ray is a phosphor imaging plate that is placed in a standard size cassette, replacing the regular radiographic film. The x-ray exposure forms a latent image on the plate that is then scanned (read or developed) using a laser CR reader. The CR unit displays and/or stores the resultant digital image. After scanning, the plate is erased and ready for another x-ray image exposure, allowing the CR system to be very economical (compared to the film process it replaces). The imaging

plate's advantages include ease of use, high spatial resolution, high detection sensitivity with high signal-to-noise ratio, large detection area, extremely wide dynamic range, and capability for reuse.[6]

The CR plate is made up of protective, phosphor, and support layers (structure is shown in more detail in Figure 7). The imaging plate is coated with a photostimulable storage phosphor ($BaFBr:Eu^{2+}$), that is sensitive to several kinds of radiation and is widely used in various fields.[6] The phosphor layer consists of very small crystals (grain size: about 5 μm) of photostimulable phosphor of barium fluorobromide containing a trace amount of bivalent europium as a luminescence centre; these centers are sensitive to photons in the x-ray energy range.

Photostimulated Luminescence (PSL)

Naturally or artificially irradiated minerals may emit light with decreasing intensity upon illumination, especially with excitation wavelengths longer than the wavelength of the emitted light. This effect is clearly different from fluorescence excited by shorter wavelengths or phosphorescence ceasing slowly after illumination.[7]

In 1921 Przibram observed that irradiation-coloured kunzite (rose fluorspar) crystals were bleached not only by heating, but also by light, and that in some cases phosphorescence was detectable. The observed effect of light emission of illuminated irradiated substances was described as radio-photoluminescence. During his first experiment, Przibram irradiated kunzite using a radium source and

illuminated the sample with an arc lamp. He stated that the radium irradiation produced luminescence centers which are then excited by light exposure.[7]

The theory of photostimulated light emission is derived from the same trap model as thermoluminescence. PSL is a phenomenon that occurs due to the release of trapped charge carriers into the conduction band. The photostimulable phosphors are characterized as exhibiting long-wavelength luminescence, as compared with incident light after the photoionization excitation. Eu-doped alkali halides are such phosphors, in particular, barium fluorobromide doped with Eu^{2+}; it has been studied extensively as a phosphor capable of storing x-ray information.[6]

The PSL mechanism of BaFBr:Eu^{2+} is illustrated in Figure 5.

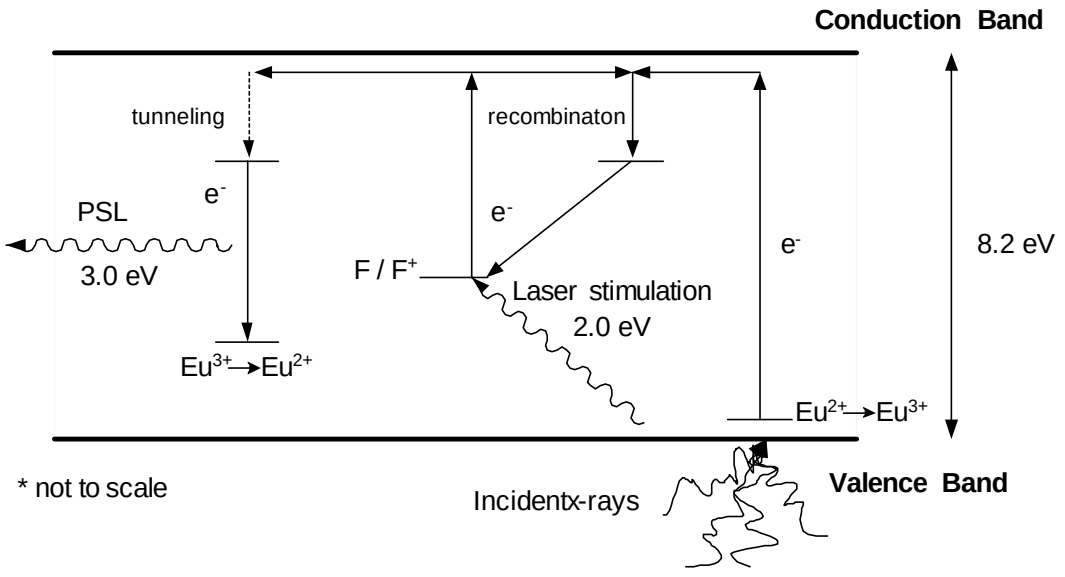

Figure 5. PSL mechanism in BaFBr:Eu^{2+}
(for purposes of illustration e^- propagation goes from right to left)

The x-ray or UV light irradiation ionizes Eu^{2+} ions (an x-ray photon is absorbed by the phosphor and the energy is transferred to a number of Eu^{2+} sites) and converts them into Eu^{3+} ions (Eu^{2+} is oxidised to Eu^{3+} and a photoelectron is ejected), either directly or by trapping holes. Photoelectrons are ejected into the conduction band and trapped by F^+ centers (halogen ion vacancies) to form two types of F centers, $F(Br^-)$ and $F(F^-)$. In this process electrons are trapped and their energy stored as the latent image.

The absorption peak due to the photoionization transition of Eu^{2+} ions is observed at 6.6 eV, and PSL centers are efficiently formed by this photoionization absorption. In the case of excitation via ionising radiation, electrons in the conduction band are captured by F^+ centers, whereas holes in the valence band are generally considered to be trapped by Eu^{3+} ions. Visible light irradiation liberates trapped electrons into the conduction band and returns them to convert Eu^{3+} ions to excited Eu^{2+} ions. Thus, Eu^{2+} luminescence is observed as photostimulated luminescence.[6]

A latent image readout mechanism is shown in Figure 6.[8] The laser in the integrated plate reader and eraser scans the exposed phosphor plate as it moves at constant speed through the reader. As the plate moves, the mirror scans the focused laser beam across the plate in a raster pattern, retracing between each scan line. As the laser moves across the plate, the integrating collection cylinder collects the stimulated luminescence. At the top of the collection cylinder are two

photomultiplier tubes (PMTs). PMTs convert light into voltage signals, which are amplified and digitised. The sampling process produces 1024 pixels for each scan line. The 12-bit digital image is then transferred to the computer for image processing.[9]

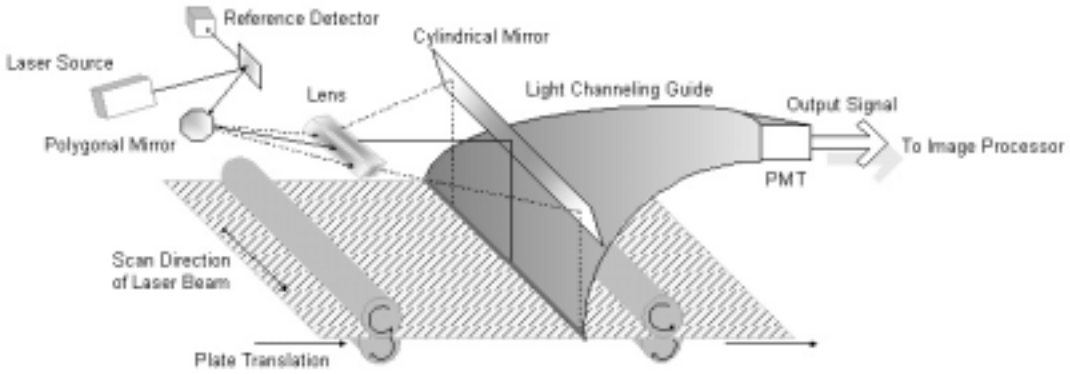

Figure 6. Latent image readout

The readout cycle of an imaging plate is illustrated in Figure 7. The imaging plate captures x-ray radiation or electrons in its phosphor crystal structure, creating a latent image. To readout an image, the imaging plate is placed in the CR scanner/reader. As the laser beam in the CR reader scans across the imaging plate, the phosphors are excited and release the energy they have stored. This energy is emitted from the plate as a violet-blue glow. The strength of this glow is directly proportional to the amount of radiation absorbed. The phosphor glow is captured by the scanner and converted into a digital image.

The laser scan does not extract all the energy stored in the crystals so the storage phosphor plate must be erased. After the plate is scanned it enters the eraser

where it is flooded with bright fluorescent light. This intense light removes any residual energy remaining on the plate so that it can be used again.

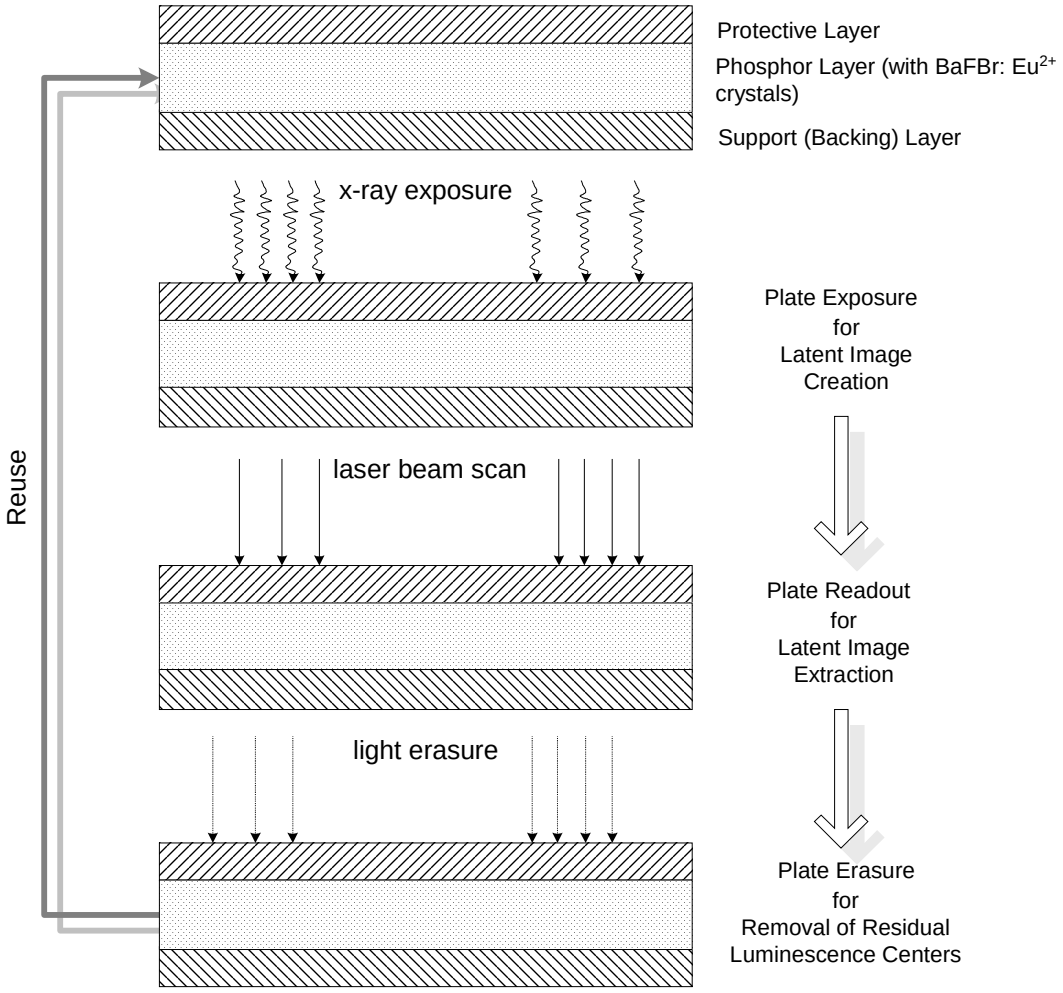

Figure 7. Readout cycle

Several CR vendors exist in the market: Fuji, Agfa, Kodak, and Konica, among others. Their systems have some substantial differences, such as image

processing methods. These differences were not investigated as part of this project. The CR system used in this study is a Kodak ACR-2000i system.

Kodak ACR-2000i System

The Kodak ACR-2000i system consists of a phosphor plate reader with the integrated eraser, shown in Figure 8. A darkened room is recommended for handling of CR plates. A computer workstation and Kodak General Radiography software are included as part of the system. The ACR-2000i system scans plates up to 14 x 17 in. in 50 seconds; erasure takes 30 seconds per plate. Images can be saved and exported in DICOM 3.0 format.[10]

Figure 8. Kodak ACR-2000i reader and eraser

The CR plates used in the study were KODAK ACR Phosphor Screens (35 x 43 cm) for KODAK ACR-2000 Systems, that come with the KODAK ACR Cassettes (35 x 43 cm) for KODAK ACR Systems, as seen in Figure 9.

While visiting the KODAK booth at the AAPM 46th annual meeting, July 25-29, 2004, a Kodak representative provided information on the CR plates used for this study (that was not available previously despite numerous inquiries), and according to this information the plates used for the research were not Kodak plates, but rather Agfa ADC MD10 plates. Agfa no longer provides specifications for the ADC MD10 plates; specifications for new Agfa ADC MD40 plates are available on the manufacture's web site.

Figure 9. CR detector (screen + cassette)

Phantom Used in the Study

Basic dose data are usually measured in a water phantom (water tank) that closely approximates the radiation absorption and scattering properties of muscle and other soft tissues. Since it is not always possible to put radiation detectors (such as CR plate or film) in water, solid dry phantoms have been developed as water substitutes.

For a given material to be water equivalent it must have the same effective atomic number, number of electrons per gram, and mass density. Since Compton effect is the dominant mode of interaction for MV photon beams in the clinical range, the necessary condition for water equivalence is the same electron density number as that of water.

The electron density of a material, ρ_e, may be calculated from its mass density, ρ_m, and its atomic composition as

Eq. 1. $$\rho_e = \rho_m N_A \sum_i a_i \left(\frac{Z_i}{A_i} \right)$$

where N_A is Avogadro's number and a_i is the fraction by weight of the ith element of atomic weight A_i and atomic number Z_i.[1]

A common solid dry phantom is a plastic water phantom. This phantom is an epoxy resin-based mixture. It has a density of 1.02 g/cm^3 and provides dosimetry characteristics similar to natural water over the entire oncology energy range. Dose

measurements in a plastic water phantom agree with those in true water within 0.5% ± 0.04% above 7 MeV and need no correction factors.[11]

Through the course of this study, a plastic water phantom was used. Two slabs of plastic water were used, each with dimensions of 30 x 30 x 5 cm^3 (width x length x thickness).

Measurement Procedure

Setup for the Measurements

The setup used for plate exposures was the same as the setup used commonly for film dosimetry. A series of measurements with several different thicknesses of lead sheets were used (lead sheets are used as low-energy photon filters, in film dosimetry they can be used on both sides of the film to compensate for overresponse of the film to low-energy photons). Because no significant difference was observed in cases with or without lead sheets and because handling of lead sheets required special care to be taken not to contaminate the phantom with the lead, we decided not to use lead sheets in the study. In retrospect, using the lead sheets can somewhat improve agreement between plan and plate profiles in low dose regions.

Measurement with the plate inside the cassette was made (cassette thickness must be taken into account for accurate depth placement of the plate itself). After analysis, no significant difference between measurements made with and without the cassette was observed so it was decided to use the plates without the cassette for future measurements and to put the plates inside paper envelopes (with black

backing) to protect the plates from direct exposure to light and from possible damage during regular handling throughout the measurement process.

To setup a CR plate for exposure, the CR plate was first transferred from the cassette to a paper envelope. The film was placed between the two slabs of plastic water; the white surface of the CR plate faces the x-ray source. The phantom is positioned on the treatment couch. The source to plane distance (SPD) was 100 cm (location of the plate); the source to surface distance (SSD) was 95 cm. Finally, a 5 x 5 cm^2 field was used for all calibration measurements. The field sizes for the patient plan exposures varied according to the plan. All measurements were made at a depth of 5 cm. Figure 10 shows this setup.

Figure 10. CR plate exposure setup

Exposure

Exposures were made for 3 different energies: 4 MV, 6 MV and 10 MV. Calibration curve measurements were done first for each energy and then for all

three energies; IMRT fields from 10 different patients (approximately 7 fields per patient) were acquired. Some fields were repeated to check reproducibility.

Each patient plan was opened in the MultiAccess application. QA mode was chosen as the mode of delivery and the first IMRT field is selected in the resultant window. Once the chosen field was downloaded MLCs started to move to shape the appropriate area. After the exposure (delivery of the chosen field), proof of the delivery is recorded as QA performed. The next field is chosen afterwards.

After the delivery of each field, the CR plate was taken out of the treatment room, still in the envelope, and scanned in the Kodak scanner. For study purposes, some of the plates (where noted) were scanned immediately after exposure and some after various time intervals.

Scanning

After the exposure the plate is taken out from the envelope and placed in the scanner. On the Kodak computer a new study is created and with the click of a button the plate is scanned. During the scanning process, the image slowly appears on the computer screen as it is being read by the scanner system.

The scanning was done in port film mode. Port film mode uses a photomultiplier tube gain reduced by 100 in comparison to when used in diagnostic mode. Low resolution mode (1024 pixels) setting was used. With this setting, average image size was 2.5 MB. The Kodak software saves plate images in DICOM

3.0 format. After the plate is read, it falls into a drawer where it gets erased with a bright halogen light. After a few seconds the plate is ready for reuse.

DICOM

DICOM (Digital Imaging and Communications in Medicine) is a standard that is a framework for medical-imaging data transfer. Based upon the Open System Interconnect (OSI) reference model, which defines a 7-layer protocol, DICOM is an application-level standard, which means it exists inside layer 7 (the uppermost layer). The standard was developed by the American College of Radiology (ACR) and the National Electrical Manufacturers Association (NEMA) with input from various vendors, academia, and industry groups. It is referred to as "version 3.0" because it replaces versions 1.0 and 2.0 of the standard previously issued by ACR and NEMA, which was called the "ACR-NEMA" standard. DICOM provides standardized formats for images, a common information model, application service definitions, and protocols for communication.[12] Kodak uses the DICOM 3.0 standard for storage of the image data.

To use DICOM images in available programs all file name extensions had to be changed to accommodate different file name conventions. An MS Visual Basic script was developed for this purpose.

Reading in, Conversion and Calibration of Plate and Plan Image Files

Conversion of Plate Image Files

During the course of the study, the decision was made to read in and compare, in the algorithm developed for the IMRT analysis, both plan and plate images in TIFF format. For that purpose, a program for the conversion of Kodak DICOM files to TIFF files was developed in MS Visual Basic (VB). The program uses Kodak Image Controls, DICOM ocx[13,14] (DICOM ActiveX control), and Microsoft Common Dialog Control as part of the VB project components.

The program (see Appendix B) is capable of opening original Kodak DICOM 3.0 files. The program converts the image to TIFF format and can also perform several transformations. Transformations include grayscale inversion and flipping it horizontally and/or vertically. The program can also be used simply to change the extension of the original DICOM file.

Every acquired plate image had to be opened in this application and converted to TIFF format. Because such a large number of exposures was made (around 700), this process was not very efficient. Taking this into consideration, we switched to using a free DICOM reader program called IrfanView[15] for the plate DICOM image to TIFF format conversion. Because this software requires DICOM files to have .dcm extension, the Visual Basic script was used for file renaming.

This renaming script changes the KODAK DICOM file name to a user specified name with the .dcm extension, Figure 11.

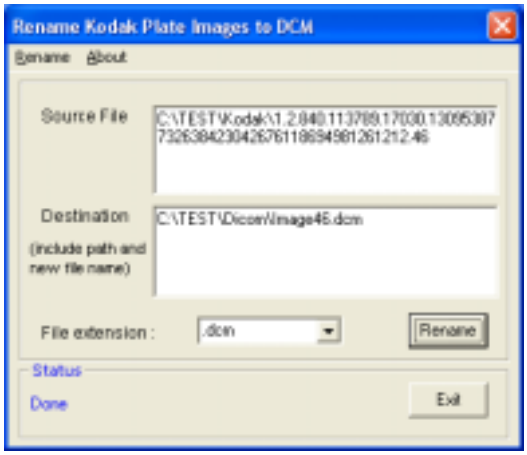

Figure 11. VB script used for renaming

Once correct paths were established, for both source and destination files, several images could be renamed very fast. This program was used for renaming all the plate image files to .dcm and then the IrfanView software was used for the conversion of every image file from the DICOM format to TIFF format. The converted files were then analyzed with in-house software, described in the next section. In the future one could consider incorporating the conversion and analysis software into the same application (opening file from the original format and performing the analysis).

Conversion and Calibration of Plan Image Files

Plan Calibration Curve

The TPS field (plan) image contains information on dose rate values; to get dose (in cGy), one multiplies those values by the number of monitor units actually delivered by the LINAC when delivering the plan to the phantom. For convenience, the commercial RIT113 software[16] was used (instead of developing an equivalent program in-house).

For every plate exposure, for each field delivered, a plan calibration curve is required by our IMRT analysis algorithm. The calibration maps dose (in cGy) to pixel values or shades of gray. To generate the calibration curve, the minimum, middle and maximum dose rates were obtained from the RIT113 software and multiplied by the number of monitor units. These dose values were linearly scaled across 255 pixel (gray) levels, with the minimum value mapped to a pixel value of 0 and the maximum mapped to 255. MS Excel was used to calculate the slope and intercept of the calibration curve from these values. Figure 12 shows a sample plan image and a color bar indicating the dose rate values. Table 1 and Figure 13 give the conversion values and linear calibration for this sample plan, which required 184 monitor units to be delivered.

The plan image calibration procedure is repeated for all the fields delivered for each patient. Approximately 300 different fields were delivered in this study.

The coefficients for the linear calibration are used subsequently in the algorithm for the conversion of the plan image to dose values.

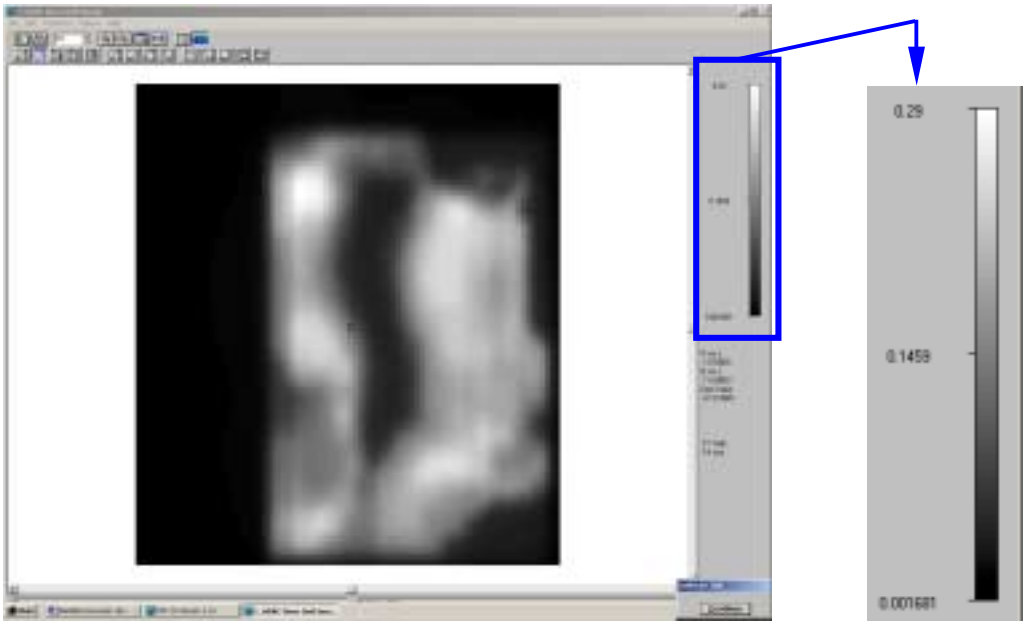

Figure 12. Imported plan image file

Table 1. Plan image dose values

RGB value	Dose Rate (cGy/MU)	Dose (cGy)
0	0.001681	0.309304
127.5	0.1459	26.8456
255	0.29	53.36

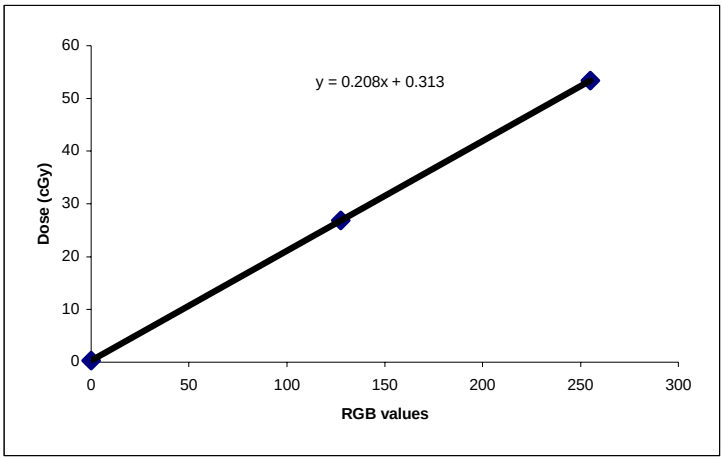

Figure 13. Plan image calibration curve

In retrospect, since the relationship is linear and the plan data values are exact, MS Excel was not needed. All that was needed was to record the minimum and maximum dose values from which we could calculate the slope and intercept directly as

Eq. 2. $$slope = \frac{\max dose - \min dose}{255 - 0}\ ;\ intercept = \min dose$$

A more streamlined approach would be to calibrate the plan images directly in the IMRT analysis program, skipping the use of RIT113 and Excel. For this project, the time needed for coding the analysis program to read Pinnacle Planar Dose files and to generate the calibration, was deemed excessive.

Conversion of Plan Image Files to TIFF Format

After obtaining the data for the plan calibration, the RIT113 software was used to export the plan images as TIFF files. Together, the TIFF files and the plan calibrations are used to import the TPS plan into our IMRT analysis software.

CR Plate Calibration and Conversion

CR Plate Calibration Curve

CR plate calibration curves for each of the three energies used were acquired by exposing several plates to a series of doses using 5 x 5 cm^2 field sizes, 100 cm SPD and 95 cm SSD.

First we exposed a set of plates by doing both one exposure per plate and several exposures per plate for all of the three energies used; Figure 14 shows sample images from these exposures. It was observed that the CR plate values do not change regardless of the number of exposures done per plate. To speed up the process of gathering calibration data, several exposures per plate were used for the final calibration curves.

For each field delivered to the plates, the number of monitor units delivered was recorded. An MS Excel spread sheet calculates the delivered dose using Eq. 3; Appendix C describes this calculation and the purpose of the various factors in the equation.

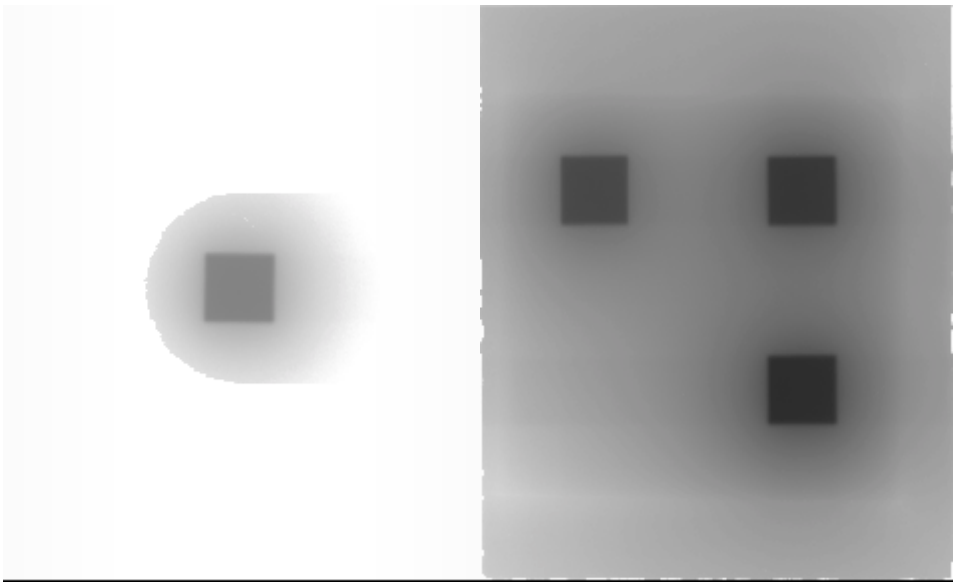

Figure 14. Example CR plate calibration images showing a single field per plate (left) and multiple fields per plate (right)

Eq. 3. $$D = MU \cdot S_{c,p}(5x5) \cdot TMR(5,5) \cdot \left(\frac{100cm + d_m}{100cm} \right)^2$$

Knowing the depth of the point of interest (5 cm), the depth of maximum dose d_m (cm), field size used (5 x 5 cm^2) and the corresponding $S_{c,p}$ and TMR, and the number of monitor units delivered, MU to dose (in cGy) conversion factors were calculated for each energy and then used to calculate the dose delivered for each field. The calculated conversion factor for each energy is listed in Table 2.

After measuring the intensity or gray level for each calibration field, the CR plate calibration curve was determined using curve-fitting to the data. MS Excel was used to do the curve-fitting. The calibration curve is used in the IMRT analysis program to convert the CR plate images to dose (in cGy).

Table 2. MU to dose conversion factors for Eq. 3

Energy	Conversion Factor (for setup used)
4 MV	0.83804679376
6 MV	0.86799008671
10 MV	0.93321764692

CR Plate Image and Plan Image Resampling (Resizing)

To be able to adequately compare plan and plate images (and to check that the field size of each delivered field is correct), both images were resampled to have the same pixel size. Knowing that the plate area is 35 x 43 cm^2, once opened in any photo editor software, the image is resized to 35 x 43 cm^2, and pixel size is set to 4 pixels/cm, which matches the 0.25 cm pixel size for the TPS plan images. An alternative way to do it would be to write out plan data at much higher resolution, i.e. to match the resolution of the plate image.

Because of the image registration algorithm used (larger images give better registration) the image was enlarged by 700%, using bicubic interpolation; Appendix D gives an explanation of interpolation methods. The images were cropped to an area of 700 x 700 pixels (as they had to have same dimensions in pixels for the registration algorithm), and saved in TIFF format as the final images that will be used in the analysis. Figure 15 shows the cropping boundary on a sample plate image.

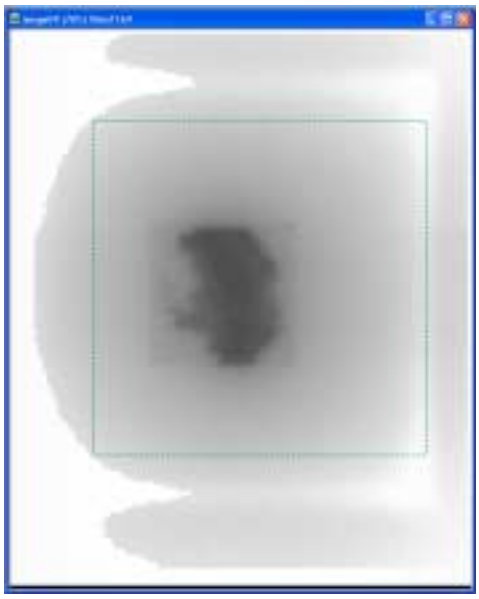

Figure 15. Plate image cropping

The plan images must be resized too. The plan images were resized by the same percentage value (700%) and cropped to 700 x 700 pixels. Now both images are comparable in size and ready for the analysis, except that the two images are probably not aligned. The plate and plan images may not have the exposed area located at the same position. They may be rotated and/or shifted relative to each other. The automatic image registration algorithm (described in the next section) aligns the plate image to the reference plan image.

Image Registration

To accurately compare plan and plate images, by comparing absolute dose values at different points in the field as well as horizontal and vertical dose profiles ,

the plan and plate images must be properly registered (aligned). At first, we planned to use the RIT113 Film Dosimetry System for the IMRT analysis. Although the current version (3.14) could not read Kodak plate images, we still thought it would be useful for the analysis. However additional limitations of RIT113's image alignment method led us to implement instead a separate algorithm for automatic image alignment. Before describing the automatic alignment method, we describe the process and limitations of image alignment in the RIT113 software. We also developed a separate program to compare the IMRT data from plans and plates, because the RIT software couldn't read the Kodak plate image files.

Note: RIT113 just put a new version of its software on the market (version 4.1) and this version claims to handle plate images the same way it handles film images. In that case, one still faces the problem of image cropping (user dependent and subjective) and placing the control points (again extremely user dependent and subjective).

To perform registration in the RIT software, the image is cropped first to an appropriate field size, depending on the field size of the IMRT field used for the exposure (Figure 16). The crop window is placed manually, and it depends strongly on the visual ability and skillfulness of the user. If rotation is necessary, it is again done manually and depends strongly on the skill of the user. Cropping and rotation are possible sources of image registration error.

Figure 16. Image cropping

For its image registration method the RIT software uses control-points. With control points, the target image is registered into the image space of a reference image. A set of control points are defined in both images (Figure 17). Comparison of the control point locations identifies necessary rotation, scaling and shift. An affine transform then corrects the target image to align to the reference image.[16]

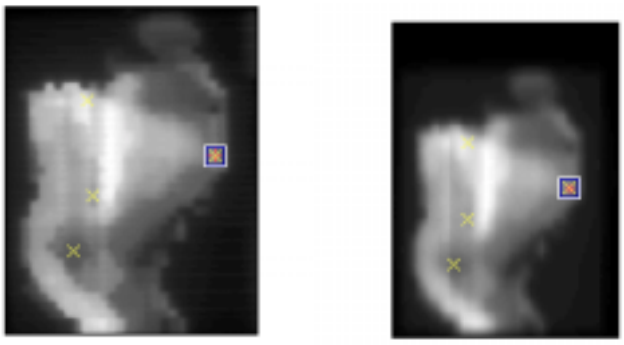

Figure 17. Control points placement in RIT113 v3.14

Ideally, the manually placed control points mark identical places in the target and reference images. This technique of manually placing control points is very

subjective. If control points are not placed carefully and accurately, very different results may be obtained as demonstrated in Figure 18.

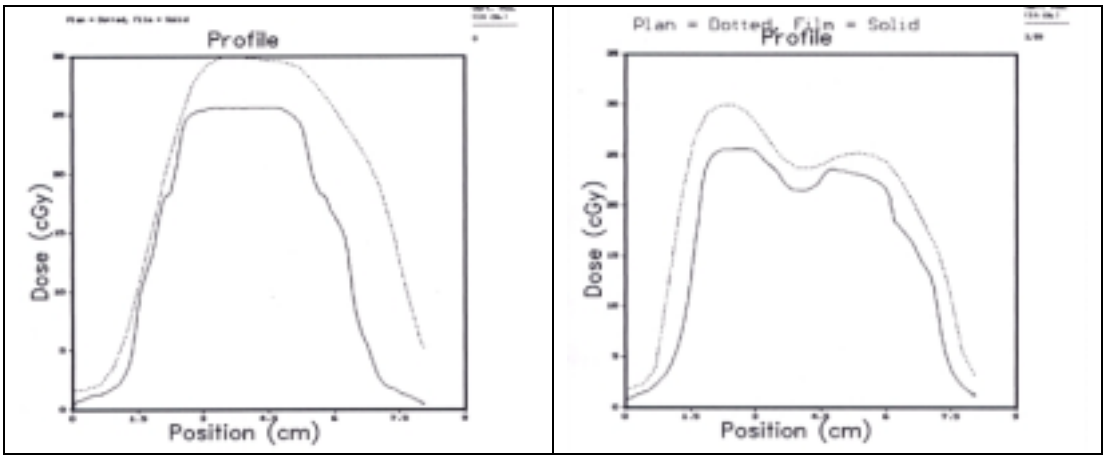

1st user

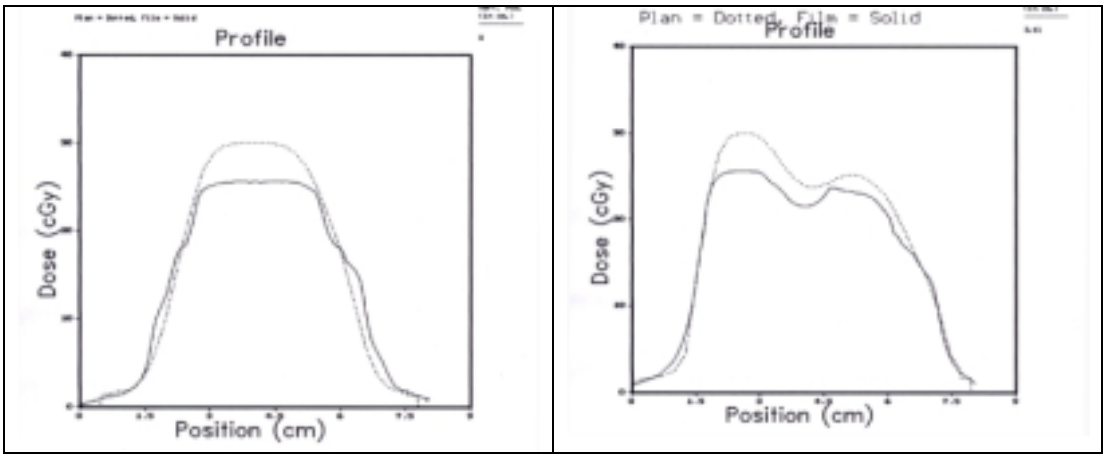

2nd user

Figure 18. Profiles depending on the control points placement and cropping

The quality of analysis strongly depends on the operator and may not be accurate or reproducible. The profiles shown in Figure 18 were generated from registered images where the control points were set by two different users; although

both users were doing IMRT QA regularly using the RIT113 system, the discrepancies between the resultant profiles (solid lines) are quite striking.

We have implemented two different approaches to eliminate the problems of manual placement of control points. One method provides automatic placement of control points, which will not depend on the user doing the analysis. The other method is to use a fully automatic registration algorithm, where registration is based on inherent image information rather than control points.

Automatic Control Points Placement

An image representing planar dose (plan image) for each beam consists of two parts: the image file itself (.img) and the header file (.header or .hea). From the header file, exact field size and coordinates can be obtained. Once a Kodak screen image is imported into the RIT113 v3.14 system it is transferred to the RIT file format that consists of three parts: two image files (.i00 and .d00) and the header file (.hdr). For the correct transformation and to be able to do IMRT analysis, the plate image once imported had to be converted to a 16-bit integer image.

Once all necessary files were created for the automatic control placement procedure, the “Control Points Placement” program developed in Microsoft Visual Basic was used for the automatic creation of the RIT system .gcp file (Figure 19).

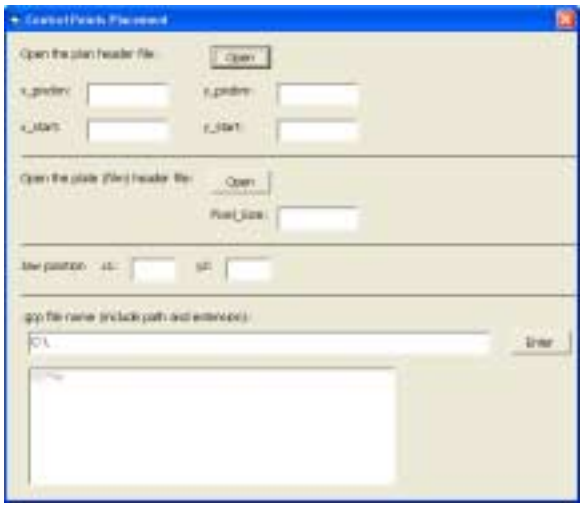

Figure 19. Graphical user interface
(for the automatic creation of the RIT system .gcp file)

Mathematics running in the background of the program uses x1 and y2 jaw positions that can be obtained from the plan printout sheet and pixel dimensions from both header files, as well as x and y start positions from the plan header file, for the calculation of the control points location.

Knowing that x1 and y2 jaw positions represent the origin, the calculation was done as follows:

$$x_{plan} = \frac{|x_{start}| + x_i}{PixelSize} \qquad y_{plan} = \frac{|y_{start}| + y_i}{PixelSize}$$

$$x_{plate} = \frac{x_1 + x_i}{PixelSize} \qquad y_{plate} = \frac{y_2 + y_i}{PixelSize}$$

where x_{plan}, y_{plan}, x_{plate} and y_{plate} values give control points' positions.

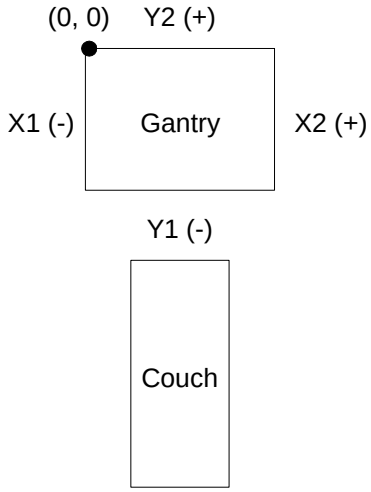

Figure 20. Jaws

What is actually calculated is how many pixels in both x and y direction from the origin control points are located. The origin on a plan image is represented by x_{start} and y_{start} values that are read from the plan image header file as given by the TPS. The same origin on the plate image is given by the position of the x1 and y2 jaws. Since both images also have different pixel sizes, that are again obtained from their header files, values calculated for x_{plan}, y_{plan}, x_{plate} and y_{plate} will be different. Points x_i and y_i are, at present time, picked by the program from a built-in array, that records the smallest possible field size values. The program can be easily changed to allow the user to select the four (or as many as necessary) arbitrary points. Since it is much faster to have points predefined in the program (instead of the user entering them manually) the decision was made to have predefined points in

the program. Once control point locations are calculated they are written into the RIT113 .gcp file format, so that the RIT system can load and use them.

The first step in using this program is to open the plan header file; in the next step, the plate (or film) header file is opened. Values needed for the program execution are automatically populated into the appropriate text boxes; x1 and y2 jaw positions need to be manually entered. Once desired location and name of the .gcp file is entered in the designated text box, by clicking on the 'Enter' button, the .gcp file is automatically created and control point locations are displayed in the text box inside the program itself. The program places four arbitrary points on both (plan and plate or film) image files, as explained previously.

Once finished, the .gcp file now can be used in the RIT113 software for automatic control points placement instead of placing control points manually. By utilizing this program subjectivity of the points placement is gone, i.e. it is not user dependent any more and cases like the one shown in Figure 18 can now be completely eliminated.

The logic works because the images have different pixel sizes, so we are physically going the same distance from the origin on both images – assuming they have the same origin. So unfortunately this procedure has one major flaw: the images must still be cropped manually. If the images are not cropped correctly to begin with, the control points calculated with the program are mispositioned and may produce a worse result than that obtained by manual placement. So the user factor still is not

completely eliminated. With this in mind the need for a fully automatic registration of the images is obvious.

Automatic Registration (Alignment) of the Images

Image registration is crucial for the analysis of different kinds of data and, as shown before, necessary in the IMRT analysis to be able to do accurate profile and absolute dose comparison. Image alignment is basically a linear mapping which consists of translation, scaling, and rotation. It assumes the existence of a reference image. Figure 21 illustrates different types of possible image transformations.

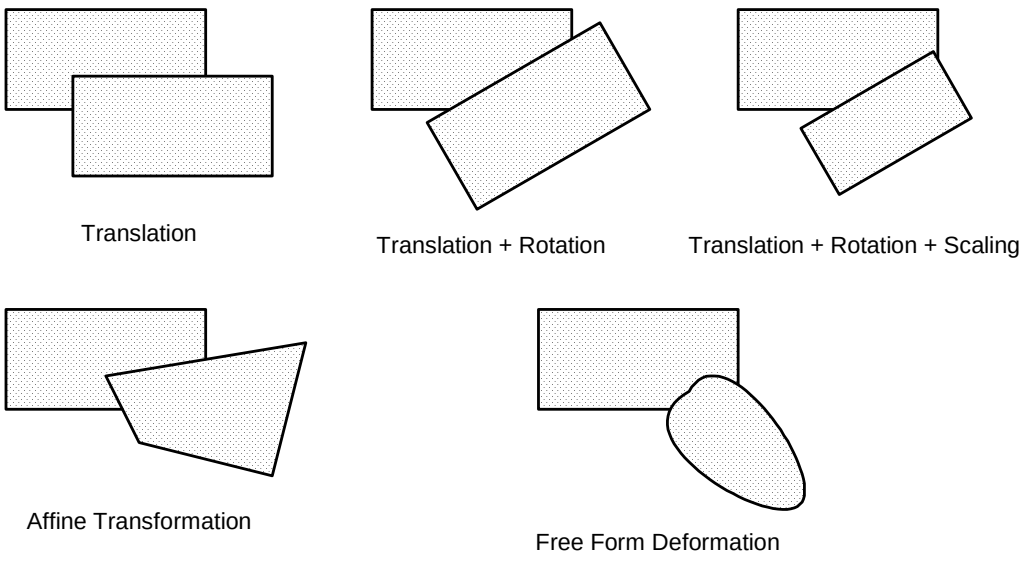

Figure 21. Types of transformation

All registration algorithms attempt to align a destination (transformed) image over a reference image so that pixels present in both images are in the same location.

This process is useful in the alignment of an acquired image over a template, a time series of images of the same scene, or the separate bands of a composite image (co-registration). One practical application of this process is the alignment of multi-modality images in radiology.

There are several different methods used for image registration:[17]

- Correlation
- Transform Methods (including Fourier and Radon transforms)
- Point Mapping (affine transformation)
- Edge-based methods

Correlation based techniques use a 2D normalized correlation function that measures the similarity for each translation in an image patch, but the data must be normalized to avoid contributions from local image intensities.

Fourier transform based techniques use the correlation theorem: the Fourier transform of the correlation of two images is the product of the Fourier transform of one image and the complex conjugate of the Fourier transform of the other. These techniques use several different approaches: phase-correlation, cross power spectrum, etc.Point mapping techniques use control points, point mapping with feedback, or a global polynomial approach for the image registration. Control points can be intrinsic (markers used within image) or extrinsic (control points automatically or manually selected). After the selection of the control points different methods can be used for the registration of the sets of control points (this

method is used by the RIT113 software). Point mapping with feedback determines the optimal spatial transformation between images by an evaluation of all possible pairs of feature matches.[17] This method can use intensities more or less directly for the image registration. It compares intensities between a transformed version of the image and the fixed (reference) image, utilizes pixel by pixel evaluation within the region, and then applies inverse mapping at each pixel. This can create problems in the sense that inverse mapping of a pixel may not 'land' on a discrete pixel location. In that case interpolation is used: nearest neighbor, bilinear or trilinear (in 3D), spline or sinc. Global polynomial transformation uses a set of matched points to generate a single optimal transformation.

In edge-based techniques, edge-enhanced images (generated from the reference and destination images) are processed to extract straight line segments, which are then grouped to form triangles. A set of candidate transformations is determined by matching triangles from the reference and destination images. The transformations are evaluated by matching the transformed set of reference (source) segments to the set of destination segments.[18] For typical image registration problems, the sources of differences between two images fall into the following categories:

- Differences of alignment between images are caused by a spatial mapping from one image to the other. Typical mappings involve translation, rotation,

warping, and scaling. Changing the orientation or parameters of the imaging sensor can cause differences of alignment.

- Differences from occlusion (one object partially hidden by another) occur when part of a finite image moves out of the image frame or new data enters the image frame of a finite image due to an alignment difference, or to an obstruction coming between the imaging sensor and the object being imaged.
- Differences from noise occur from sampling error and background noise in the sensor, and from unidentifiably invalid data introduced by sensor error.
- Differences due to change are actual differences between the objects or scenes being imaged. It may be impossible to distinguish between change and noise.

Most often, images are registered to facilitate detecting the changes in a scene; successful registration detects and undoes (or accounts for) differences due to alignment, occlusion, and noise while preserving difference due to change. Registration algorithms must assume that change is small with respect to the content of the image; that is, the images being registered are assumed to be “visibly similar" after accounting for differences due to alignment, occlusion, and noise. In addition, a sufficient amount of the object or scene must be commonly visible in both images. Often, algorithms require that at least 50% of the content of the reference image also be present in the pattern to be registered against it. In practice, medical sensors can

usually be oriented with enough precision for images to share 90% or more of their content.

The most promising automatic registration algorithms are based on the Fast Fourier Transform (FFT), such as the Fourier-Mellin transform. The Fourier-Mellin transform is a useful mathematical tool for image registration because its resulting spectrum is invariant in rotation, translation and scale. The FFT's conversion to log-polar coordinates converts the scale and rotation differences to vertical and horizontal offsets that can be measured. A second FFT gives a transform-space image that is invariant to translation, rotation and scale; this transform is the Mellin transform of the original image.

Using the Fourier Transform for Automatic Image Registration

Essentially the Fourier transform equations of a 2-dimensional function are

Eq. 4. $$H(u,v) = \iint h(x,y)e^{-i2\pi(ux+vy)}dxdy$$

where

$i = \sqrt{-1}$ and $e^{\pm ix} = \cos(x) \pm i\sin(x)$

and

Eq. 5. $$h(x,y) = \iint H(u,v)e^{i2\pi(ux+vy)}dudv$$

For the automatic registration algorithm we depend on the shift theorem and correlation theorem for the Fourier transform. Appendix E provides a review of the Fourier transform.

Determination of the Translation, Rotation and Scaling Values

From the shift theorem of the Fourier transform, Fourier transformed objects have different complex phase factors and based on that information a corresponding shift between the two images is found. Appendix F gives a description of the logic and mathematics used for the determination of the shift, scale and rotation values.

The method was developed and proposed by B.S. Reddy and B.N. Chatterji in 1996[21] and underwent many interpretations. The algorithm developed for the automatic image registration uses basic approach underlined by H. Xie at al.[22] The algorithm utilizes properties of the Fourier and log-polar transform. By using log-polar transformation, one can obtain the rotation and scaling; remove these, then you can get the shift.

Consider an image $i1(x, y)$ and another image $i2(x, y)$ which is a translated, rotated and scaled copy of image $i1(x, y)$, i.e.

Eq. 6. $$i2(x, y) = i1\left(\sigma[\cos\alpha x + \sin\alpha y] - x_0, \sigma[-\sin\alpha x + \cos\alpha y] - y_0\right)$$

where σ is the scale factor, α is the rotation angle, and x_0 and y_0 are translation shifts.

The corresponding Fourier transforms $I1(u,v)$ and $I2(u,v)$ are related by

Eq. 7. $$I2(u,v) = e^{-i\phi_{i2}(u,v)}\sigma^{-2}\left|I1\left(\sigma^{-1}[u\cos\alpha + v\sin\alpha], \sigma^{-1}[-u\sin\alpha + v\cos\alpha]\right)\right|$$

where $\phi_{i2}(u,v)$ is the frequency phase of the image $i2(x,y)$. $\phi_{i2}(u,v)$ depends on the translation, rotation and scaling, but the frequency magnitude $abs(I2(u,v)) = |I2(u,v)|$ is invariant for translation:

Eq. 8. $$|I2(u,v)| = \sigma^{-2}\left|I1\left(\sigma^{-1}[u\cos\alpha + v\sin\alpha], \sigma^{-1}[-u\sin\alpha + v\cos\alpha]\right)\right|$$

The above equation shows that a rotation of image $i1(x,y)$ rotates the frequency magnitude by the same angle α, and that image scaling of σ scales the frequency magnitude by σ^{-1}.

However at the frequency space origin $(u=0, v=0)$ there is no change to rotation or scaling. Rotation and scaling can thus be resolved in this frequency space origin by defining the frequency magnitude of $i1$ and $i2$ in polar coordinates (r,ϕ):

Eq. 9.
$$I1_{pol}(r,\phi) = |I1(r\cos\phi, r\sin\phi)| \qquad for \quad 0 \le r < \infty, \;\; 0 \le \phi < 2\pi$$
$$I2_{pol}(r,\phi) = |I2(r\cos\phi, r\sin\phi)| \qquad for \quad 0 \le r < \infty, \;\; 0 \le \phi < 2\pi$$

thus leading to

Eq. 10. $$I2_{pol}(r,\phi) = \sigma^2 I1_{pol}(r/\sigma, \phi - \alpha)$$

It can be seen from this equation that an image rotation (α) shifts the image along the angular axis, while a scale change (σ) is reduced to a scaling along the radial axis and magnifies the intensity by σ^2. To further reduce this scaling to a shift, a logarithmic scale for the radial coordinate is used, i.e. log-polar transformation:

Eq. 11.

$$I1_{\log-pol}(\xi,\eta) = I1_{pol}(r,\phi)$$
$$I2_{\log-pol}(\xi,\eta) = I2_{pol}(r,\phi) = \sigma^2 I1_{\log-pol}(\xi-\rho,\eta-\alpha)$$

where $\xi = \log(r)$ and $\rho = \log(\sigma)$.

Now both rotation and scaling are simple translations (shifts), so that taking a Fourier transform of these log-polar transformations reduces rotation and scaling to phase shifts, so that the magnitudes of two images are the same. This process is known as the Fourier-Mellin transform.

Automatic Image Registration Algorithm

The algorithm implemented for this project uses the Fourier-Mellin transform for automatic image registration. The sequence of steps is:

- I1 is reference (plan), and I2 is plate/film
- FFT is applied to both images
- Absolute values of FFT-ed images are computed
- High pass filter is applied on the result (for noise removal[23])

- Filtered FFT-ed magnitudes of both images are transformed from Cartesian to log-polar coordinates
- FFT is applied to the log-polar data
- Ratio of the two FFT-ed log-polar images is computed
- Inverse FFT of the ratio is calculated
- Absolute value of the inverse FFT of the ratio is computed
- Maximum value of the absolute value of the inverse FFT of the ratio is obtained as well as the position of this maximum
- Angle and scale needed for the automatic image registration is generated from the obtained position of the maximum
- The second image (image I2) is rotated and scaled using the calculated values; this new image (I3) represents a shifted and rotated version of image I2
- The translation calculation for the reference image I1 and image I3 is done
- Corresponding ratio is computed
- Inverse FFT of the calculated ratio is done
- Position and value of the maximum of the inverse FFT of the ratio is obtained
- From the position of the maximum, the shift value is obtained and used to shift image I3; image I4 is generated as a result.

Our algorithm is written in IDL and uses built-in IDL functions, such as reading in TIFF files and doing FFTs, whenever possible. No attempt was made to optimize the program for memory usage or execution time. This automatic registration was used for the comparisons presented in the next chapter.

There are some known and observed limitations to this algorithm.

- Both images must be the same size and square (number of rows = number of columns)
- The size of the images, for best registration results, should be at least 700 pixels
- The pixel size in both images, for best registration results, should be the same (we did tests using different pixel sizes; with some minor modifications the algorithm was capable of handling these cases too)
- Both images must represent the same type of data (i.e. dose values; this algorithm won't work to register PET and MRI images for example)

The beauty of this algorithm lies in the fact that not only can it be used for the registration of the images as a part of the IMRT analysis, but it may also find its place in other medical physics areas that need such registration implemented: in tomotherapy to obtain necessary shifts for the patient repositioning at the day of the treatment in comparison to the CT data used for planning purposes (this is now usually done with the help of fiducial markers placed under the patient's skin or

using the bony structures (spine for example)); in portal imaging for patient positioning assessment; etc. The easiest implementation may be in tomotherapy since both images consist of the same type of data. Getting this algorithm to work for different types of images (like CT and MRI for example) could perhaps be accomplished via algorithm modifications and represents an area that needs further development. A few tests were done where some requirements of the algorithm were relaxed enough for CT and MRI images to be registered (which is an interesting avenue to pursue). We plan to continue this investigation.

A potential concern for the automatic registration algorithm was that because it uses rescaling it won't be able to pick up any error in field size that occurred during the exposure, but after the procedure described above any difference in the field size will be fully visible while comparing the profiles; otherwise the registration program will show a rescaling value different than 1 being used for the registration.

Patient-Specific IMRT QA (Analysis)

For the patient-specific IMRT QA, items that need to be validated include: monitor units delivered (or absolute dose to a point), MLC leaf sequences or fluence maps, and dose distribution.

In film dosimetry this is done with IMRT plan/film analysis, plan/film profiles and isodose lines examination. During the planar dose extraction, the maximum dose point on the fluence map is manually chosen and the dose rate for that point (with the point's coordinates) is recorded. Once the film is scanned,

calibrated and cropped, the same point on the film is selected. The value at this point is compared to the value obtained from the plan. The two values should agree within 5%. In the second step, plan and film images are registered and vertical and horizontal profiles are compared (the profiles are usually chosen to go through the maximum dose point). Profiles are usually reported in absolute dose. As a last step, film isodose lines are generated (also in absolute dose).

On the other hand diode arrays like MapCheck compare normalized values (normalized to a 'best fit' point) and display points (diodes) that do not fall within criteria (3% and 3 mm DTA – distance to agreement). In this case isodose lines and profiles are normalized. The point used for both absolute dose comparison and normalization is chosen from the area where maximum dose is delivered (a low gradient and low modulation area).

We followed these common practices when our program for IMRT analysis was developed. The same rules were applied as for film: the point for absolute dose comparison is the maximum dose read on plan and plate images, the position of the maximum point is read and displayed, two vertical and two horizontal profiles are read and compared, both normalized and absolute isodose lines are displayed for both plan and plate, and the intensity map for both images is displayed (in 2D and 3D). The results are described in the next chapter.

Results and Discussion

When the study started, a different model of CR plate was used other than the one that the study was finally finished with (Agfa MD10). The plates used at the start were thicker and cracked easily, and that was the main reason why Kodak replaced them. Plate particles would quickly mess up the rollers in the scanner so it had to be cleaned often; consequently portal images were of very bad quality. In Figure 22 two white lines are clearly visible; they are the result of plate debris that fell into the scanner and stuck to the rollers. If the lines and other artifacts were in the exposed area, accurate analysis (dosimetry) would not be possible. In this paper, the original set of plates will be referred to as 'old' and the Agfa MD10 plates used later on as 'new'. For all the tests, plates were randomly selected; we didn't just use one plate over again. This was done mainly because the goal of the study was to explore the possibility of CR plates being good replacements for film dosimetry. Also, if only one plate was used for all the measurements, a considerable amount of time would be lost just waiting for that plate to be erased each time. As one sees hereafter, the plates all show similar (one can even say same) behavior.

Several different tests were done throughout the course of the study. All the exposures with the old plates were done with 4 MV only; exposures with all energies were made with the new plates. After the first few exposures of the study were done,

the Kodak scanner was serviced. The values read on the plates changed considerably after the service.

Figure 22. CR plate image

Lead vs. No Lead Plate Exposure

Several exposures were done using lead sheets ranging from 1 mm to 10 mm thick; we then repeated the exposures with the same number of monitor units delivered but without the lead. Table 3 shows results for 1 mm lead vs. no lead. It can be noticed that even though the absolute difference between values read is comparable for all MU delivered, the relative percentage difference increases with higher numbers of MU delivered because of the smaller magnitude of the RGB

values. Due to issues related to handling of the plates with lead sheets while doing hundreds of exposures (time consuming and contamination is a possibility), it was decided to continue with the exposures without using the lead. Exposures with lead were done only with 4 MV, and different lead thicknesses used gave similar results to those presented in Table 3.

Table 3. Exposure with lead vs. without (4 MV) – 'old' plates used

	RGB values read in center of 5 x 5 area		
MU	**1 mm lead**	**no lead**	**% difference**
5	79	76	3.9
10	50	48	4.2
15	32	33	-3.0
20	20	22	-9.0
25	10	11	-9.0
30	0	0	0.0

Multiple Exposures vs. One Exposure Per Plate

Exposures on different days with the same number of monitor units were done to be able to establish if one calibration curve will be enough for all plates. Measurements were repeated both for one exposure per one plate and for multiple exposures per plate with the same number of monitor units. Figure 23 shows sample images.

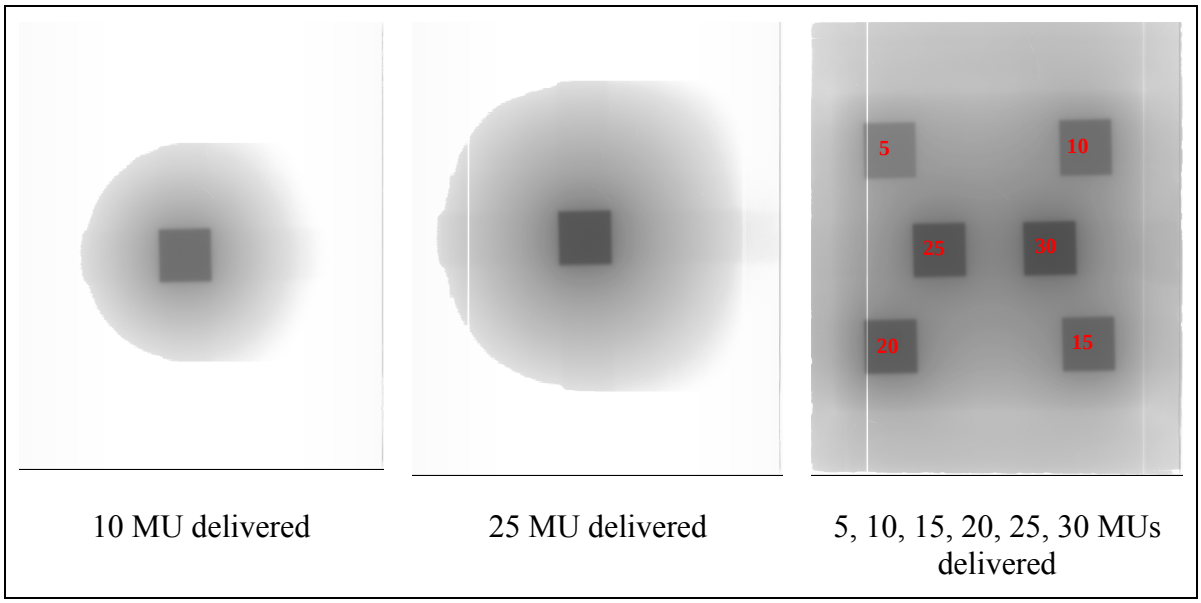

Figure 23. One exposure per plate vs. multiple exposures per plate

Table 4. Multiple exposures vs. one exposure per plate

	Separate Plates			All on 1 Plate			All on 1 Plate		% Difference		
Image #	MUs	Value	Image #	MUs	Value	Image #	MUs	Value	Sep.* - #17	Sep.* - #18	#17 - #18
7	10	**111**	17	10	**110**	18	10	**110**	0.9	0.9	0.0
8	15	**102**		15	**100**		15	**NA**	2.0	NA	NA
9	20	**90**		20	**91**		20	**90**	-1.1	0.0	-1.1
10	25	**86**		25	**85**		25	**NA**	1.2	NA	NA
11	30	**80**		30	**79**		30	**NA**	1.3	NA	NA
13	40	**75**		40	**NA**		40	**74**	NA	1.4	NA
14	60	**64**		60	**NA**		60	**63**	NA	1.6	NA

* % difference in values read for one exposure/plate (separate image) vs. multiple exposures/plate (all on one image)

Delivering a higher dose (more monitor units) results in darker values. The values read showed little difference (all differences were less than 2%); Table 4 presents part of the data that is representative of the obtained values.

Cassette vs. No Cassette Exposure

Exposures were also repeated for several monitor units with and without the cassette, with typical results shown in Table 5. Again due to handling issues (cassettes are heavy and hard to manipulate), and because the presence of the cassette does not make considerable difference in the result, plates without the cassette were used for all remaining measurements.

Table 5. Plate in cassette vs. plate in envelope – typical result

MUs	Value with Cassette	Value without Cassette	% difference
10	112	110	1.8
15	104	102	2.0
20	91	94	3.2
25	86	86	0.0
30	80	80	0.0

Time Decay Analysis

An analysis of the decay of the plate images with time was done for a limited number of exposures. The results are presented in Table 6. Additional analysis was not done.

Table 6. Decay analysis

	RGB value			
MU	Scanned 5 min after x-ray exposure (before scan plate was exposed to bright flash light)	Scanned immediately	Scanned after 10 min	3 min bright flash light exposure
30	1	80	83	40
	Scanned immediately	Plate exposed on reverse side and scanned immediately		
5	130	2		

It is obvious that by exposing the irradiated plate to bright light (a flash light was used) the plates become overexposed. For example if plate was scanned immediately after exposure or 10 minutes after it was exposed to same number of MUs (30), the values read were almost the same. But if the plate was exposed to 30 MUs and then before scanning taken out of envelope and flashed with a bright light, the results read after the scanning of these plates changed considerably. This actually shows why Kodak does recommend for plates to be read and used in areas with dim light. One of the plates that was exposed to 5 MUs was exposed backwards, i.e. the white side of the plate was not facing the x-ray source, but rather its back. The plate was scanned normally. We wanted to see what would be the result if someone turned a plate upside down unintentionally and exposed it that way.

Further Analysis of the Plate Behavior

Over the days, several different exposures were made using the same number of monitor units (Table 7). Numbers in blue font in Table 7 belong to plate exposures that showed a strange 'overexposure' behavior. Table 8 shows the range and percentage differences for the data excluding the overexposed plates. Percentage differences shown represent percentage difference between the minimum and maximum values read for the particular number of MUs delivered. We also investigated the effect of taking the plate out of the erasure drawer after different amounts of time after the plate was erased (Table 9).

Table 7. Several plates exposed in two days

	1st day									2nd day				
Plate number / MU	1	2	3	4	5	6	7	8	9	1	2	3	4	5
5	122	124	122	81	67	123	122	80	121	121	122	121	121	121
10	107	107	106	60	44	107	106	61	105	106	106	105	104	105
15	99	98	/	/	30	97	/	/	/	/	/	/	/	/
20	90	90	89	37	19	90	90	38	89	89	89	89	89	89
25	82	83	/	/	9	83	/	/	/	/	/	/	/	/
30	78	77	/	/	1	78	/	/	/	/	/	/	/	/
40	/ *	/	73	15	/	/	72	15	72	73	73	72	72	72
60	/	/	61	2	/	/	61	2	60	61	61	61	60	61

* "/" means that these MU values were not delivered to the plates in question

Table 8. Percentage difference range

MU	RGB value range	% difference
5	121 - 124	2.4
10	104 - 107	2.8
15	97 – 99	2.0
20	89 - 90	1.1
25	82 - 83	1.2
30	77 - 78	1.3
40	72 - 73	1.4
60	60 - 61	1.6

Table 9. Erasure time dependence

MU	**Plate number**				
	2	**3**	**4**	**5**	**6**
5	81	122	81	122	123
10	60	107	59	106	106
20	38	90	37	90	89
40	16	73	16	73	73
60	2	61	2	61	61

Before the study was done to obtain the results shown in Table 9, first the plate was erased (#1) and then exposed. The rest of the plates were handled as follows:

- #2 – taken from previously cleaned plate (#1)
- #3 – was taken from scanner immediately after erasure
- #4 – was taken out 5 min after erasure finished
- #5 - was taken out 10 min after erasure finished
- #6 – was taken out immediately

Again some of the plates showed overexposure and since the study was not repeated, one cannot distinguish if it had anything to do with the erasure time or if it was just 'random behavior'. Plates behaving 'normally' showed no significant difference in values from the plates in Table 7. Several more exposures were done using the same number of monitor units and the values always fell within the range specified in Table 8. The question is what is the cause of the differences in values measured for the same number of MUs? There are some potential error sources. For instance, inaccuracy in the LINAC output and/or MLC controls (in a case of patients' plan delivery), CR plate response (reader system included), fluctuations in the scanner output, the quantization error or mistakes made by the person performing the IMRT QA, might be some error sources. Sources of error in CR system include structure noise (phosphor in CR plate), statistical fluctuations in amount of PSL emitted for certain amount of latent energy stored in phosphor, and fluctuations in PMT output. In all cases standard deviation may be approximated by the square root of the average or single measurement if no more than two measurements are

available (assuming Gaussian statistics). Thus the results shown in Table 8 represent reproducibility of the plates and show that it is on the order of 2%.

Excluding the 'random behavior', the plates performed consistently from day to day and exposure to exposure. Thus we concluded that one calibration curve could be used all the time. There is no need to do separate calibration curves every time IMRT QA is performed, as it is done now in film dosimetry. Appendix G provides the results of a separate study that shows the large variations in calibration values encountered in film dosimetry, depending on when the exposures are done.

This study of erasure time dependence was done only for the 'old' plates and it was not repeated for the 'new' ones. Both 'old' and 'new' plates exhibited the 'random overexposure' behavior.

IMRT Analysis

Using 'Old' Plates

In the first IMRT exposures (done with 'old' plates), we tried to follow the film dosimetry procedure. At first, the RIT113 system was used, but it had problems with reading Kodak DICOM images, as discussed previously. Also the calibration curve results did not look very promising; Figure 24 compares film and plate calibration curves determined with the RIT113 software. Figure 25 shows the calibration plate image for 20, 40, 60 and 80 MU.

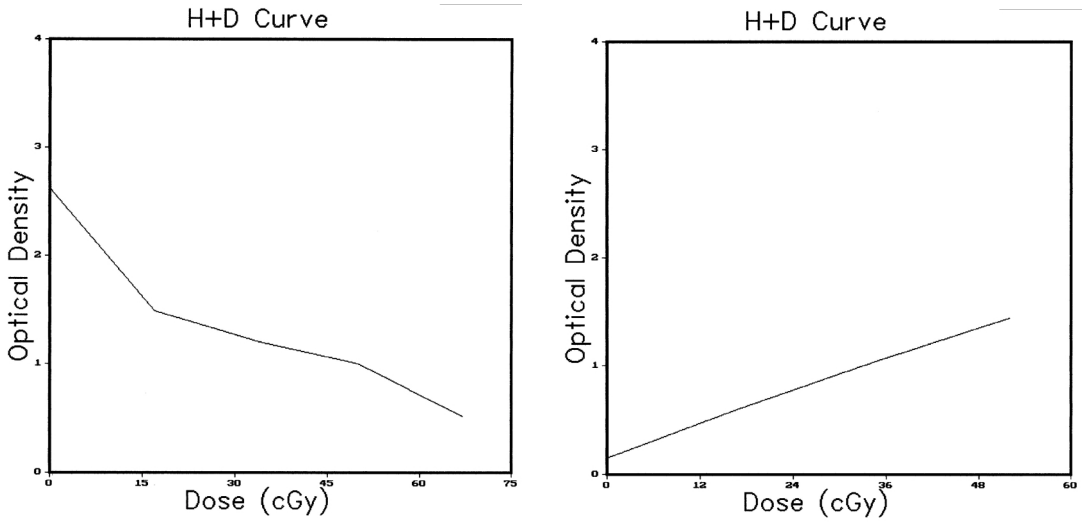

PLATE FILM

Figure 24. Example of calibration curve done with RIT113 v. 3.14

After the IMRT analysis algorithm was developed, the analysis for the plate image in Figure 25 was repeated. Figure 26 shows the calibration curve that was generated and used in the analysis. Using the plan calibration curve shown in Figure 13, an 'old' plate was used to deliver one patient IMRT QA plan. The resulting plate image, a dose profile, and isodose contours are shown in Figure 27 for one of the delivered fields.

It is obvious that four points for the calibration curve are not enough to accurately represent all the values on the plate image; a curve with more measured points is needed.

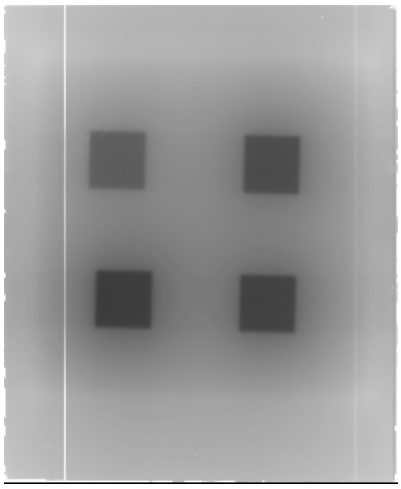

Figure 25. Plate calibration image

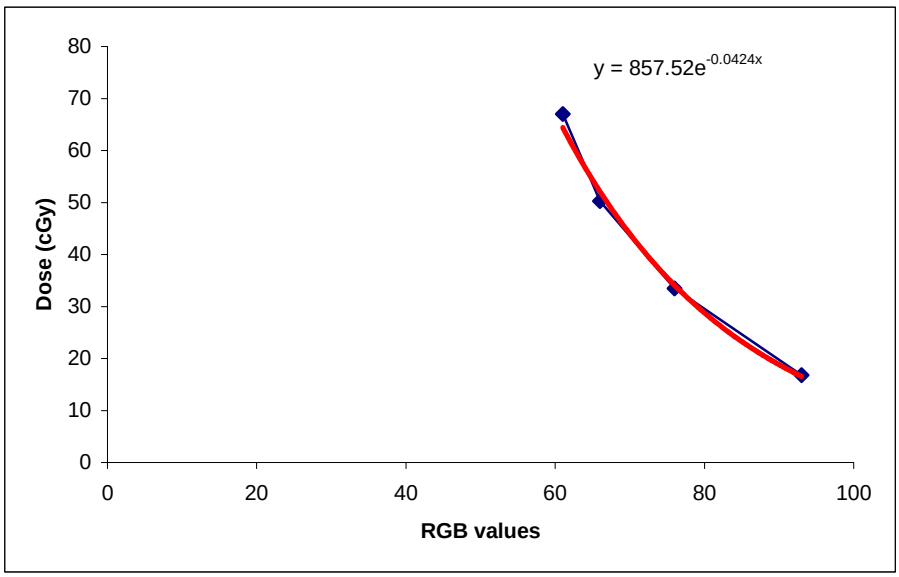

Figure 26. Plate calibration curve (4 MV), trendline in red

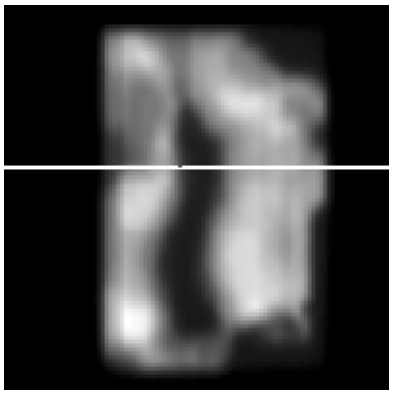

Profile Location

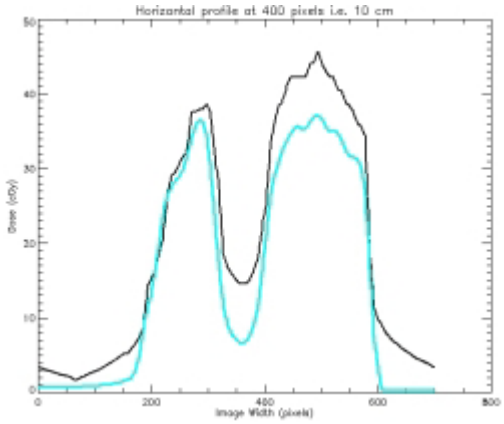

Profile, plan is blue

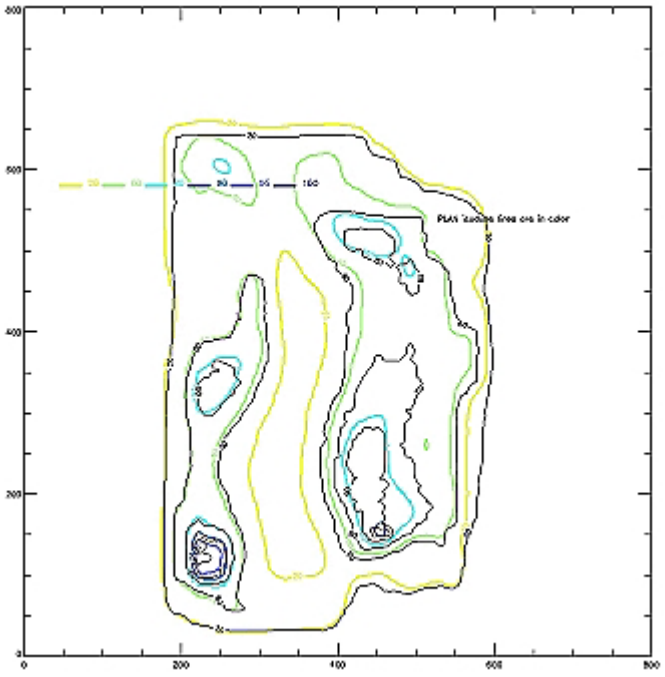

Isodose Lines (in %)

Maximum value in Plan array is:
53.3530
The maximum value of Plan is at location
(18, 828)

Maximum value in Plate array is:
59.3139
The maximum value of Plate is at
location (18, 828)

Percentage difference: 11%

Figure 27. First results

Analysis was repeated using a calibration curve obtained with 10 points; Table 10, Figure 28 and Figure 29 show the results.

Table 10. Calibration points (4 MV)

MU	RGB value	Dose (cGy)
3	143	2.51414
4	136	3.352187
7	121	5.866328
10	112	8.380468
15	104	12.5707
20	91	16.76094
25	86	20.95117
30	80	25.1414
40	76	33.52187
60	65	50.28281

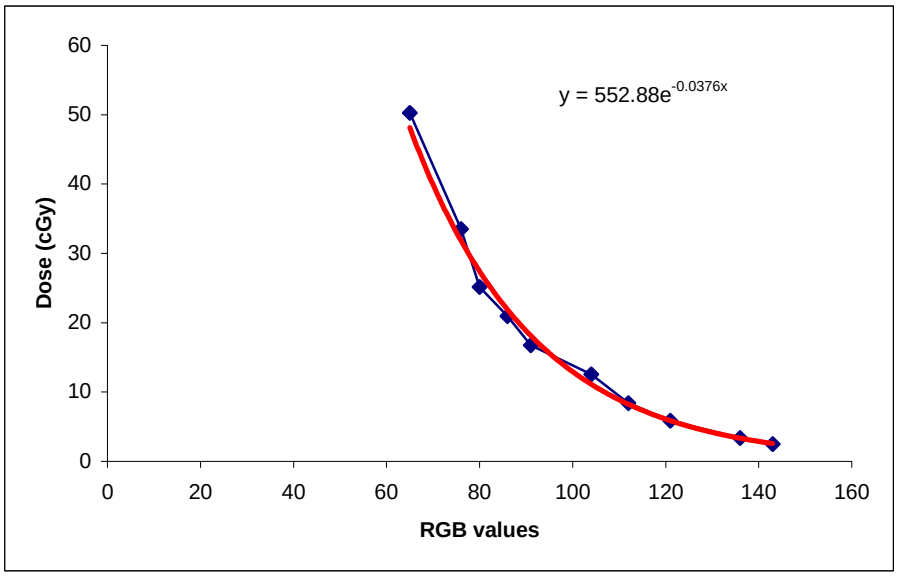

Figure 28. Calibration curve (4 MV)

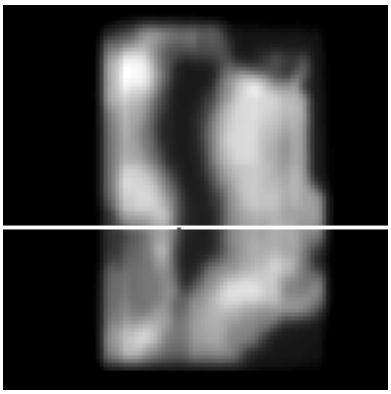

Profile Location

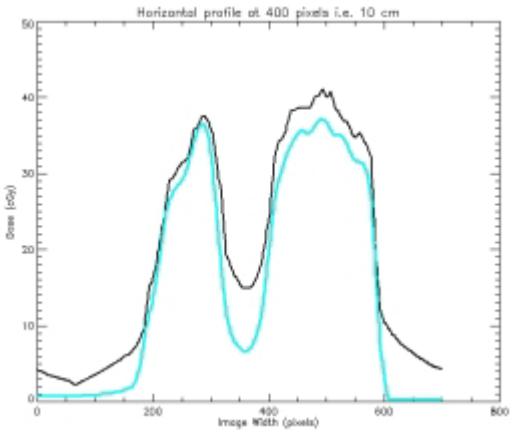

Profile, plan is blue

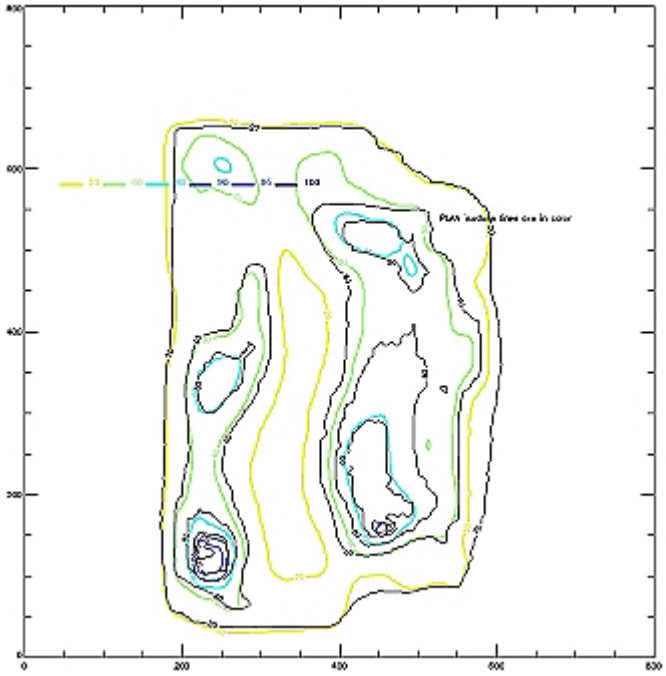

Isodose Lines (in %)

Maximum value in Plan array is: 53.3530
The maximum value of Plan is at location (18, 828)

Maximum value in Plate array is: 51.7457
The maximum value of Plate is at location (18, 877)

Percentage difference: -3%

Figure 29. Second results

It may be noticed that for the ranges given in Table 8, the values reported in Table 10 fall outside that range. The exposures and measurements done for this patient plan were done after plates were cleaned with the Kodak-recommended solution. After this cleaning, we did not repeat exposures to establish a range of values like the ones reported in Table 8.

From the figures, it is obvious that a curve with more points gives better results if only profiles are compared. Unfortunately further analysis with this kind of plate was not possible because they were soon replaced with the Agfa MD10 plates and rest of the study was done using those plates.

Using 'New' Plates

Calibration Curves Used

The data used for the generation of the calibration curves shown in this section are presented in Appendix H. Calibration curves data were obtained in 1 MU intervals, using both single and multiple exposures per plate; exposures were done on different days.

An exponential trend of values from the plate images was observed. Each data set in Appendix H was graphed in MS Excel and an exponential function was fitted through the data points. Figure 30 through Figure 32 show the calibration curves for 4 MV, 6 MV, and 10 MV, respectively.

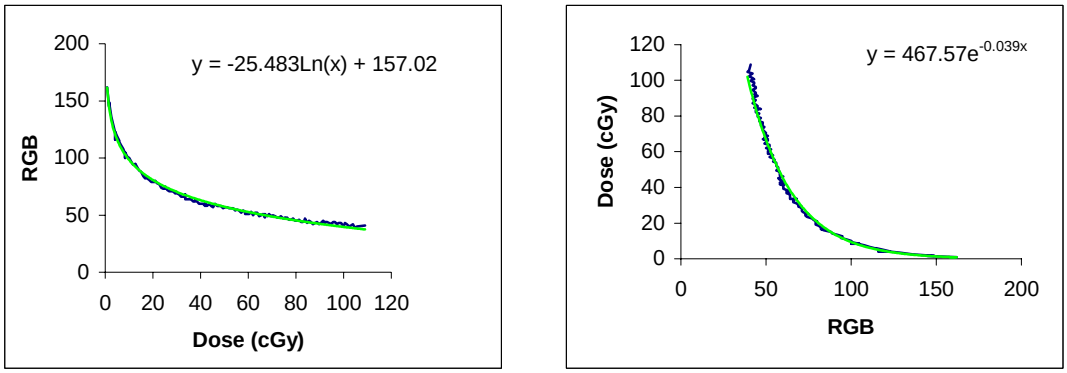

4 MV curve with all the values delivered used

Figure 30. 4 MV plate calibration curves

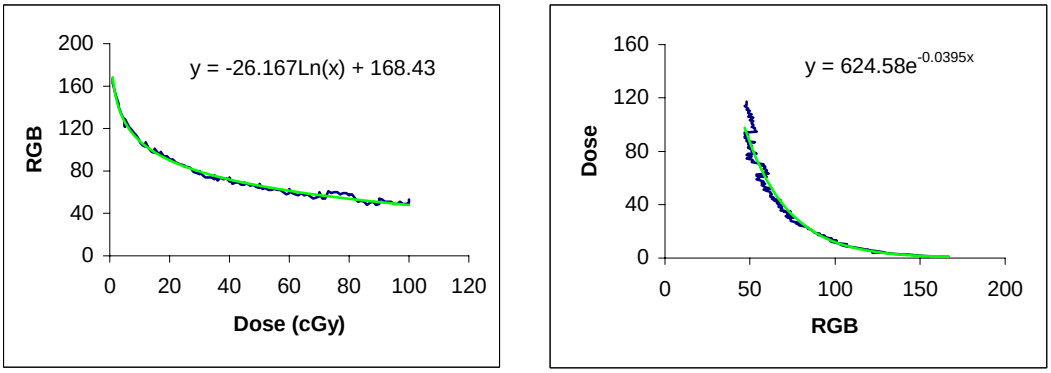

6 MV curve with all the values delivered used

Figure 31. 6 MV plate calibration curves

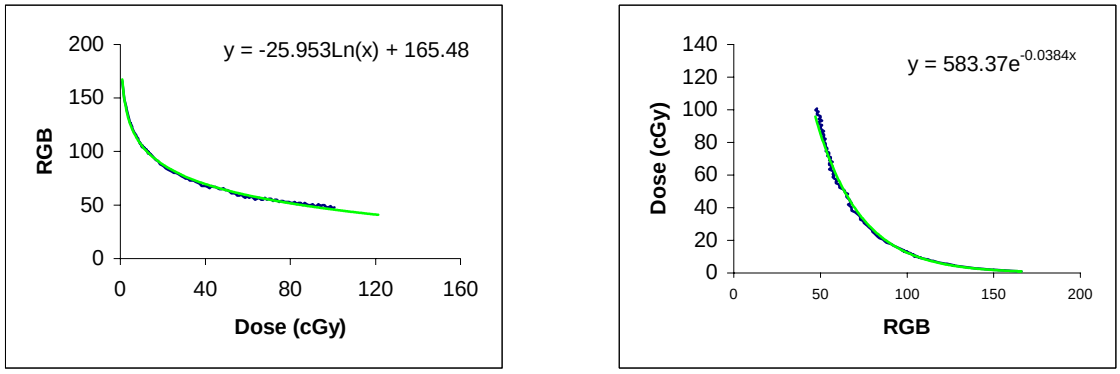

10 MV curve with all the values delivered used

Figure 32. 10 MV plate calibration curves

Different calibration curve values were used for different fields in the IMRT analysis program depending on the maximum dose expected in the field, i.e. if maximum dose expected was 60 cGy, the curve that goes up to that dose value was used first. Theoretically the full curve is the best fitted function because it has the most data, so for all the cases presented analysis was done with the full calibration curve too. In some cases, calibration curves based on fewer points produced better results, but in most cases the calibration curve using the most data points gave the best results for all energies tested.

When comparing results based on the two calibration curves used, the difference was in most cases barely noticeable. Figures in continuation (see Figure 33 and Figure 34) compare typical plans for 4 MV and 6 MV (on all graphs, plan values are always in color). Differences, as expected, were the least in the normalized isodose lines comparison. If profiles were done using normalized values,

the differences will be practically invisible. As expected in most cases, the curve with the most calibration points gave best results. So in practice only the full calibration curve should be used. On the figures below where 0% is indicated, it means that the percentage difference between the two values was less than 0.5%.

4 MV, with the fewer points (up to 80 MU) calibration curve	**4 MV, with the maximum points (up to 130 MU) calibration curve**
Maximum value in Plan array is: 60.9020 The maximum value of Plan is at location (8, 2194) Maximum value in Plate array is: 55.6432 The maximum value of Plate is at location (7, 2152) Percentage difference: -9%	Maximum value in Plan array is: 60.9020 The maximum value of Plan is at location (8, 2194) Maximum value in Plate array is: 59.1779 The maximum value of Plate is at location (7, 2152) Percentage difference: -3%
	
Normalized isodose lines, plan values are in color	
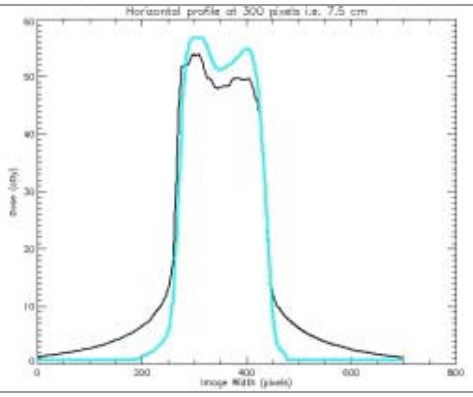	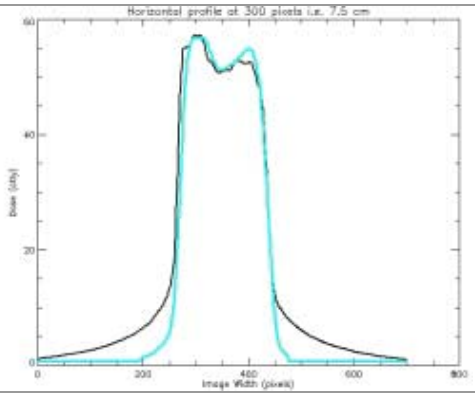

Figure 33. Comparison based on calibration curves used (4 MV)

6 MV, with the fewer points (up to 70 MU) calibration curve	6 MV, with the maximum points (up to 135 MU) calibration curve
Maximum value in Plan array is: 69.2648 The maximum value of Plan is at location (2, 2377) Maximum value in Plate array is: 63.2072 The maximum value of Plate is at location (14, 2132) Percentage difference: -9%	Maximum value in Plan array is: 69.2648 The maximum value of Plan is at location (2, 2377) Maximum value in Plate array is: 69.1400 The maximum value of Plate is at location (14, 2132) Percentage difference: 0%
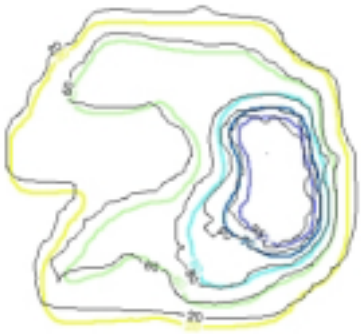	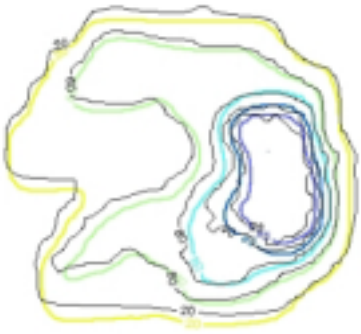
Normalized isodose lines, plan values are in color	
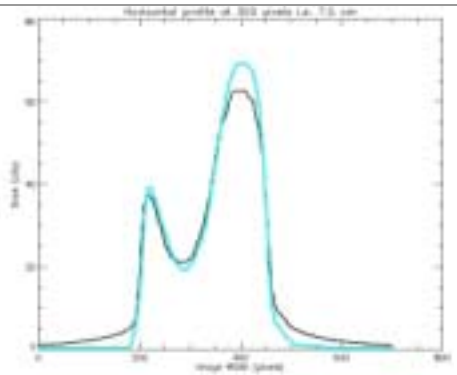	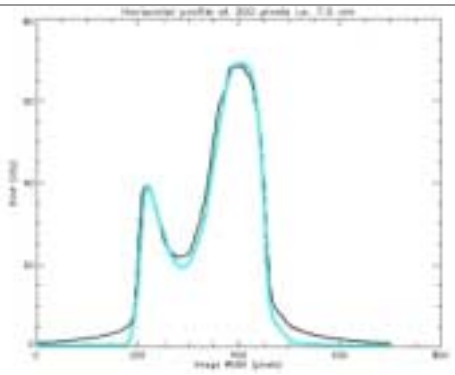
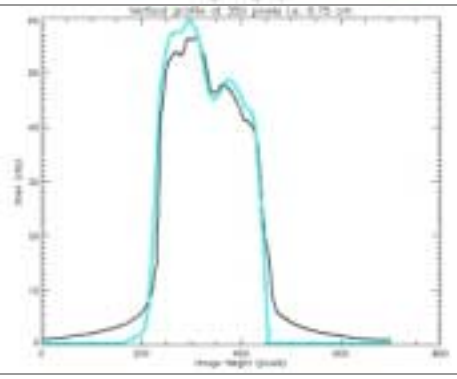	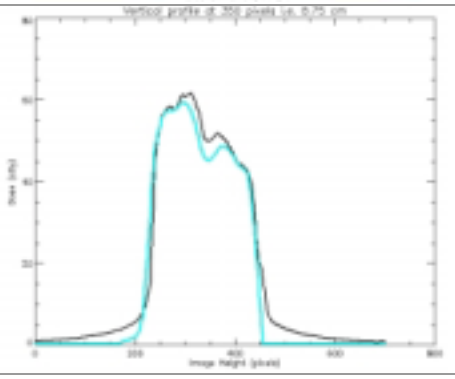

Figure 34. Comparison based on calibration curves used (6 MV)

IMRT Analysis – Output of the Algorithm Developed

TIFF format for both plan and plate images is used as the input to the developed algorithm together with the values for the corresponding calibration curves. Typical output generated after the program runs is shown in the images below.

(*Note:* For the first field some of the windows that are created as the output are left in their original background color – black, while for the second case the window's color is inverted to make the results more visible on paper.)

6 MV

1st field

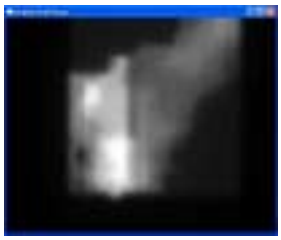

Original plan image

Original plate image

Converted plan image

Converted plate image

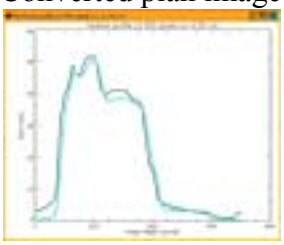

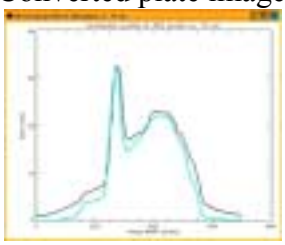

1st vertical profile

1st horizontal profile

1st field

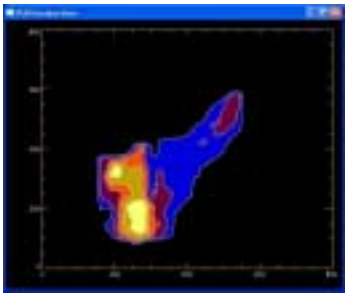

Plan isodose lines in absolute dose

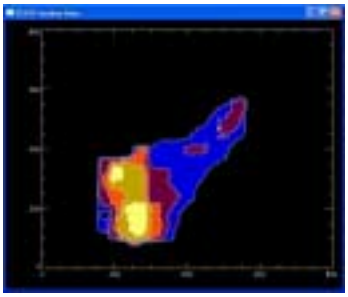

Plate isodose lines in absolute dose

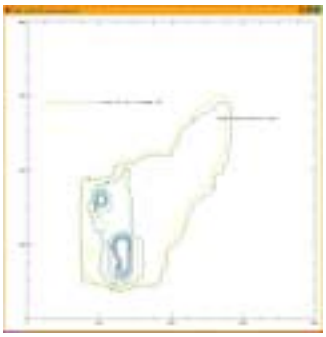

Plan and plate normalized isodose lines(normalization is done using maximum value read)

Maximum value in Plan array is: 51.6569
The maximum value of Plan is at location (63, 1269)

Maximum value in Plate array is: 51.8616
The maximum value of Plate is at location (63, 982)

Percentage difference: 0%

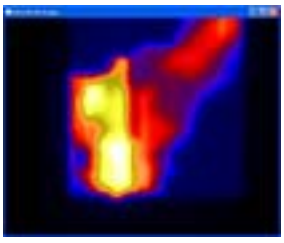

Plan fluence map

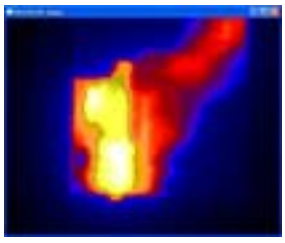

Plate fluence map

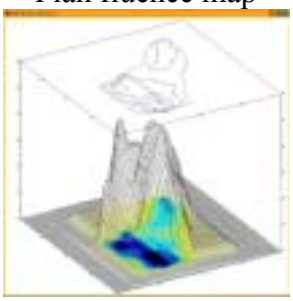

Plan 3D intensity profile

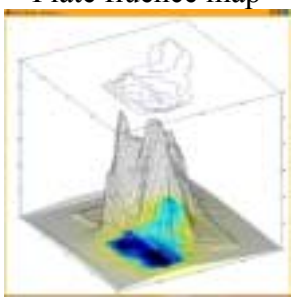

Plate 3D intensity profile

2nd field

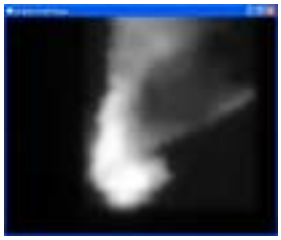

Original plan image

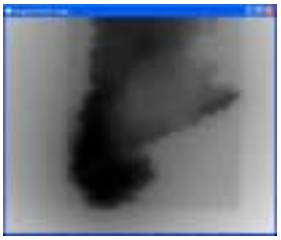

Original plate image

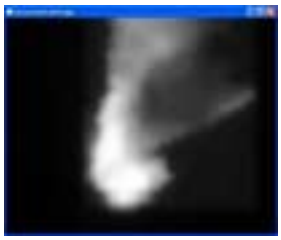

Converted plan image

Converted plate image

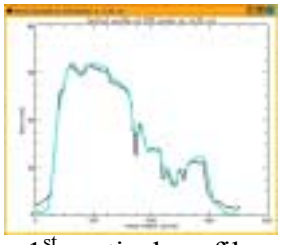

1st vertical profile

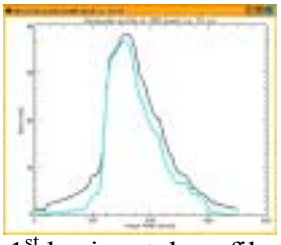

1st horizontal profile

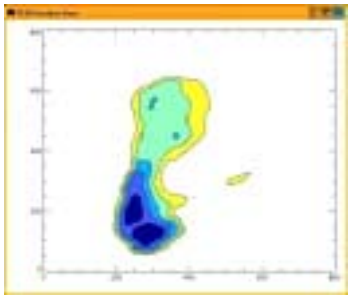

Plan isodose lines in absolute dose

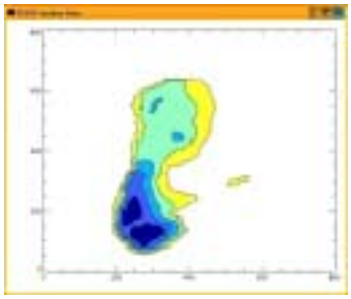

Plate isodose lines in absolute dose

2nd field

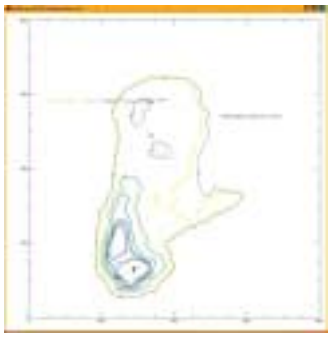

Plan and plate normalized isodose lines
(normalization is done using maximum value read)

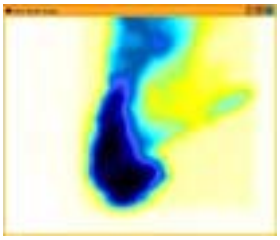

Plan fluence map

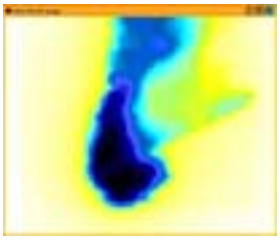

Plate fluence map

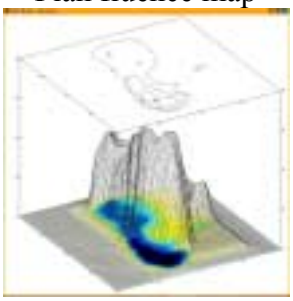

Plan 3D intensity profile

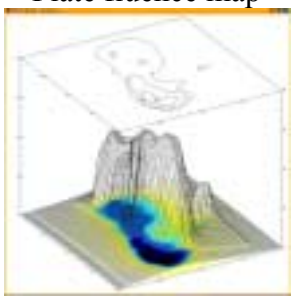

Plate 3D intensity profile

Maximum value in Plan array is: 64.1980
The maximum value of Plan is at location (85, 842)

Maximum value in Plate array is: 63.1858
The maximum value of Plate is at location (71, 646)

Percentage difference: -2%

The 6 MV plates showed the best behavior compared to the profiles generated with different patient plans with different energies, and percentage

differences in maximum absolute dose values read for all fields delivered were between –2% and 4%. The 4 MV plate behaved inferiorly when the absolute maximum dose values were compared in comparison to the other two energies. Percentage difference for all fields was within –10% to 2%, even though normalized isodose lines were a perfect match (this is the way values are checked in MapCheck for example, while for absolute dose value comparison, best values are found and often chosen purposely for reporting!). For 10 MV, same as for 4 MV, plates were usually underexposed, but the differences in maximum absolute doses were still within –8% to 0%. One reason could be the calibration curve; if a better choice of calibration curve was made the results might be better. One way of dealing with the obvious disagreements between the profiles in low dose regions is to chose a separate calibration curve for that particular range of values; another way would be by placing lead sheets on both sides of the plate (as it is done sometimes with film) to filter low-energy photons. As shown previously results were not significantly different with lead, but still for lower dose values, they were different enough to matter. And above all the same test was not done for the 'new' plates.

Contrary to 4 MV and 6 MV, the 10 MV plate was usually underexposed in higher dose regions and had better matching with planned values in lower dose regions.

Even though percentage differences for some fields seem to be quite high, higher differences are observed sometimes with film dosimetry and either neglected

if all other parameters are within acceptable limits or the exposure is repeated. There is not much sense in repeating plate exposures since its response doesn't change from day to day, although it can certainly change in relation to accidental exposure to bright light or its own 'random behavior'. Time decay of the plate data was not significant in the time frame we used for scanning each exposed plate, but it must be considered if plates are not scanned immediately after exposure.

Many of the fields had to be repeated, as they were overexposed (Figure 35). Table 11 summarizes the fractions of plate exposures that exhibited the 'random overexposure' behavior. Figure 35 compares a properly exposed plate to an overexposed plate for the same field. 6 MV IMRT fields had the lowest number of overexposed images; some patient plans were completely delivered without overexposures, even though 6 MV had the highest number of overexposed images when exposure for calibration curves was done.

The overall percentage of overexposed fields is 23.4%, meaning that roughly 23 plates will be overexposed for 100 images taken. If an average patient plan has 7 fields that must be exposed for IMRT QA, on average ~ 2 fields out of 7 must be repeated. This inexplicable behavior of the plates adversely impacts the time saving advantage that plates have in comparison to film dosimetry.

Table 11. Percentage of the overexposed fields

4 MV	% overexposed	average (in %)
Calibration Images	25.6	
Field Images	22.7	
		24.2
6 MV	% overexposed	
Calibration Images	34.8	
Field Images	15.3	
		25.0
10 MV	% overexposed	
Calibration Images	25.0	
Field Images	26.3	
		25.7
Overall %	**23.4**	

Some suggestions received in conversation with other medical physicists who are trying to use CR plates in dosimetry, were that the time between the actual exposure and scanning should be greater than 10 minutes, but if this idea is followed (note that we tried this for several exposures and still saw overexposed images), it will take 70 minutes just to scan in all the plate images if only one plate is available, and slightly faster if multiple plates are available. In this scenario any time saving advantage is eliminated.

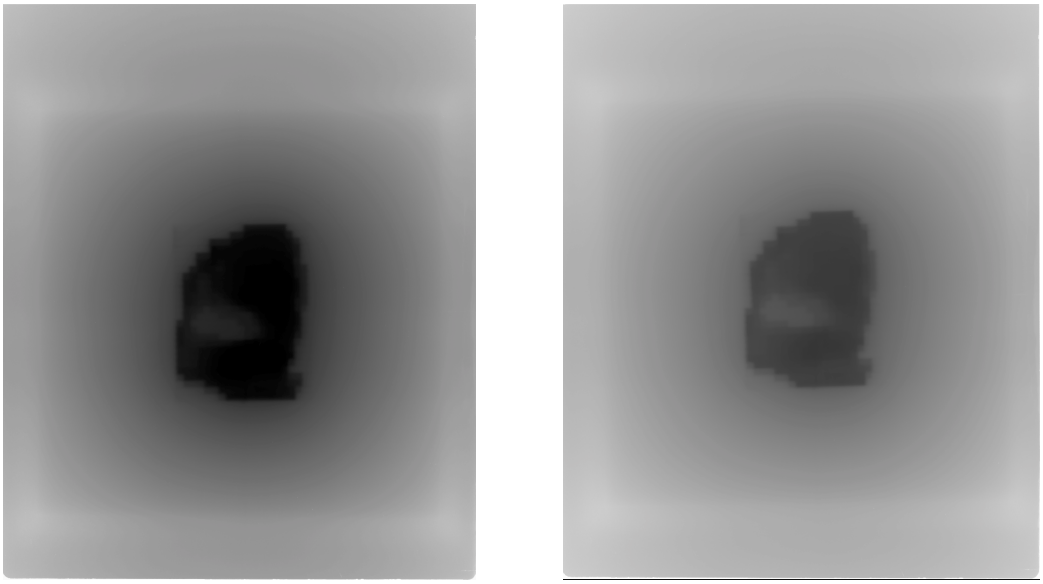

Figure 35. Same field, overexposed on left

CR Plates Calibration Discussion

As shown before, profiles mostly exhibited disagreement in low dose regions; part of the problem may be in the calibration curve used for the plates. The plate calibration curve is described with an exponential equation. A problem with the exponential calibration curve is that it never goes to zero so it cannot accurately predict plate behavior in low dose areas (where dose approaches zero). When a separate calibration function is used for low dose values, agreements in low dose areas were better. Software limitations prevented us from adequately implementing a

dual-function calibration curve in the analysis program. This is the main reason why many of the profiles show disagreement in the low dose areas of the fields.

It is obvious that even though results were good when the calibration curve used for the analysis was taken as a best fit to the maximum number of data points measured, some results strongly depended on the range of the curve used (i.e. if an exponential equation based on fewer points described the trend the best). When data points were calculated backward, using the trendline equation, they did not necessarily fall within the measured data range. A more accurate approach would be to assign to each pixel in the acquired plate image an exact measured value. The problem with this is computational time. But after all, the analysis did show that in most cases, the best fit approach (trendline) will do.

Finally, we found that one calibration curve can be used for each energy and the calibration doesn't vary over time. The same is not true for film calibration curves regardless of energy (see Appendix G).

Half vs. Full Number of MUs Delivered

In this part of the study several fields were delivered using both half and the full number of monitor units. A typical case is compared in Figure 36 and Figure 37. A slight difference is observed if the same plate calibration curve was used for the fields delivered with half and the full number of MUs delivered for all energies. On the other hand if different calibration curves were used (selected by the maximum

dose expected for the particular field), there was almost no difference in the values and profiles.

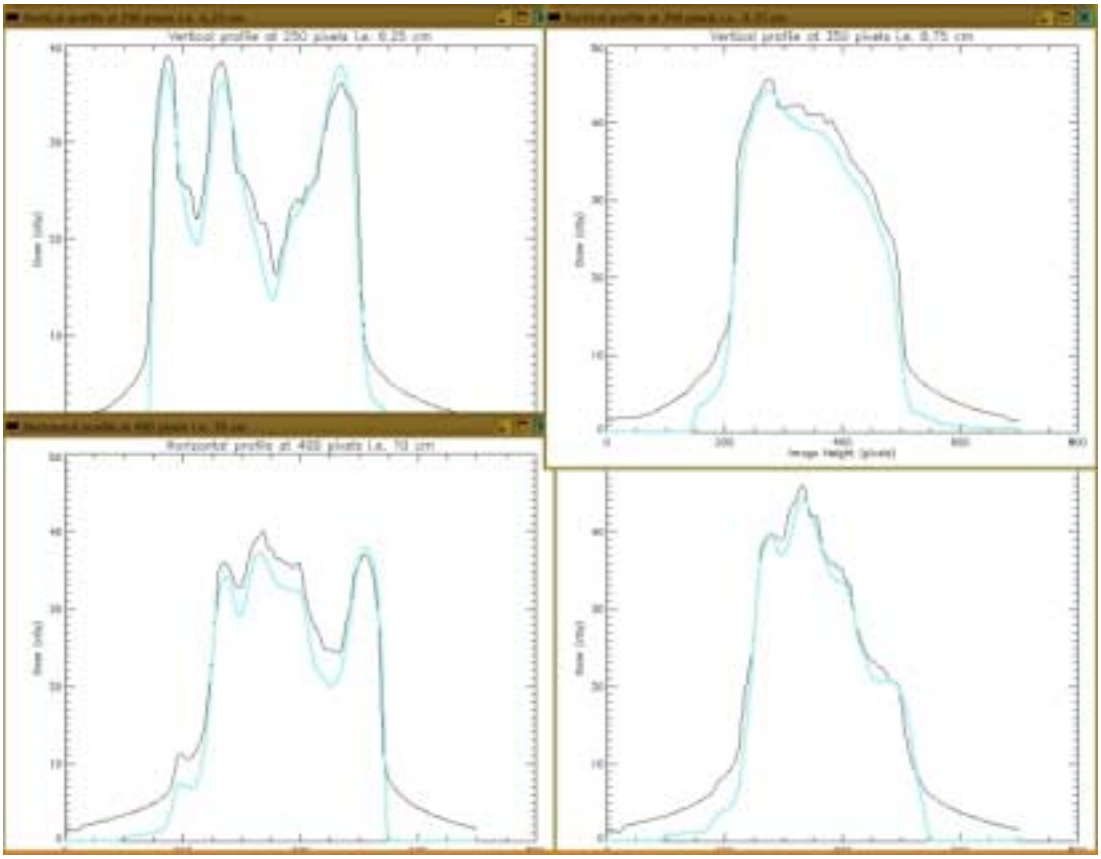

Maximum value in Plan array is: 46.3483
The maximum value of Plan is at location (38, 1928)

Maximum value in Plate array is: 48.6492
The maximum value of Plate is at location (36, 1879)

% difference: 5%

Figure 36. Full number of MUs delivered

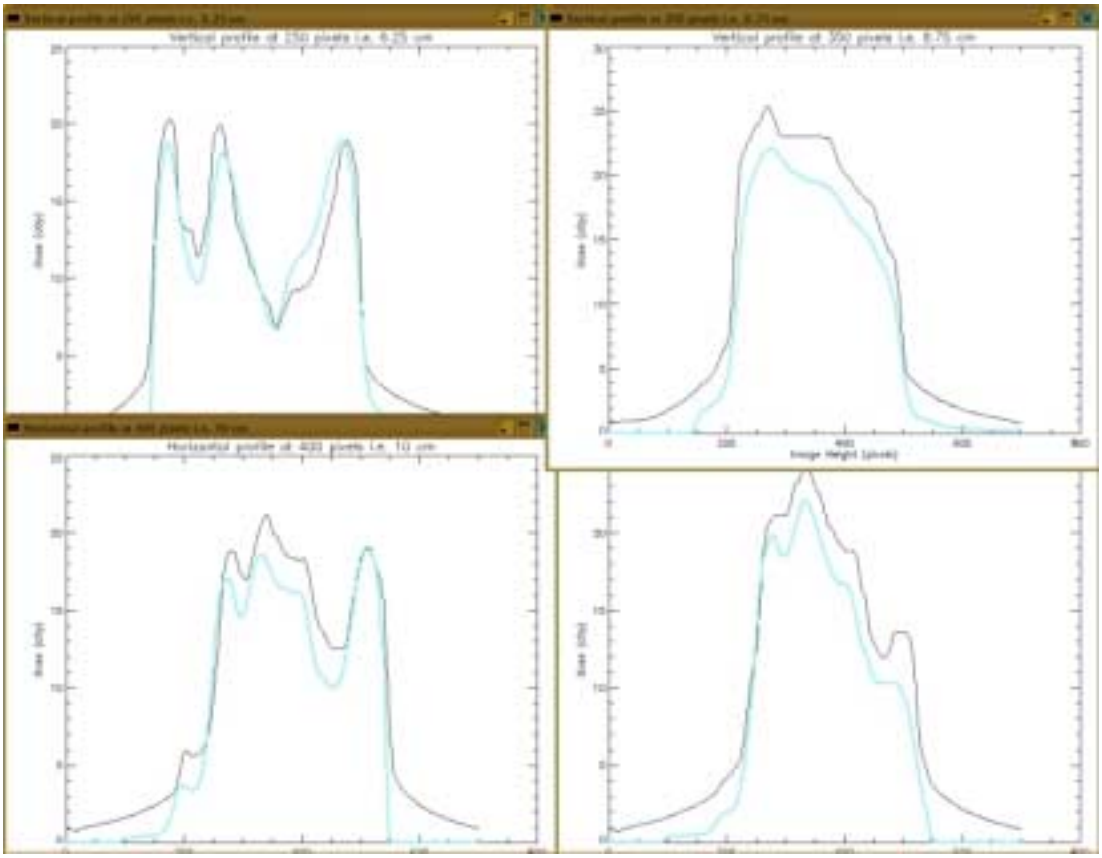

Maximum value in Plan array is: 23.1457
The maximum value of Plan is at location (38, 1928)

Maximum value in Plate array is: 25.5695
The maximum value of Plate is at location (35, 1844)

% difference: 9%

Figure 37. Half number of MUs delivered

Reproducibility

Typical results for reproducibility are shown in Figure 38 and Figure 39 (plan values are always in color). The case shown as an example in Figure 38 had fields exposed 3 weeks apart.

If the same field was exposed on the same day a couple of times subsequently, maximum value measured on the plate remained the same regardless of the number of exposures done (up to 2% difference was observed in a few cases); a slight difference was observed in the position of the maximum [(8, 2180) instead of (8, 2229) for example].

Surprisingly so, the maximum values measured on a plate for the exposures done 3 weeks apart did not show any difference for this case, but since the same exposure was not repeated again for the same field another 3 weeks apart, no particular conclusions could be drawn.

Original QA session	QA session 3 weeks later
Maximum value in Plan array is: 59.9180 The maximum value of Plan is at location (22, 2383) Maximum value in Plate array is: 58.3862 The maximum value of Plate is at location (8, 2320) Percentage difference: -3%	Maximum value in Plan array is: 59.9180 The maximum value of Plan is at location (22, 2383) Maximum value in Plate array is: 58.3862 The maximum value of Plate is at location (8, 2180) Percentage difference: -3%
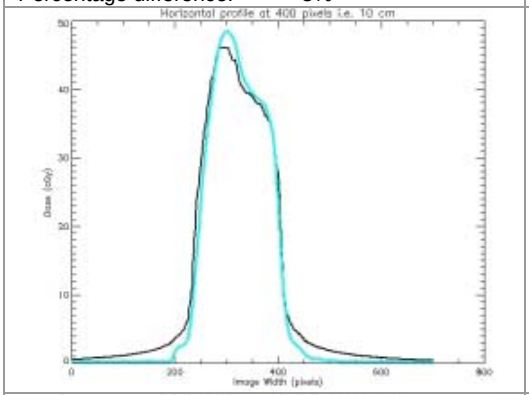	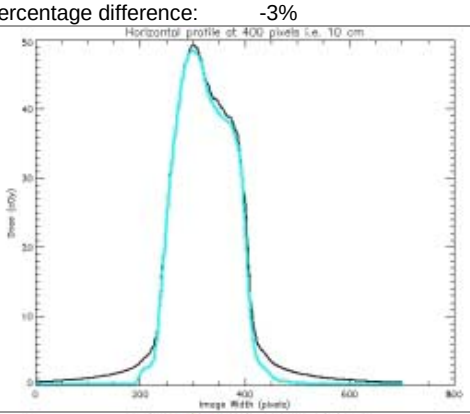
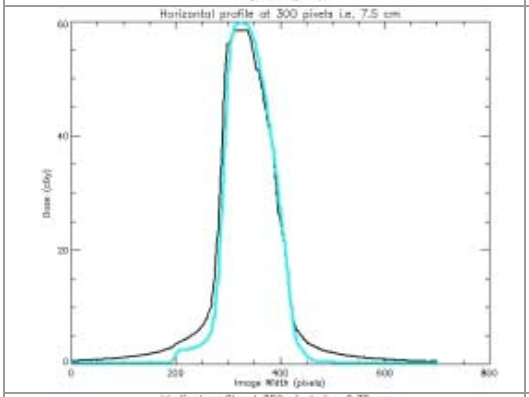	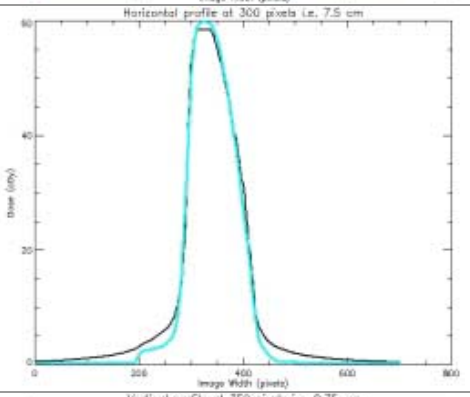
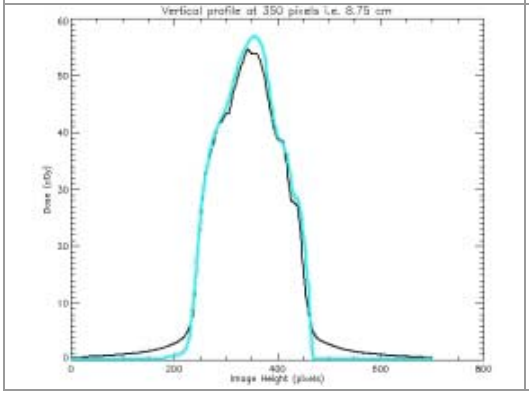	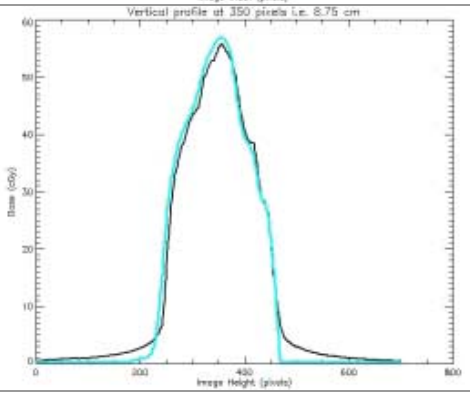

Figure 38. Reproducibility analysis - exposed on different days

Exposure 1	Exposure 2
Maximum value in Plan array is: 59.9180 The maximum value of Plan is at location (22, 2383) Maximum value in Plate array is: 58.3862 The maximum value of Plate is at location (8, 2180) Percentage difference: -3%	Maximum value in Plan array is: 59.9180 The maximum value of Plan is at location (22, 2383) Maximum value in Plate array is: 58.3862 The maximum value of Plate is at location (8, 2180) Percentage difference: -3%
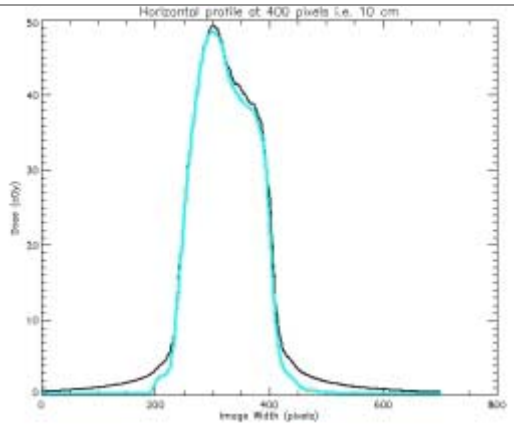	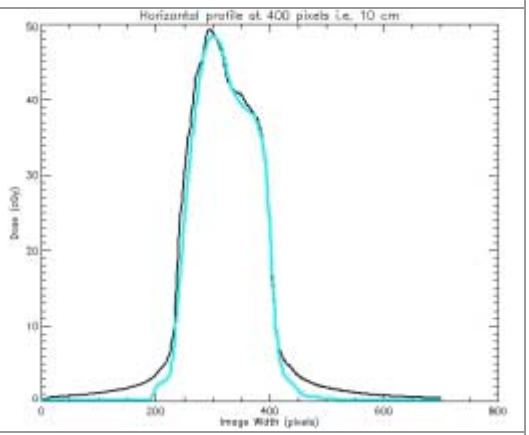
Exposure 3	Exposure 4
Maximum value in Plan array is: 59.9180 The maximum value of Plan is at location (22, 2383) Maximum value in Plate array is: 58.7386 The maximum value of Plate is at location (8, 2180) Percentage difference: -2%	Maximum value in Plan array is: 59.9180 The maximum value of Plan is at location (22, 2383) Maximum value in Plate array is: 58.3862 The maximum value of Plate is at location (8, 2229) Percentage difference: -3%
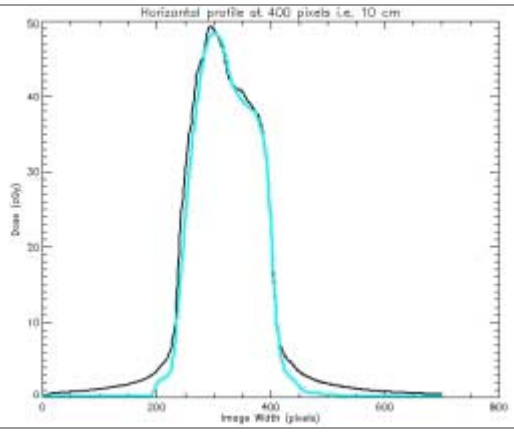	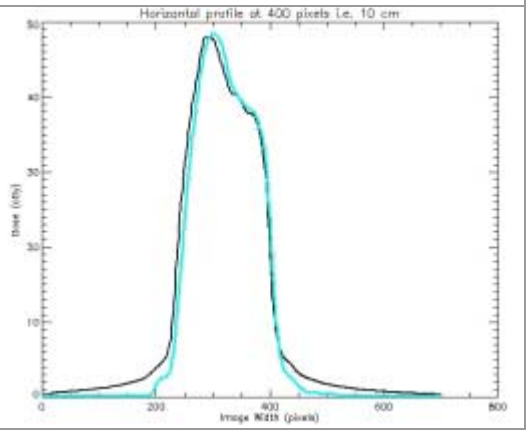

Figure 39. Reproducibility analysis – same day exposure

Plate to Film Results Comparison

For some fields, a comparison of plate vs. film results was done. Percentage differences in absolute dose values as well as some of the profiles were compared. For the plates the IMRT analysis algorithm developed in IDL was used; for the film IMRT analysis, the RIT113 v. 3.14 software was used. Typical results are presented for all three energies: 4 MV (Figure 40), 6 MV (Figure 41) and 10 MV (Figure 42).

4 MV

	% difference read for point (absolute dose)
Film	-7.1
Plate	-3

Profiles

Profile Location	Film	Plate
	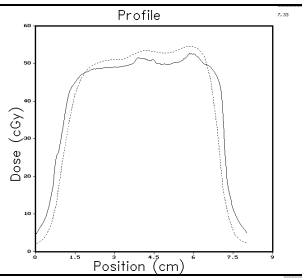	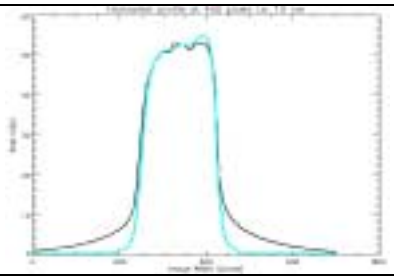
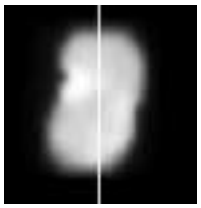	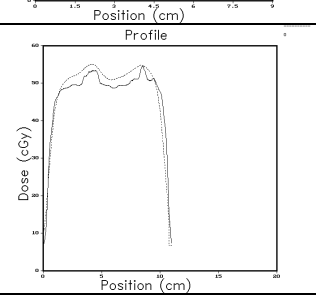	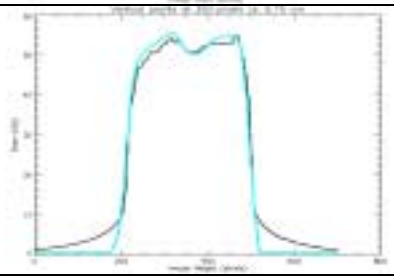
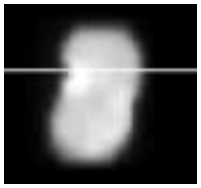	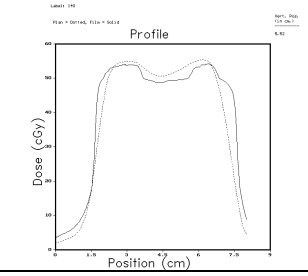	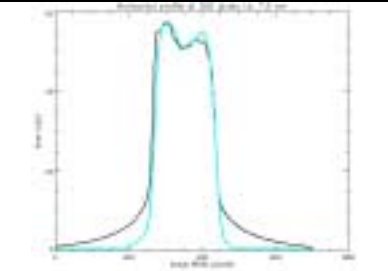

Figure 40. 4 MV, film, plan, plate comparison

6 MV

	% difference read for point (absolute dose)
Film	-1.4
Plate	-2

Profiles

Profile Location	Film	Plate
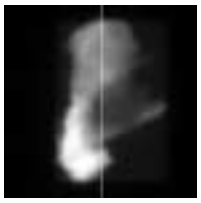	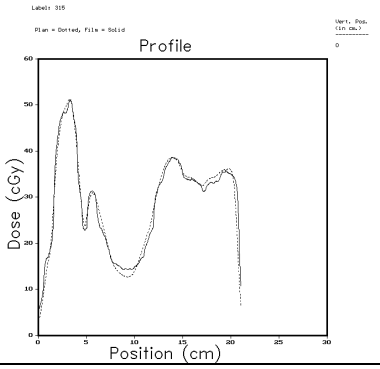	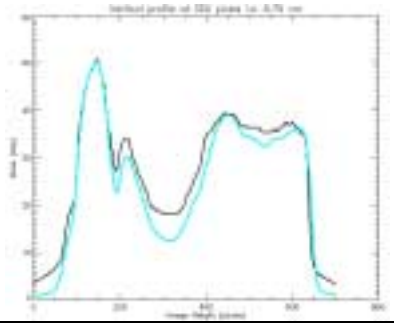
	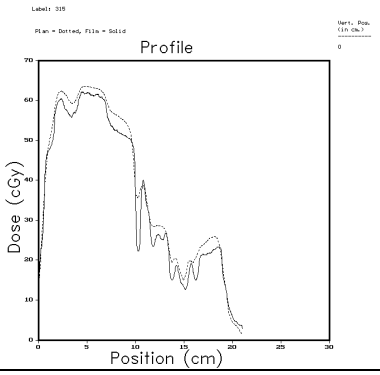	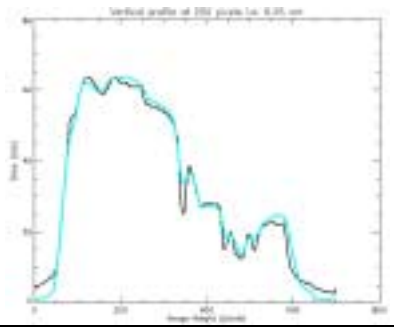
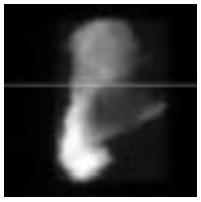	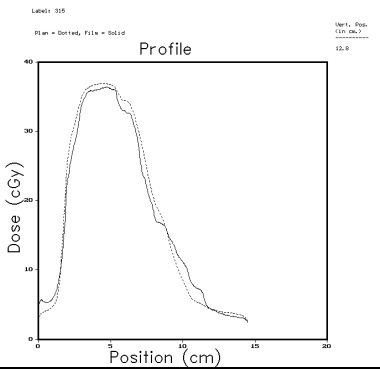	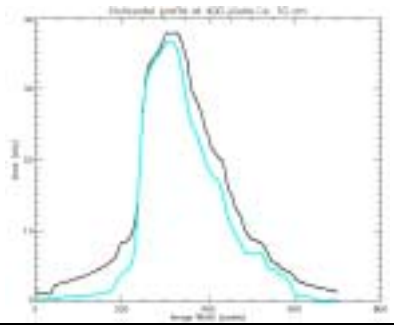

Figure 41. 6 MV, film, plan, plate comparison

10 MV

	% difference read for point (absolute dose)
Film	-0.4
Plate	-3

Profiles

Profile Location	Film	Plate
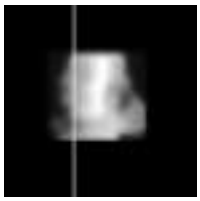	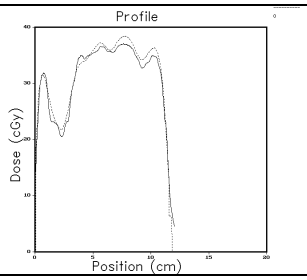	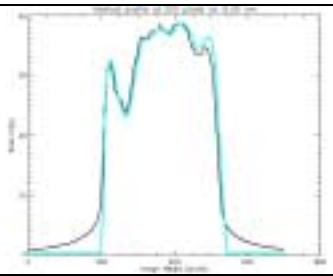
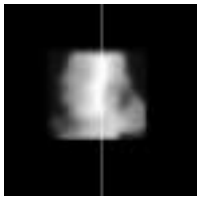	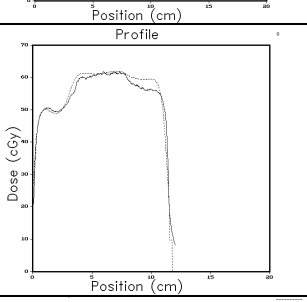	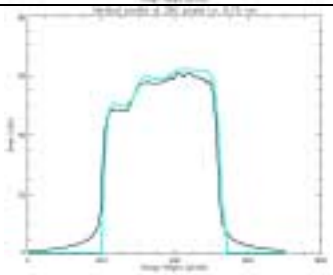
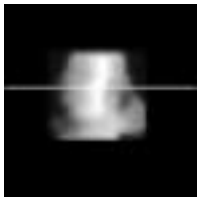	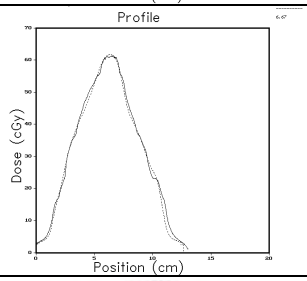	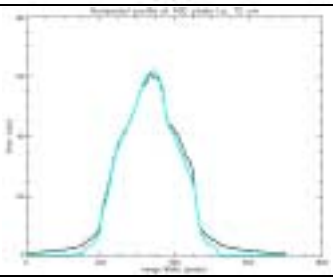
Normalized contours	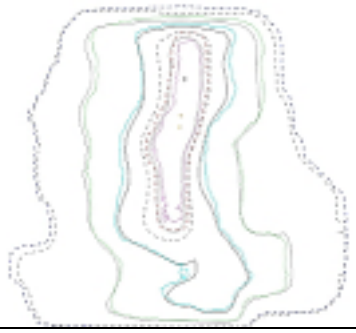	

Figure 42. 10 MV, film, plan, plate comparison

It should be noted that while both plan and film images are cropped to the same field size, the CR plate image is not, so its value on the field edges does not go artificially to zero. A closer look at the film and plan profiles (especially with 10 MV examples) shows that the film profile is cut off and that the trend of the profile does not necessarily drop to zero at the field edge. In the 10 MV cases, the plate profile follows the plan profile even in the low dose areas (Figure 42).

To have accurate and reliable comparison, the right calibration curve is the most important part. More work should obviously be done in calibration data collection, trying different depths in the phantom (maybe 10 cm which is usually used as the reference depth for calibration purposes for photon beams, where contribution of dose from incident electron contamination is minimal), using different lead sheet thickness, and finding correction factors that will compensate for CR plate and scanner non-uniformities (a Kodak scanner calibration procedure may be needed). Thus by obtaining the most reliable calibration curve decision, the best patient-specific IMRT QA can be made. Overall, it appears that CR plates are a reasonable IMRT QA tool, probably somewhat better than film.

Evaluation of the Automatic Image Registration Algorithm

The registration algorithm was evaluated for several different cases. This evaluation showed some of the algorithm constraints mentioned before:

- if image size is small, rotation is not done right;

- if images are not of the same type, scaling is not done right (evaluation was done using MRI and CT images of the brain);
- otherwise it works fine as one sees on the following figures.

Figure 43 and Figure 44 show the algorithm output for two examples.

Plan image:

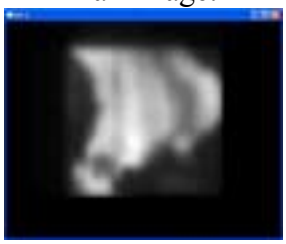

Plate image (before registration):

Plate image (after registration):

Profiles (y-axis values are in cGy):

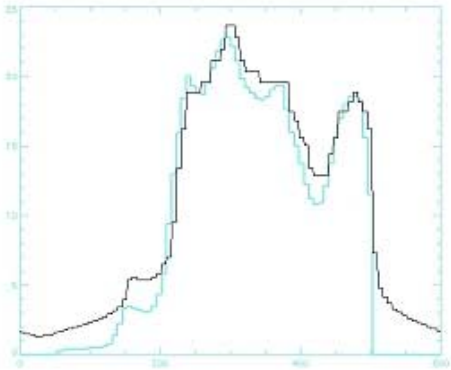

Horizontal

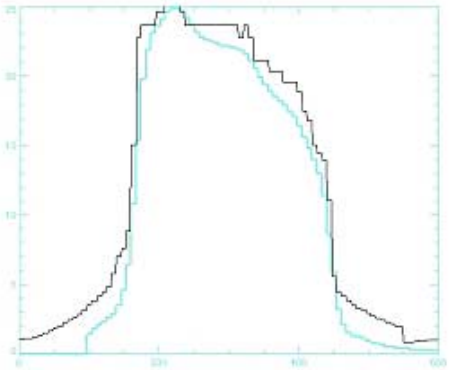

Vertical

Figure 43. Automatic image registration – case I

Plan image:

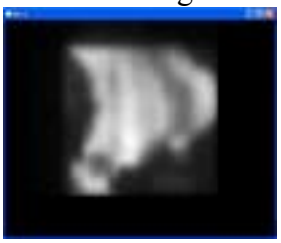

Plate image (before registration):

Plate image (after registration):

Profiles (at the same position as in previous case):

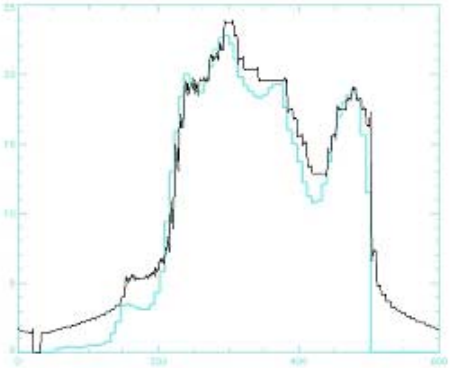

Horizontal

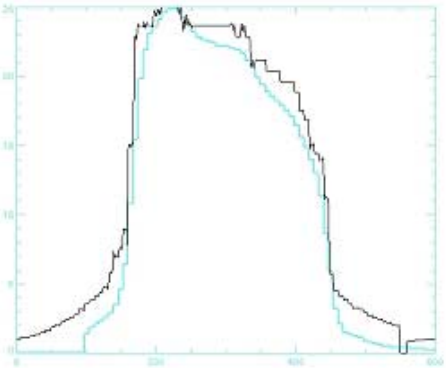

Vertical

Figure 44. Automatic image registration – case II

In the case I, plan and plate images were taken as is and the registration algorithm applied. In the case II, the plate image was purposely rotated before the evaluation. It is obvious that the algorithm correctly registers images in both cases and that profiles show no significant difference. In this evaluation, for faster results the images were not smoothed (with a mean filter) before profiles were taken as they

are in the program used for the IMRT analysis. For the plan and plate images, the registration always appeared to work correctly.

Summary and Conclusions

The purpose of this study was to investigate the possibility of using CR plates instead of film for patient-specific IMRT QA. Several different tests were performed to establish the overall behavior of the CR plates. Overall, 778 exposures were done (calibration and repeated exposures included), from which 609 exposures were done with 'new' plates and 169 exposures were done with 'old' plates.

Calibration curves were generated for three energies: 4, 6 and 10 MV. It was shown that one curve can be used for each energy independently of the day when the measurement is taken. Saturation of the CR plates and variations in results were noticed for all three energies when more than 100 MU delivered, as it can be seen from the calibration curve deliveries.

It is obvious that even though results were good when the calibration curve used for the analysis was taken as a best fit to the maximum number of data points measured, some results strongly depended on the range of the curve used (i.e. using an exponential equation based on fewer calibration points). Some of the discrepancies noticed can be avoided by using a separate calibration curve in the low dose region. Also, using a lead filter would certainly help.

The main goal of the research (finding out if CR plates can be used in IMRT QA) is done, but the tools used in the analysis need further development to be able to

utilize the procedure more efficiently. Finally, CR plate dosimetry has several major advantages over film dosimetry:

- The calibration curve at each energy is stable over time;
- CR plates are less time-consuming than film (using CR plates should be even less time consuming when the analysis process can be automated, the current manual analysis with IDL is faster than film analysis with RIT);
- Working with CR plates is no more difficult than working with film.

In high dose regions, the CR-measured values compare well to planned values. In low dose regions, fields delivered with the full number of MU show better agreement with the plan than fields delivered with half the MU (possibly due to calibration curve limitations at low doses as noted before). One major drawback to CR plates is the inexplicable apparent overexposure of some fields. The specific cause of this behavior could not be identified.

References

1. Faiz M. Khan, The Physics of Radiation Therapy. Lippincott Williams & Wilkins, 3rd edition, (2003).

2. Gary A. Ezzell, Quality Assurance: When and What is Enough for IMRT?. AAPM 2003 Summer School, Intensity-Modulated Radiation Therapy: The State of the Art, (2003).

3. Michael B. Sharpe, Commissioning and Quality Assurance for IMRT Treatment Planning. AAPM 2003 Summer School, Intensity-Modulated Radiation Therapy: The State of the Art, (2003).

4. J. H. Kung, G. T. Y. Chen, F. K. Kuchnir, A monitor unit verification calculation in intensity modulated radiotherapy as a dosimetry quality assurance. Med. Phys. Vol. 27, No 10: 2226-2230, October 2000.

5. ADAC Pinnacle^3, SmartSim User Guide. Version 6.0, August 2001.

6. M. Hareyama, N. Tsuchiya, M. Takebe and T. Chida, Two-dimensional measurement of natural radioactivity of granitic rocks by photostimulated luminescence technique. Geochemical Journal, Vol. 34, 1 - 9, (2000).

7. Heinz Anderle, Physical Methods: Theory. Available online: http://www.anc.univie.ac.at/scripts/anderle_cap4.pdf., 1997. [Downloaded: June 15, 2004]

8. J. A. Seibert, Physics of Computed Radiography. AAPM 1999 Annual Meeting, Nashville, (1999).

9. Kodak 2000RT CR System, Characteristics of a computed radiography system for radiation therapy. Eastman Kodak Company, (2002).

10. Kodak Health Imaging Products by Type, ACR-2000i System. Available online: http://www.kodak.com/global/en/health/productsByType/cr/acr2000i.jhtml. [Downloaded: April 10, 2004].

11. Cardinal Health's Radiation Management Services, Available online: http://www.cardinal.com/rms. [Downloaded: July 3, 2004].

12. Kodak Health Imaging Service and Support, Available online: http://www.kodak.com/global/en/health/serviceAndSupport/dicom.jhtml. [Downloaded: June 25, 2004].

13. DICOM Brahma ActiveX Control, Available online: http://freehost04.websamba.com/dicom4india/dicom_brahma.htm. [Downloaded: April 10, 2004].

14. DICOM plug in, DicomObserver, Available online: http://freehost04.websamba.com/dicom4indiadicom_component.htm. [Downloaded: April 10, 2004].

15. IrfanView, Graphic viewer, Available online: http://www.irfanview.com. [Downloaded: May 11, 2004].

16. RIT113 Film Dosimetry System Version 3.14, User's Manual & Guide. Radiological Imaging Technology, (2002).

17. Image Registration, Image Registration Mapping of Evolution. Available online: http://www.cs.ucsd.edu/classes/fa02/cse252c/Image_Registration.ppt. [Downloaded: May 13, 2004].

18. Enrique Corias, Javier Santamaria, Carlos Miravet, A Segment-based Registration Technique for Visual-IR Images. Available online: http://www.ece.eps.hw.ac.uk/~ecoiras/OptEng_Registration.pdf. [Downloaded: May 15, 2004].

19. UNESCO Training Course, The Frequency Domain. Available online: http://www.netnam.vn/unescocourse/computervision/chap9.doc. [Downloaded: May 15, 2004].

20. Connexions – Sharing Knowledge and Building Communities, Constraint Optimization. Available online: http://cnx.rice.edu/content/m11223/latest/. [Downloaded: May 20, 2004].

21. B. S. Reddy, B. N. Chatterji, An FFT based technique for translation, rotation, and scale-invariant image registration. IEEE Transactions on Image Processing, Vol. 5, 1266-1271, (1996).

22. Hongjie Xie, Nigel Hicks, G. Randy Keller, Haitao Huang, Vladik Kreinovich, An IDL/ENVI implementation of the FFT-based algorithm for automatic image registration. Computers and Geosciences 29, 1045-1055, (2003).

23. RSI (Research Systems, Inc.) - Data Analyses and Visualization Software, Removing Noise from an Image with FFT. Available online: http://www.rsinc.com. [Downloaded: May 20, 2004].

24. John P. Gibbons, Monitor Unit Calculations for External Photon and Electron Beams. Advanced Medical Publishing, Inc., (2000).

Appendix A. Varian LINAC 21EX (6-18) Components

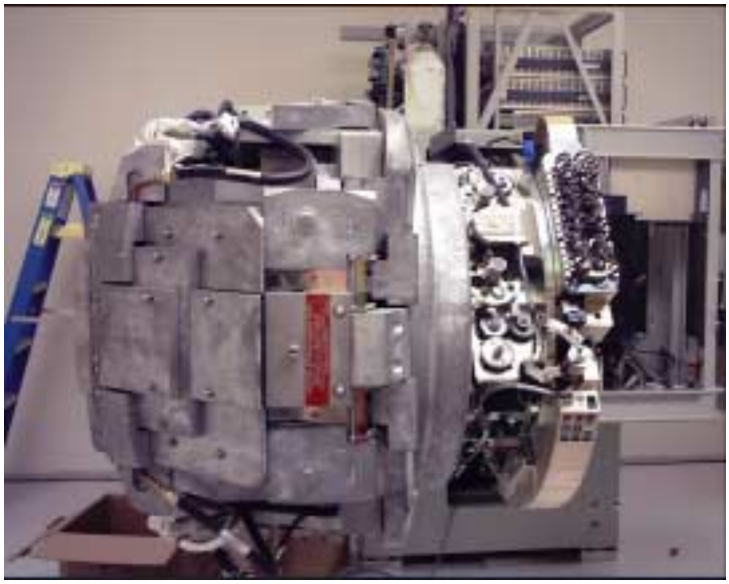

Treatment Head
(shielding blocks, and electro motors used for the MLC control are visible)

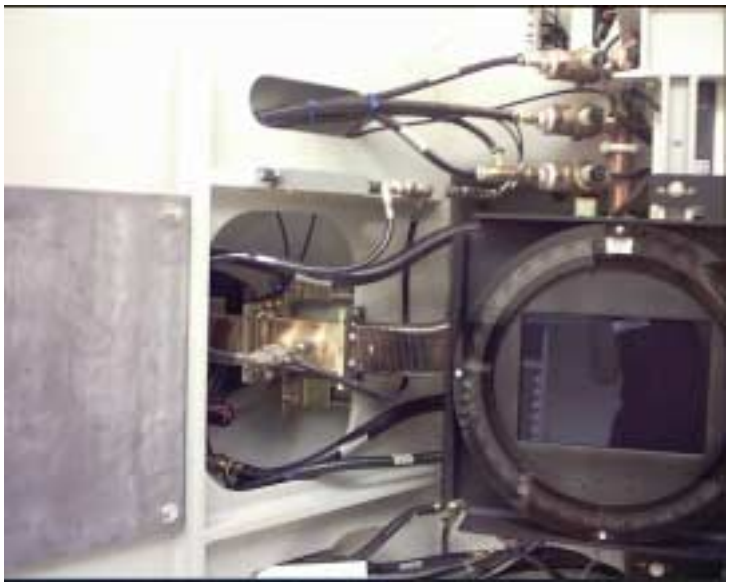

RF power coming from Klystron (Wave Guide System)

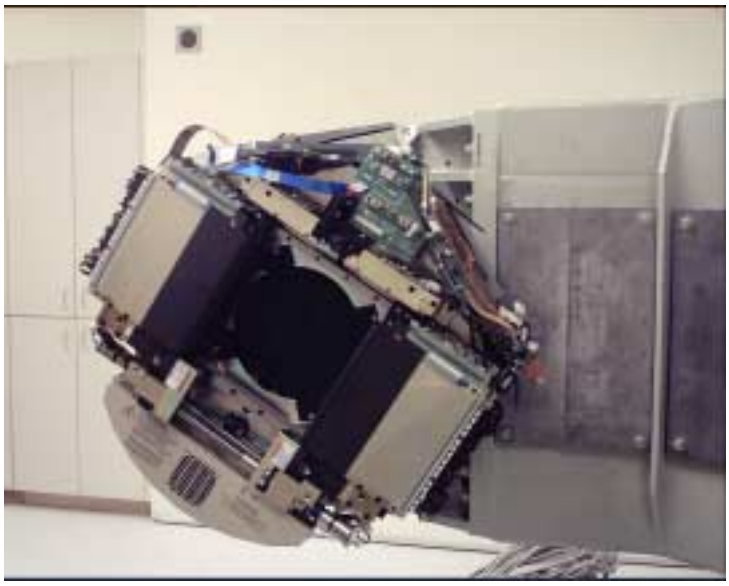

View of the Collimators (Jaws) and MLCs in the Treatment Head

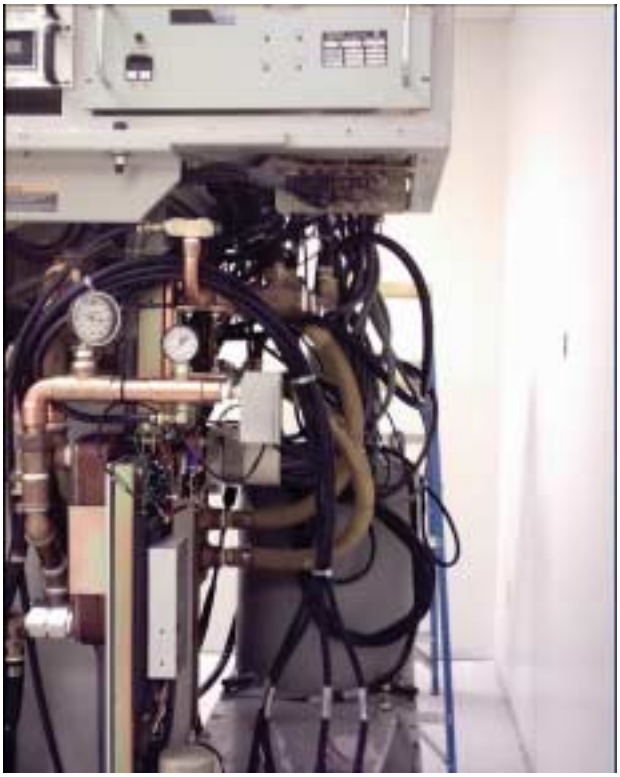

LINAC's ancillary equipment
(Klystron is visible behind the cables)

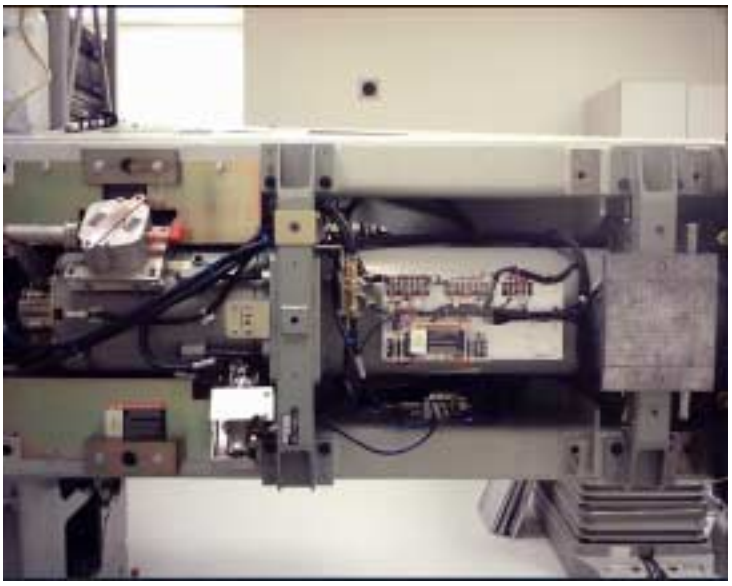

Accelerator Tube

Accelerator Tube (different view)

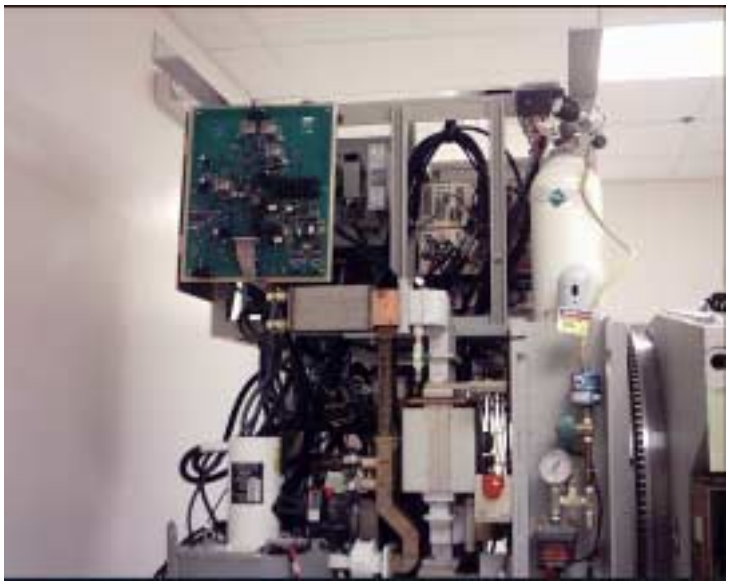

Ancillary Equipment

Gantry

Appendix B. DICOM to TIFF Application

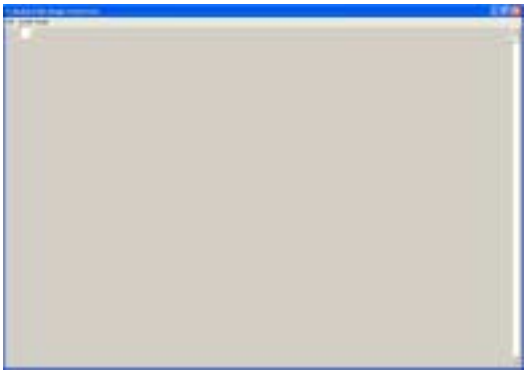

Opened Application

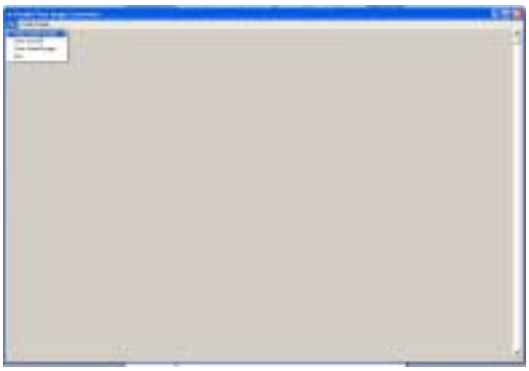

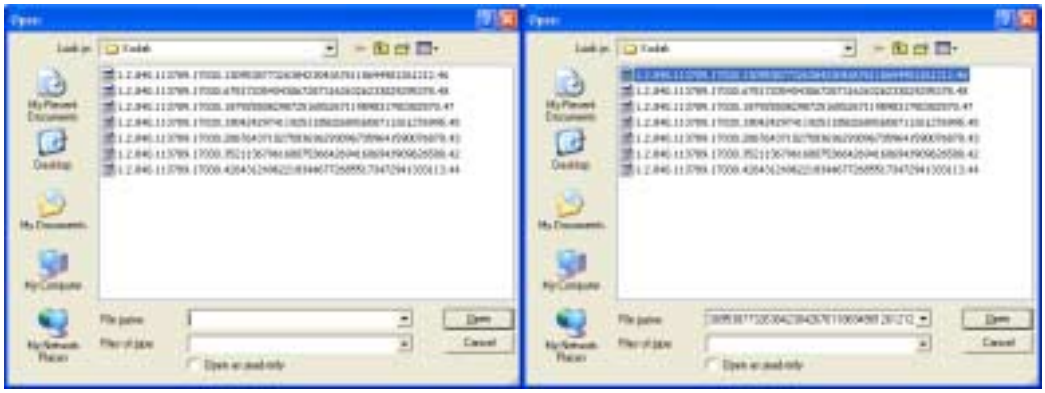

Opening Kodak Image File

Opened Kodak Image File

Getting the Header Information of the Image

Inverting the Image

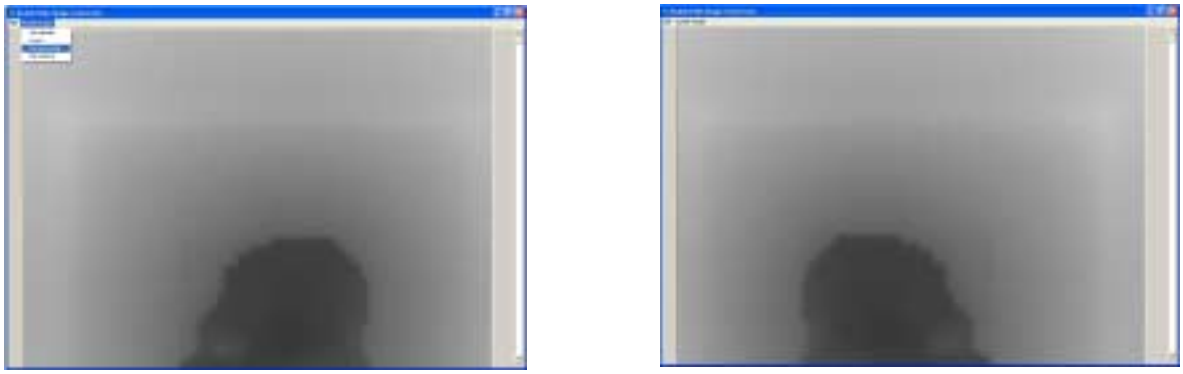

Flipping the Image Horizontally

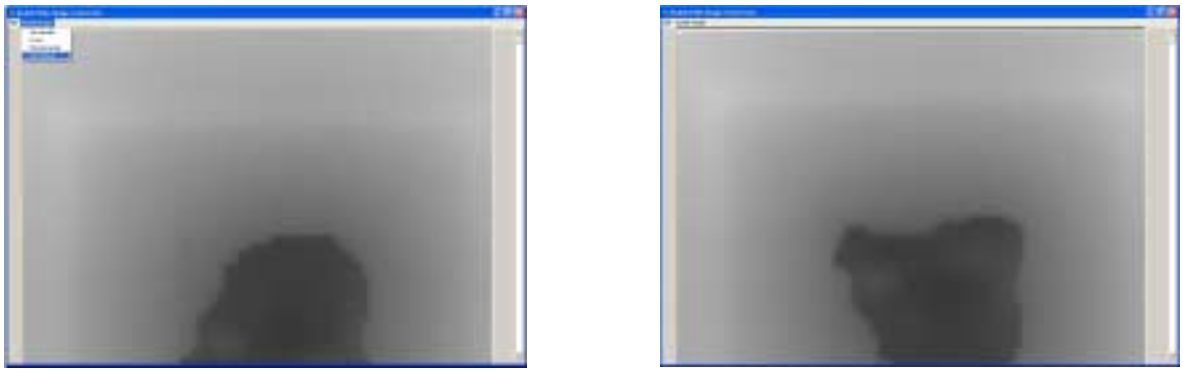

Flipping the Image Vertically

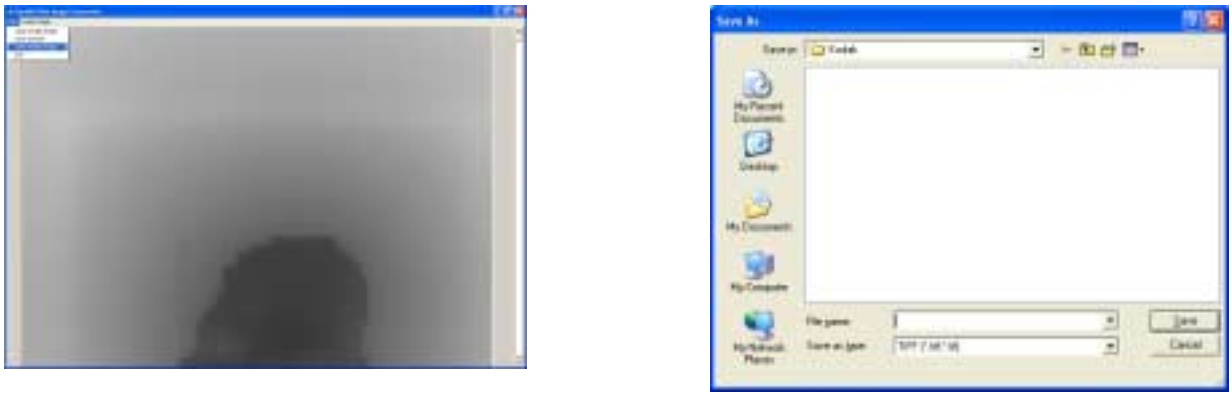

Saving the Image in TIFF Format

Appendix C. MU Calculations

Monitor Unit Calculation for Photon Beam

Dosimetric quantities used in the calculation are[24]:

- TMR (Tissue-Maximum Ratio)
    - special case of TPR (tissue-phantom ratio)
    - ratio of dose at a given point in phantom (point P) to the dose at the same point in the beam (point Q) at a fixed reference depth of maximum dose, d_m, Figure 45

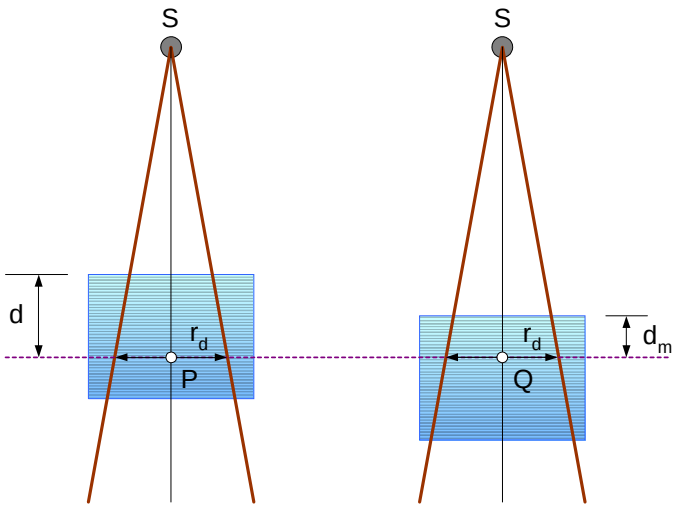

Figure 45. Definition of TMR

- TMR can be derived directly from the percent depth dose (PDD) data

$$TMR(d, r_d) = \left(\frac{PDD(d, r, SSD)}{100}\right)\left(\frac{SSD + d}{SSD + d_m}\right)^2\left(\frac{S_p(r)}{S_p(r_d)}\right)$$

where r is field size at surface, r_d is field size at depth d, SSD is source-surface distance and S_p is the phantom scatter factor measured at reference depth d_m

- S_c (Collimator Scatter Factor)
  - ratio of photon energy fluence in air at a point in a given field to the energy fluence for a 10 x 10 cm^2 field centered at that point

- S_p (Phantom Scatter Factor)
  - ratio of dose in a phantom for a given field at d_m to the dose at the same point for a 10 x 10 cm^2 field size, with the same incident fluence

  - commonly determined by

$$S_p(r) = \frac{S_{c,p}(r)}{S_c(r)}$$

where $S_{c,p}(r)$ is the total scatter factor defined as the dose in phantom at d_m for a given field of size r divided by the dose at the same point for the reference 10 x 10 cm^2 field

- OAR (Off-Axis ratio)
  - ratio of primary dose at the off-axis point to the primary dose at the central axis point

- TF (Tray Factor)
    - tray transmission factor is usually determined in a phantom at a fixed depth

- WF (Wedge Factor)
    - wedge transmission factor may be measured in a phantom at a suitable depth for a number of field sizes

MU calculation equation:

$$MU = \frac{D}{K \cdot TMR\left(d,(r_d)_{eff}\right) \cdot S_c(r_c) \cdot S_p\left((r_d)_{eff}\right) \cdot TF \cdot WF \cdot OAR(d_{.}) \cdot \left(\frac{SCD}{SPD}\right)^2}$$

where D is dose in cGy to be delivered at depth d, K is 1 cGy/MU, $(r_d)_{eff}$ is effective field size at depth d, r_c is collimator field size projected at isocenter, SCD is source-calibration point distance (can be = SAD (source-axis distance = 100) or = 100 + d_m), SPD is source-point of calculation distance.

Appendix D. Interpolation in Image Processing

Interpolation in Image Processing

Interpolation is the process used to estimate an image value at a location in between image pixels. For example, if image is resized so it contains more pixels than it did originally, interpolation is used to determine the values for the additional pixels.

Three interpolation methods most commonly used in image processing are:

- Nearest-neighbor interpolation
- Bilinear interpolation
- Bicubic interpolation

They all work in fundamentally similar way.

Nearest neighbor interpolation offers fast method of resampling but it only takes info from pixels at each side of the new one so the calculation is less precise. The output pixel is assigned value the point falls within, no other pixels are considered.

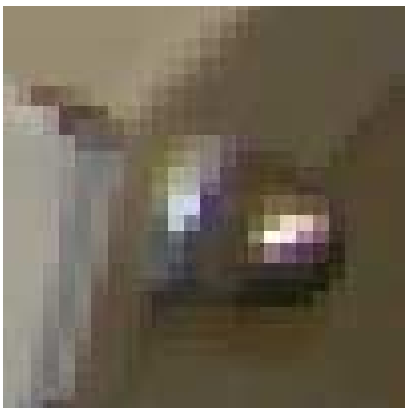

Bilinear interpolation takes info from the pixels above and to the side of where the new pixel will appear and offers slightly better quality when compared to nearest neighbor interpolation. The output pixel is a weighted average of pixels in the nearest 2 by 2 neighborhood.

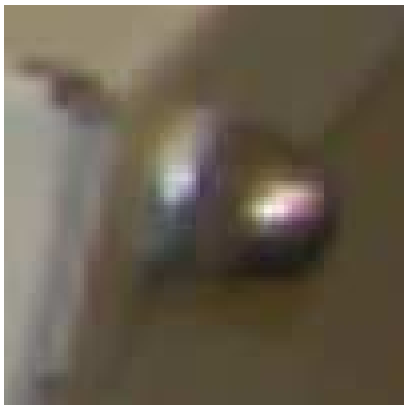

Bicubic interpolation samples from all eight surrounding pixels resulting in smoothest tonal gradations. The output pixel is a weighted average of pixels in the nearest 4 by 4 neighborhood.

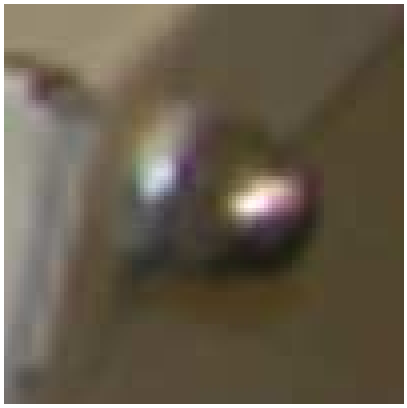

Appendix E. Fourier Transform

Fourier Transform

In 1807, Jean Baptiste Joseph Fourier presented the results of his study of heat propagation and diffusion to the 'Institut de France'. In his presentation, he claimed that any periodic signal could be represented by a series of sinusoids. These sinusoids vary in frequency and amplitude. Though this concept was initially met with resistance, it has since been used in numerous developments in mathematics, science, and engineering. This concept is the basis for what we know today as the Fourier series.[19]

The spatial frequency of an image refers to the rate at which the pixel intensities change. The frequency domain shows the magnitude of different frequency components. Many different transforms are used in image processing (Hilbert, Hartley, Hough, Radon, …). Due to its wide range of applications in image processing, the Fourier transform is one of the most popular (Figure 46). It operates on a continuous function of infinite length.

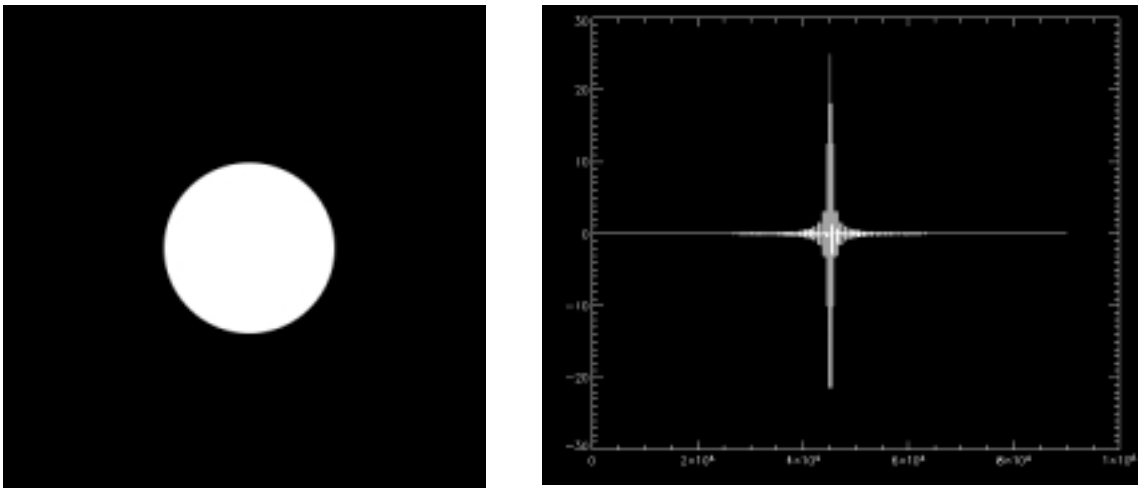

Original Image Fourier Transform - Surface Plot

Figure 46. Fourier transform of a uniform disk

The Fourier transform of a 2-dimensional function is shown mathematically as

Eq. 12. $$H(u,v) = \iint h(x,y) e^{-i2\pi(ux+vy)} dxdy$$

where

$i = \sqrt{-1}$ and $e^{\pm ix} = \cos(x) \pm i\sin(x)$

Inverse Fourier Transform, Eq. 13, is used to transform image data from the frequency domain back to the spatial domain.

Eq. 13. $$h(x,y) = \iint H(u,v) e^{i2\pi(ux+vy)} dudv$$

In the frequency domain, u represents the spatial frequency along the original image's x axis and v represents the spatial frequency along the y axis. In the center of the image u and v have their origin.

The Fourier transform deals with complex numbers. Another way to represent the data is with its phase and magnitude. Magnitude (Figure 47), is expressed as:

Eq. 14. $$|H(u,v)| = \sqrt{R^2(u,v) + I^2(u,v)}$$

and phase as:

Eq. 15. $$\phi(u,v) = \tan^{-1}\left(\frac{I(u,v)}{R(u,v)}\right)$$

where $R(u,v)$ is the real part and $I(u,v)$ is the imaginary part. The magnitude is the amplitude of sine and cosine waves in the Fourier transform formula. As expected, ϕ is the

phase of the sine and cosine waves. This information along with the frequency, allows full specification of the sine and cosine components of an image. Frequency is dependent on the pixel location in the transform. The further from the origin it is, the higher the spatial frequency it represents.

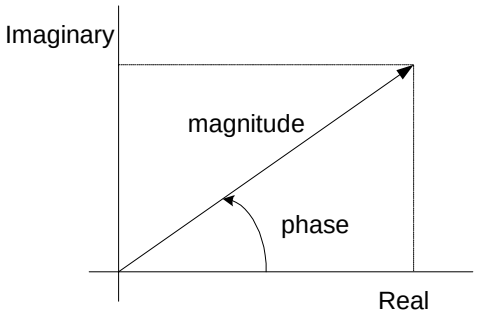

Figure 47. Relationship between phase and magnitude

When working with digital images, a continuous function is not used but rather a finite number of discrete samples. These samples are the pixels that compose an image. To do image analysis on the computer, a discrete Fourier transform needs to be used. The discrete Fourier transform represents a special case of the continuous Fourier transform. The formula to compute the discrete Fourier transform on an M x N size image is

Eq. 16. $$H(u,v) = \frac{1}{MN} \sum_{x=0}^{M-1} \sum_{y=0}^{N-1} h(x,y) e^{-i2\pi(ux/M + vy/N)}$$

The discrete Fourier transform expects the input data to be periodic, and the first sample is expected to follow the last sample. The discontinuity (ringing known as Gibb's phenomenon) observed if this rule is not followed is a function of the difference between the amplitude of the first and last samples. To reduce this discontinuity, data can be multiplied by a windowing function (sometimes called window weighting functions) before the Fourier

transform is performed. There are a number of window functions, each with its set of advantages and disadvantages. Window functions attenuate the original image data.

The discrete Fourier transform is computationally intensive. An image of size $M \times M$ will require $(M^2)^2$ or M^4 complex multiplications. Fortunately, in 1942, it was discovered that the discrete Fourier transform of length N could be rewritten as the sum of two Fourier transforms of length $N/2$. This technique is known as the Fast Fourier Transform. It reduces the number of complex multiplications from N^2 to the order of $N\log_2 N$. This savings is substantial especially when image processing is done. The FFT is separable, which makes Fourier transforms even easier to do. Because of the separability, the FFT operation can be reduced from a 2-dimensional operation to two 1-dimensional operations. First the FFT of the rows of an image is computed and then the FFT of the columns. For an image of size $M \times N$, this requires $N + M$ FFTs to be computed. The order of $NM\log_2 NM$ computations are required to transform the image.

There are some considerations to keep in mind when transforming data to the frequency domain via the FFT. First, since the FFT algorithm recursively divides the data down, the dimensions of the image must be powers of 2 ($N = 2^j$ and $M = 2^k$ where j and k can be any number). Chances are pretty good that image dimensions are not a power of 2. The image data set can be expanded to the next power of 2 by surrounding the image with zeros; this is called zero-padding. The image could also be scaled up to the next legal size or cut down at the next valid size.[19] For algorithm developed during this study build in FFT function is used for all the FFT transforms.

Appendix F. Determination of the Translation, Rotation and Scaling Values

Determination of the translation value

(*Note:* in accordance with the terminology used previously, $I(\vec{x}) = I(x, y)$ and $F(\vec{\omega}) = H(u, v)$)

It is known that if two images, $I1(\vec{x})$ and $I2(\vec{x})$, differ only by shift (translation), i.e. if $I2(\vec{x}) = I1(\vec{x} + \vec{a})$, where $\vec{a}$ is some unknown shift, then their Fourier transforms are:

$$F1(\vec{\omega}) = \frac{1}{2\pi}\iint I1(\vec{x}) e^{-2\pi i(\vec{x}\vec{\omega})} dxdy$$

$$F2(\vec{\omega}) = \frac{1}{2\pi}\iint I2(\vec{x}) e^{-2\pi i(\vec{x}\vec{\omega})} dxdy$$

Their Fourier transforms are then related by the following equations:

Eq. 17 $$F2(\vec{\omega}) = e^{-2\pi i(\vec{\omega}\vec{a})} F1(\vec{\omega})$$

and

Eq. 18 $$\left|F2(\vec{\omega})\right| = \left|F1(\vec{\omega})\right|$$

To obtain shift $\vec{a}$ Eq. 17 is used to compute the value of the following ratio:

Eq. 19 $$R(\vec{\omega}) = \frac{F2(\vec{\omega})}{F1(\vec{\omega})} = e^{-2\pi i(\vec{\omega}\vec{a})}$$

Inverse Fourier transform of this ratio is equal to the delta function $\delta(\vec{x} - \vec{a})$. This inverse Fourier transform is equal to zero everywhere except for the point $\vec{x} = \vec{a}$. So the desired shift $\vec{a}$ can be determined from the fact that it represents only value for which inverse Fourier transform of the ratio is not equal to zero.

In the ideal case the absolute value of the ratio is equal to 1. In real life images have some noise in them. In the presence of noise observed values of the intensities may differ from the actual values, and as a result the absolute value of the ratio $R(\vec{\omega})$ may be different from 1. To find out exact value of the ratio in the presence of noise following can be done. Let

$e^{-2\pi i(\vec{\omega}\vec{a})} = b$

then in absence of noise:

Eq. 20 $F2(\vec{\omega}) = bF1(\vec{\omega})$

In the presence of noise Fourier transforms, $F1(\vec{\omega})$ and $F2(\vec{\omega})$, can be different from the actual values so the Eq. 20 changes to

Eq. 21 $F2(\vec{\omega}) \approx bF1(\vec{\omega})$

As stated before it is also known that absolute value of b is equal to 1:

Eq. 22 $|b| = 1$ i.e. $|b|^2 = b \cdot b^* = 1$

where b^* is complex conjugate to b.

Now the best estimate for b that satisfies condition in Eq. 22 and approximate Eq. 21 has to be found. For this task the Least Squares Method can be used. This method assumes that the best-fit curve of a given type is the curve that has the minimal sum of the deviations squared (least square error) from a given set of data. According to this method for each estimation of b error (E) can be defined as follows:

Eq. 23 $E = F2(\vec{\omega}) - bF1(\vec{\omega})$

Then among all estimates that satisfy the additional condition in Eq. 22, a value of b for which the square of error, $|E|^2 = E \cdot E^*$, is minimum is found. Knowing

Eq. 24

$$|E|^2 = E \cdot E^* = [F2(\bar{\omega}) - bF1(\bar{\omega})] \cdot [F2^*(\bar{\omega}) - b^* F1^*(\bar{\omega})]$$
$$= F2(\bar{\omega})F2^*(\bar{\omega}) - b^* F2(\bar{\omega})F1^*(\bar{\omega}) - bF1(\bar{\omega})F2^*(\bar{\omega}) + bF1(\bar{\omega})b^* F1^*(\bar{\omega})$$

Resulting expression has to be minimized under the constraint in Eq. 22.[9] Constraint optimization is the minimization of an objective function subject to constraints on the possible values of the independent variable. The typical constrained optimization problem has the following form:

$\min_x \{f(x)\}$ subject to $g(x) = 0$

where $f(x)$ is the scalar-valued objective function and $g(x)$ is the vector-valued constraint function.

The classical approach to solving constraint optimization problems is the method of Lagrange Multipliers. This approach converts the constrained optimization problem into an unconstrained one. The Lagrangian of a constraint optimization problem is defined to be the scalar-valued function

$L(x, \lambda) = f(x) + \lambda^T g(x)$

where λ is Lagrange multiplier.

Stationary points of the Lagrangian are potential solutions of the constrained optimization problem, as always each candidate solution must be tested to determine which one minimizes the objective function. As shown in Figure 48, the constraint corresponds to a contour in the x plane.

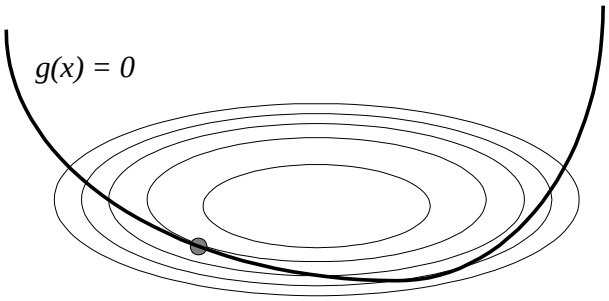

Figure 48. Geometric interpretation of Lagrange multipliers

In the above figure thick line corresponds to the contour of the values of x satisfying constraint equation $g(x)=0$. The thinner lines are contours of constant values of the objective function $f(x)$. The contour corresponding to the smallest value of the objective function just tangent to the constraint contour is the solution to the optimization problem with equality constraints.[20]

In the other words minimum of the function $f(x)$ under the constraint $g(x)=0$ is attained when for some real number λ function $L(x,\lambda)$ attains its unconstraint minimum.

This leads to finding the value of the complex variable b for which the expression

Eq. 25

$$F2(\bar{\omega})F2^{*}(\bar{\omega})-b^{*}F2(\bar{\omega})F1^{*}(\bar{\omega})-bF1(\bar{\omega})F2^{*}(\bar{\omega})+bF1(\bar{\omega})b^{*}F1^{*}(\bar{\omega})+\lambda(b\cdot b^{*}-1)$$

takes the smallest possible value.

Since complex variable is in effect a pair of two real variables minimum can be found as a point at which the partial derivatives with respect of each of these variables are both equal to zero. If Eq. 25 is differentiated relative to b^{*} following linear equation is obtained:

Eq. 26 $$-F2(\bar{\omega})F1^{*}(\bar{\omega})+bF1(\bar{\omega})F1^{*}(\bar{\omega})+\lambda b=0$$

From this equation b can be found as

Eq. 27 $$b = \frac{F2(\vec{\omega})F1^{*}(\vec{\omega})}{F1(\vec{\omega})F1^{*}(\vec{\omega}) + \lambda}$$

From the condition in Eq. 22 that value b should satisfy the coefficient λ can be determined. Knowing that denominator in Eq. 27 is a real number, it is sufficient to find a value of this denominator for which $|b|^2 = b \cdot b^{*} = 1$. To achieve this the absolute value of the numerator should be taken as denominator, i.e.

Eq. 28 $$\left|F2(\vec{\omega})F1^{*}(\vec{\omega})\right| = \left|F2(\vec{\omega})\right| \cdot \left|F1^{*}(\vec{\omega})\right|$$

and now expression for b, Eq. 27, has a following form

Eq. 29 $$b = \frac{F2(\vec{\omega})F1^{*}(\vec{\omega})}{\left|F2(\vec{\omega})\right| \cdot \left|F1^{*}(\vec{\omega})\right|}$$

The ratio $R(\vec{\omega})$ $\left(R(\vec{\omega}) = \frac{F2(\vec{\omega})}{F1(\vec{\omega})}\right)$ from the ideal non-noise case becomes

Eq. 30 $$R(\vec{\omega}) = \frac{F2(\vec{\omega})F1^{*}(\vec{\omega})}{\left|F2(\vec{\omega})\right| \cdot \left|F1^{*}(\vec{\omega})\right|}$$

in the presence of noise.

From the equation above it is obvious that inverse Fourier transform of $R(\vec{\omega})$ in the presence of noise has values that are slightly different from the delta function, but still absolute value of the inverse Fourier transform should be much larger at point $\vec{x} = \vec{a}$ than all

the other values of this function. In this case desired shift $\bar{a}$ represents the point for which the absolute value of the inverse Fourier transform takes the largest possible value.

Using Log-Polar Coordinates for the Determination of Rotation and Scaling Values

If one image differs from another not only by shift, but also by the rotation and scaling then the absolute values (magnitudes) of their Fourier transforms are not equal, but also differ by the corresponding rotation and scale.

By using transformation to go from Cartesian to polar coordinates (r,θ) in the $\bar{\omega}$ plane, rotation by an angle θ_0 is described by simple shift $\theta \to \theta - \theta_0$. In the polar coordinates scaling is also simple but cannot be described by simple shift $r \to \lambda r$. On the other hand if transformation is made form Cartesian to log-polar coordinates (ξ,η) where $\xi = \log(r)$ and $\eta = \theta$, then scaling can be also represented by the shift $\xi \to \xi - c$, where $c = \log(\lambda)$. From this is obvious that log-polar transformation can be used to describe both rotation and scaling as a shift.

Log-Polar Transformation of an Image

The log-polar transformation is a conformal mapping from the points on the Cartesian plane (x, y) to points in the log-polar plane (ξ,η):

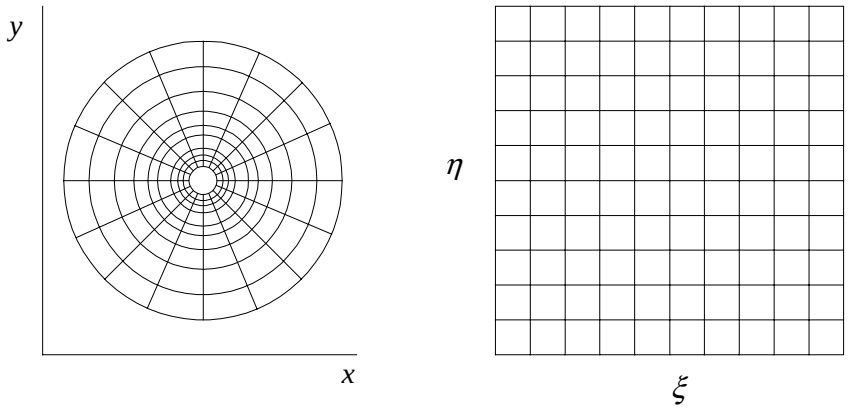

Cartesian Plane Log-Polar Plane

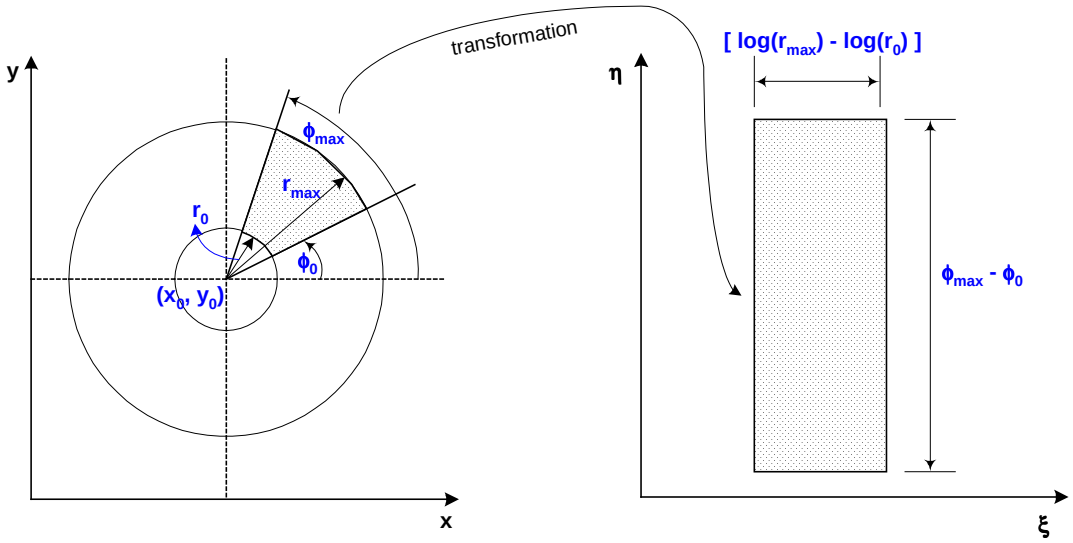

Log-Polar Transformation of the Circular Segment

Figure 49. Cartesian and log-polar planes

If $I(x, y)$ is an image with support on a rectangular set in the Euclidean plane, then the log-polar transform with origin (x_0, y_0) is described by following mapping[19]:

Eq. 31

$$\begin{cases} \xi = M \log(r + \alpha) \\ r = \sqrt{(x - x_0)^2 + (y - y_0)^2} \\ \eta = \tan^{-1}\left(\dfrac{y - y_0}{x - x_0}\right) \end{cases}$$

The transform maps a 2D image onto the surface of a cylinder. The cylinder is indexed by ξ and η. The ξ-axis is parallel to the axis of the cylinder. The η-axis forms a circle around the cylinder.

As shown above log-polar image is produced through a projection onto an image plane, which is not sampled in a rectangular (x, y)-grid, but in the following way: the pixels are arranged in concentric circular rings around the focus of attention. On each ring the same number of pixels is sampled, and the pixel size increases exponentially with growing radius of the rings in such a way, that all pixels are approximately square (see Figure 50).

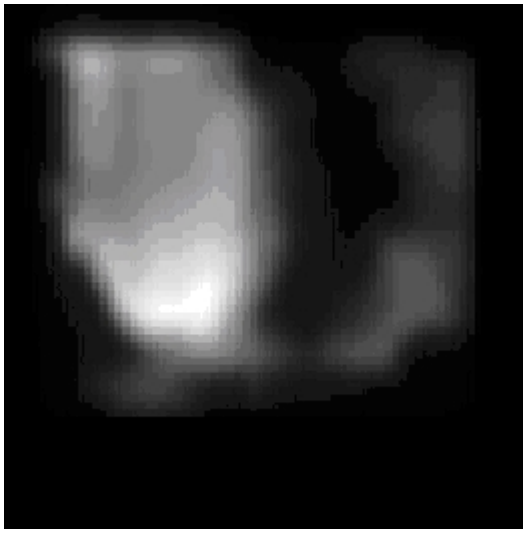

Original Image

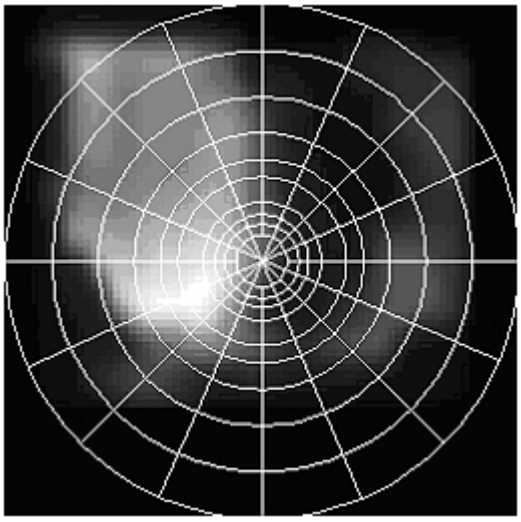

The Original Image Overlayed with Log-Polar Grid

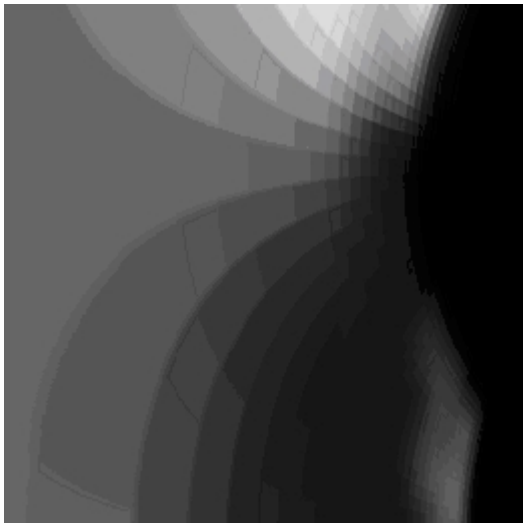

Generated Log-Polar Image

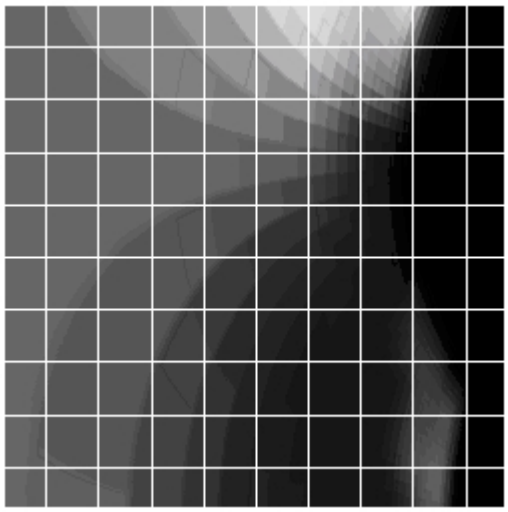

Log-Polar Image with the Rectilinear Grid Overlay

Figure 50. Log-polar imaging

After log-polar image is mapped back to Cartesian coordinates the decrease in resolution with increasing radius can be observed.

Determining Rotation and Scaling

Log-polar transformation can be used to describe both rotation and scaling as a shift. To determine rotation and scaling needed for the image registration both images have to be transformed from the original Cartesian coordinates to log-polar coordinates. Next same Fourier transforms as described for the translation determination are used to determine the corresponding shift $(\theta_0, \log(\lambda))$, from these values rotation angle θ_0 and scaling factor λ are reconstructed.

However, computing (ξ, η) from the original rectangular grid leads to points that are not located exactly at points in the original grid. Thus, interpolation is needed to find a value of $abs(F(\bar{\omega}))$ on the desired grid. A bilinear interpolation is used for resampling. Knowing the transformation relationship between the log-polar plane and Cartesian plane, point (x, y) in Cartesian plane is related to the desired grid point (ξ, η) by

Eq. 32
$$x = r\cos(\eta) = 10^{\xi}\cos(\eta)$$
$$y = r\sin(\eta) = 10^{\xi}\sin(\eta)$$

To find value of $A(\bar{\omega}) = abs(F(\bar{\omega}))$ i.e. $A(x, y)$ using bilinear interpolation, intensities $A_{i,j}$, $A_{i+1,j}$, $A_{i,j+1}$, and $A_{i+1,j+1}$ of four original grid points (i, j), $(i+1, j)$, $(i, j+1)$ and $(i+1, j+1)$ that surround point (x, y) are used:

Eq. 33
$$A(x, y) = (1-u)(1-v)A_{i,j} + u(1-v)A_{i+1,j} + (1-u)vA_{i,j+1} + uvA_{i+1,j+1}$$

where u is fractional part of x and v is fractional part of y, see Figure 51.

Relations used:

Eq. 34

$$x_0 = floor(x) \qquad x_1 = x_0 + 1$$
$$y_0 = floor(y) \qquad y_1 = y_0 + 1$$

$$A(x, y_0) = (x_1 - x)A(x_0, y_0) + (x - x_0)A(x_1, y_0)$$

and

$$A(x, y_1) = (x_1 - x)A(x_0, y_1) + (x - x_0)A(x_1, y_1)$$

so finally

$$A(x, y) = (y_1 - y)A(x, y_0) + (y - y_0)A(x, y_1)$$

Eq. 35

$$A(x, y) = (y_1 - y)(x_1 - x)A(x_0, y_0) + (y_1 - y)(x - x_0)A(x_1, y_0) + \\ + (y - y_0)(x_1 - x)A(x_0, y_1) + (y - y_0)(x - x_0)A(x_1, y_1)$$

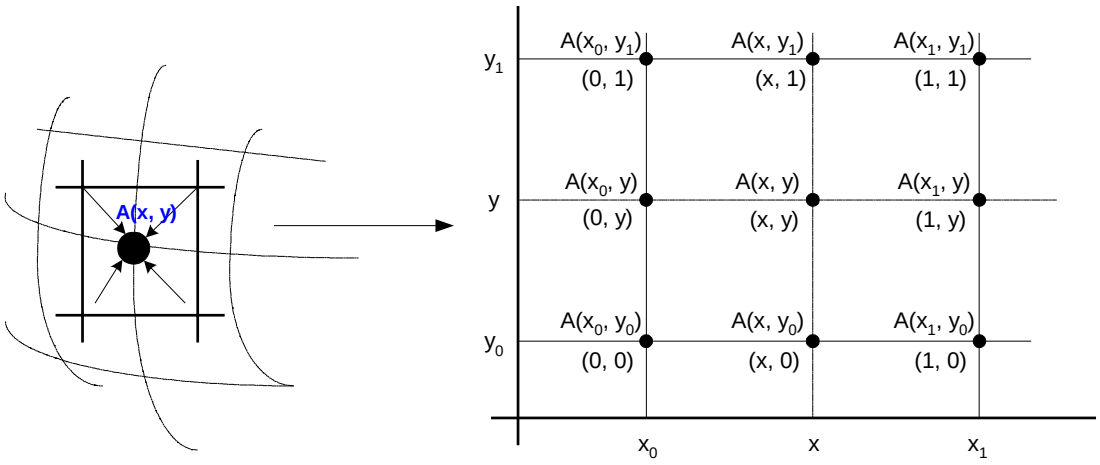

Figure 51. Bilinear interpolation

Appendix G. Film Calibration Behavior

Several calibration files, generated from calibration films exposed and scanned on different days by the RIT113 system, were analyzed.

Presented here are results obtained for different energies. Differences depending on the date of the scan are clearly visible, meaning that one calibration curve for particular energy would not probably do and showing very clearly why every time exposure of film is done calibration curve needs to be generated too. Results for only 2 energies are presented (4 and 10 MV), but analysis was done for 6 and 15 MV too showing the same amount of discrepancy. All the values compared come from the same machine.

4 MV				10 MV			
Dose (cGy)	**Date of Scan**	**Value Read by RIT113**	**% difference (min-max)**	**Dose (cGy)**	**Date of Scan**	**Value Read by RIT113**	**% difference (min-max)**
	10/23/2003	25			7/28/2003	/	NA
	9/8/2003	182			4/1/2003	/	
	2/10/2004	70			8/8/2003	/	
					6/23/2003	/	
					7/17/2003	33	
					03/18/2003	/	
101			86	112	2/11/2003	/	
					5/29/2003	/	
					2/3/2003	/	
					4/21/2003	/	
					1/5/2004	/	
					4/19/2004	/	
					4/14/2004	/	
	6/16/2003	91			7/28/2003	68	72
	10/23/2003	38			4/1/2003	/	
	7/2/2003	100			8/8/2003	/	
	5/29/2003	88			6/23/2003	51	
	2/10/2004	124			7/17/2003	53	
					03/18/2003	/	
84			69	93	2/11/2003	/	
					5/29/2003	45	
					2/3/2003	/	
					4/21/2003	/	
					1/5/2004	19	
					4/19/2004	/	
					4/14/2004	/	
	6/16/2003	167			7/28/2003	123	54
	7/2/2003	186			4/1/2003	94	
	9/19/2003	148			8/8/2003	81	
	5/29/2003	161			6/23/2003	92	
	2/10/2004	232			7/17/2003	102	
	9/8/2003	518			03/18/2003	91	
67			71	75	2/11/2003	79	
					5/29/2003	85	
					2/3/2003	82	
					4/21/2003	83	
					1/5/2004	56	
					4/19/2004	/	
					4/14/2004	/	

4 MV				10 MV			
Dose (cGy)	**Date of Scan**	**Value Read by RIT113**	**% difference (min-max)**	**Dose (cGy)**	**Date of Scan**	**Value Read by RIT113**	**% difference (min-max)**
50	6/16/2003 10/23/2003 7/2/2003 9/19/2003 12/3/2003 9/8/2003 5/29/2003 2/10/2004	379 149 391 469 376 975 366 498	84	56	7/28/2003 4/1/2003 8/8/2003 6/23/2003 7/17/2003 03/18/2003 2/11/2003 5/29/2003 2/3/2003 4/21/2003 1/5/2004 4/19/2004 4/14/2004	273 224 190 212 230 213 189 204 190 198 194 254 361	48
34	6/16/2003 10/23/2003 7/2/2003 9/19/2003 12/3/2003 9/8/2003 5/29/2003 2/10/2004	1037 423 1001 1128 1041 1698 977 1322	75	37	7/28/2003 4/1/2003 8/8/2003 6/23/2003 7/17/2003 03/18/2003 2/11/2003 5/29/2003 2/3/2003 4/21/2003 1/5/2004 4/19/2004 4/14/2004	774 673 559 624 631 695 522 633 586 619 649 741 981	43
17	6/16/2003 10/23/2003 7/2/2003 9/19/2003 12/3/2003 9/8/2003 5/29/2003 2/10/2004	2106 1612 2101 2098 2075 2309 2099 2179	30	19	7/28/2003 4/1/2003 8/8/2003 6/23/2003 7/17/2003 03/18/2003 2/11/2003 5/29/2003 2/3/2003 4/21/2003 1/5/2004 4/19/2004 4/14/2004	1954 1950 1808 1857 1880 1946 1787 1857 1833 1905 1825 1979 2117	16
0	6/16/2003 10/23/2003 7/2/2003 9/19/2003 12/3/2003 9/8/2003 5/29/2003 2/10/2004	3434 3138 3367 3369 3333 3250 3413 3280	9	0	7/28/2003 4/1/2003 8/8/2003 6/23/2003 7/17/2003 03/18/2003 2/11/2003 5/29/2003 2/3/2003 4/21/2003 1/5/2004 4/19/2004 4/14/2004	3323 3483 3442 3360 3213 3444 3440 3394 3484 3470 3420 3522 3544	9

Appendix H. CR Plate Calibration Values

Calibration curve values are presented hereafter together with the exponential equations generated as a trendline fit through the data points measured for different maximum values of monitor units delivered.

Different color means that exposure was done on different day.

4 MV

MU	Dose (cGy)	RGB	MU	Dose (cGy)	RGB	MU	Dose (cGy)	RGB	MU	Dose (cGy)	RGB
1	0.84	162	31	25.98	72	67	56.15	54	105	87.99	43
2	1.68	145	32	26.82	71	68	56.99	52	106	88.83	44
2	1.68	149	33	27.66	71	69	57.83	54	107	89.67	42
3	2.51	136	34	28.49	71	70	58.66	53	108	90.51	43
4	3.35	129	35	29.33	69	70	58.66	51	109	91.35	45
5	4.19	122	35	29.33	71	71	59.50	51	110	92.19	43
5	4.19	116	36	30.17	69	72	60.34	51	110	92.19	44
5	4.19	123	37	31.01	68	73	61.18	53	111	93.02	44
6	5.03	119	38	31.85	66	74	62.02	50	112	93.86	43
7	5.87	115	39	32.68	66	75	62.85	52	113	94.70	42
7	5.87	114	40	33.52	66	76	63.69	52	114	95.54	44
8	6.70	111	40	33.52	68	77	64.53	49	115	96.38	44
9	7.54	108	40	33.52	64	78	65.37	50	116	97.21	42
10	8.38	104	41	34.36	64	79	66.21	51	117	98.05	43
10	8.38	100	42	35.20	64	80	67.04	48	118	98.89	43
10	8.38	105	43	36.04	64	80	67.04	51	119	99.73	41
11	9.22	101	44	36.87	62	81	67.88	49	120	100.57	42
12	10.06	100	45	37.71	62	82	68.72	51	120	100.57	43
13	10.89	97	45	37.71	64	83	69.56	49	121	101.40	42
14	11.73	94	46	38.55	62	84	70.40	50	122	102.24	40
15	12.57	94	47	39.39	60	85	71.23	49	123	103.08	41
15	12.57	95	48	40.23	60	86	72.07	48	124	103.92	42
16	13.41	92	49	41.06	60	87	72.91	48	125	104.76	39
17	14.25	89	50	41.90	58	88	73.75	49	126	105.59	40
18	15.08	88	50	41.90	61	89	74.59	47	130	108.95	41
19	15.92	84	50	41.90	61	90	75.42	48			
20	16.76	82	51	42.74	58	90	75.42	47			
20	16.76	85	52	43.58	60	91	76.26	48			
20	16.76	85	53	44.42	58	92	77.10	46			
21	17.60	82	54	45.25	57	93	77.94	46			
22	18.44	81	55	46.09	60	94	78.78	47			
23	19.28	79	56	46.93	58	95	79.61	45			
24	20.11	79	57	47.77	58	96	80.45	45			
25	20.95	79	58	48.61	58	97	81.29	46			
25	20.95	80	59	49.44	56	98	82.13	44			
26	21.79	78	60	50.28	57	99	82.97	44			
27	22.63	77	61	51.12	57	100	83.80	46			
28	23.47	74	62	51.96	56	100	83.80	47			
29	24.30	73	63	52.80	56	101	84.64	43			
30	25.14	73	64	53.63	56	102	85.48	45			
30	25.14	74	65	54.47	54	103	86.32	44			
30	25.14	75	66	55.31	55	104	87.16	42			

6 MV

MU	Dose (cGy)	RGB	MU	Dose (cGy)	RGB	MU	Dose (cGy)	RGB	MU	Dose (cGy)	RGB
1	0.87	167	28	24.30	79	62	53.82	58	100	86.80	53
1	0.87	163	29	25.17	78	63	54.68	57	101	87.67	48
2	1.74	151	30	26.04	77	64	55.55	59	102	88.53	48
3	2.60	143	30	26.04	80	65	56.42	57	103	89.40	49
3	2.60	140	30	26.04	80	66	57.29	58	104	90.27	47
4	3.47	133	31	26.91	76	67	58.16	56	105	91.14	47
5	4.34	127	32	27.78	74	68	59.02	54	106	92.01	49
5	4.34	122	33	28.64	74	69	59.89	55	107	92.87	47
5	4.34	129	34	29.51	74	70	60.76	56	108	93.74	47
6	5.21	124	35	30.38	72	70	60.76	60	109	94.61	54
7	6.08	119	35	30.38	76	71	61.63	54	110	95.48	53
7	6.08	120	36	31.25	71	72	62.50	54	111	96.35	53
8	6.94	116	37	32.12	74	73	63.36	61	112	97.21	53
9	7.81	113	38	32.98	72	74	64.23	59	113	98.08	51
9	7.81	113	39	33.85	73	75	65.10	60	114	98.95	52
10	8.68	108	40	34.72	70	76	65.97	60	115	99.82	52
10	8.68	107	40	34.72	72	77	66.84	58	116	100.69	51
11	9.55	104	40	34.72	74	78	67.70	59	117	101.55	51
12	10.42	103	41	35.59	68	79	68.57	59	118	102.42	52
12	10.42	107	42	36.46	69	80	69.44	57	119	103.29	50
13	11.28	101	43	37.32	69	80	69.44	58	120	104.16	51
14	12.15	98	44	38.19	67	81	70.31	58	121	105.03	52
15	13.02	97	45	39.06	67	82	71.18	54	122	105.89	49
15	13.02	98	45	39.06	69	83	72.04	51	123	106.76	50
15	13.02	101	46	39.93	68	84	72.91	52	124	107.63	51
16	13.89	97	47	40.80	66	85	73.78	51	125	108.50	49
17	14.76	95	48	41.66	67	86	74.65	48	126	109.37	49
17	14.76	98	49	42.53	65	87	75.52	50	127	110.23	50
18	15.62	94	50	43.40	64	88	76.38	51	128	111.10	48
19	16.49	93	50	43.40	68	89	77.25	48	129	111.97	49
19	16.49	94	51	44.27	63	90	78.12	49	130	112.84	48
20	17.36	91	52	45.14	64	90	78.12	54	131	113.71	47
20	17.36	90	53	46.00	62	91	78.99	53	132	114.57	48
20	17.36	90	54	46.87	62	92	79.86	51	133	115.44	48
21	18.23	91	55	47.74	63	93	80.72	51	134	116.31	48
22	19.10	88	56	48.61	62	94	81.59	51	135	117.18	48
23	19.96	87	57	49.48	62	95	82.46	49			
24	20.83	86	58	50.34	60	96	83.33	49			
25	21.70	85	59	51.21	58	97	84.20	51			
25	21.70	84	60	52.08	59	98	85.06	49			
26	22.57	84	60	52.08	63	99	85.93	49			
27	23.44	83	61	52.95	59	100	86.80	50			

10 MV

MU	Dose (cGy)	RGB	MU	Dose (cGy)	RGB	MU	Dose (cGy)	RGB
1	0.93	166	25	23.33	82	67	62.53	57
1	0.93	165	26	24.26	81	68	63.46	55
2	1.87	150	27	25.20	80	69	64.39	56
2	1.87	149	28	26.13	80	70	65.33	57
3	2.80	141	29	27.06	79	71	66.26	55
3	2.80	140	30	28.00	78	72	67.19	55
4	3.73	133	31	28.93	77	73	68.12	57
4	3.73	133	32	29.86	76	74	69.06	55
5	4.67	126	33	30.80	75	75	69.99	56
5	4.67	127	34	31.73	75	76	70.92	56
6	5.60	123	35	32.66	73	77	71.86	54
6	5.60	122	36	33.60	73	78	72.79	55
7	6.53	118	37	34.53	73	79	73.72	55
7	6.53	118	38	35.46	72	80	74.66	53
8	7.47	115	39	36.40	71	81	75.59	54
8	7.47	114	40	37.33	70	82	76.52	54
9	8.40	112	41	38.26	68	83	77.46	53
9	8.40	111	42	39.20	68	84	78.39	53
10	9.33	107	43	40.13	68	85	79.32	53
10	9.33	108	44	41.06	67	86	80.26	52
11	10.27	104	45	41.99	66	87	81.19	52
11	10.27	106	46	42.93	68	88	82.12	53
12	11.20	103	47	43.86	67	89	83.06	51
12	11.20	104	48	44.79	67	90	83.99	52
13	12.13	101	49	45.73	66	91	84.92	52
13	12.13	102	50	46.66	65	92	85.86	50
14	13.07	98	51	47.59	65	93	86.79	52
14	13.07	100	52	48.53	66	94	87.72	51
15	14.00	97	53	49.46	64	95	88.66	50
15	14.00	98	54	50.39	64	96	89.59	50
16	14.93	96	55	51.33	63	97	90.52	51
16	14.93	96	56	52.26	61	98	91.46	49
17	15.86	94	57	53.19	61	99	92.39	49
17	15.86	94	58	54.13	61	100	93.32	51
18	16.80	92	59	55.06	59	101	94.25	49
18	16.80	92	60	55.99	59	102	95.19	50
19	17.73	91	61	56.93	60	103	96.12	50
20	18.66	88	62	57.86	58	104	97.05	48
21	19.60	87	63	58.79	57	105	97.99	48
22	20.53	86	64	59.73	58	106	98.92	49
23	21.46	84	65	60.66	57	107	99.85	47
24	22.40	83	66	61.59	58	108	100.79	48

4 MV

monitor units	SpSc(5x5)	TMR(5,5)	Dose (cGy)
20	0.946	0.865	16.8
40	0.946	0.865	33.5
60	0.946	0.865	50.3
80	0.946	0.865	67.0
100	0.946	0.865	83.8
120	0.946	0.865	100.6

Equations used depending on the maximum dose delivered (that is obtained from the plan image) and MUs read from the table above:

up to 20

$$Dose(cGy) = 403.33e^{-0.0374RGB}$$

up to 40

$$Dose(cGy) = 381.79e^{-0.037RGB}$$

up to 60

$$Dose(cGy) = 386.42e^{-0.0371RGB}$$

up to 70

$$Dose(cGy) = 400.15e^{-0.0374RGB}$$

up to 80

$$Dose(cGy) = 410.37e^{-0.0377RGB}$$

up to 100

$$Dose(cGy) = 435.74e^{-0.0383RGB}$$

up to 120

$$Dose(cGy) = 460.28e^{-0.0389RGB}$$

up to 130

$$Dose(cGy) = 467.57e^{-0.039RGB}$$

6 MV

monitor units	SpSc(5x5)	TMR(5,5)	Dose (cGy)
20	0.942	0.894	17.4
40	0.942	0.894	34.7
60	0.942	0.894	52.1
80	0.942	0.894	69.4
100	0.942	0.894	86.8
120	0.942	0.894	104.2

Equations used depending on the maximum dose delivered (that is obtained from the plan image) and MUs read from the table above:

up to 20

$$Dose(cGy) = 617.39e^{-0.0391RGB}$$

up to 40

$$Dose(cGy) = 512.59e^{-0.0376RGB}$$

up to 50

$$Dose(cGy) = 500.13e^{-0.0374RGB}$$

up to 60

$$Dose(cGy) = 490.38e^{-0.0372RGB}$$

up to 70

$$Dose(cGy) = 484.19e^{-0.0371RGB}$$

up to 80

$$Dose(cGy) = 516.49e^{-0.0377RGB}$$

up to 90

$$Dose(cGy) = 515.69e^{-0.0377RGB}$$

up to 100

$$Dose(cGy) = 529.55e^{-0.0379RGB}$$

up to 110

$$Dose(cGy) = 543.19e^{-0.0382RGB}$$

up to 120

$$Dose(cGy) = 578.72e^{-0.0388RGB}$$

up to 135

$$Dose(cGy) = 624.58e^{-0.0395RGB}$$

10 MV

monitor units	SpSc(5x5)	TMR(5,5)	Dose (cGy)
20	0.935	0.950	18.7
40	0.935	0.950	37.3
50	0.946	0.865	41.9
60	0.935	0.950	56.0
70	0.935	0.950	65.3
80	0.935	0.950	74.7
100	0.935	0.950	93.3
120	0.935	0.950	112.0

Equations used depending on the maximum dose delivered (that is obtained from the plan image) and MUs read from the table above:

up to 20

$$Dose(cGy) = 598.15e^{-0.0385RGB}$$

up to 40

$$Dose(cGy) = 528.31e^{-0.0375RGB}$$

up to 50

$$Dose(cGy) = 524.46e^{-0.0375RGB}$$

up to 60

$$Dose(cGy) = 529.38e^{-0.0375RGB}$$

up to 70

$$Dose(cGy) = 526.68e^{-0.0375RGB}$$

up to 80

$$Dose(cGy) = 539.00e^{-0.0377RGB}$$

up to 90

$$Dose(cGy) = 554.53e^{-0.038RGB}$$

up to 108

$$Dose(cGy) = 583.37e^{-0.0384RGB}$$

4 MV curves

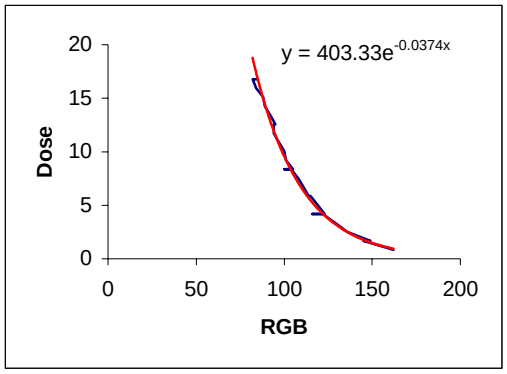

Up to 20 MU

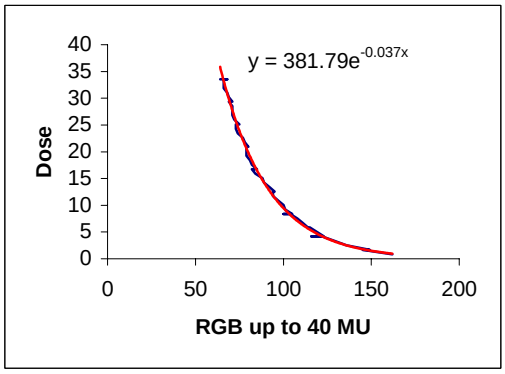

Up to 40 MU

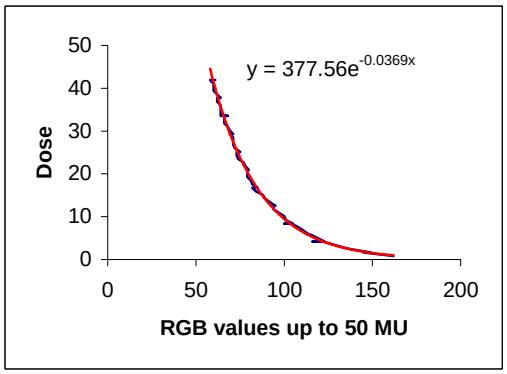

Up to 50 MU

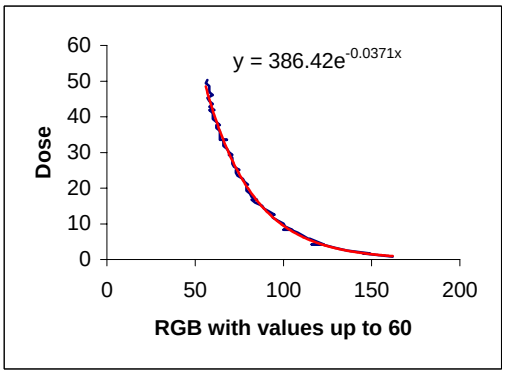

Up to 60 MU

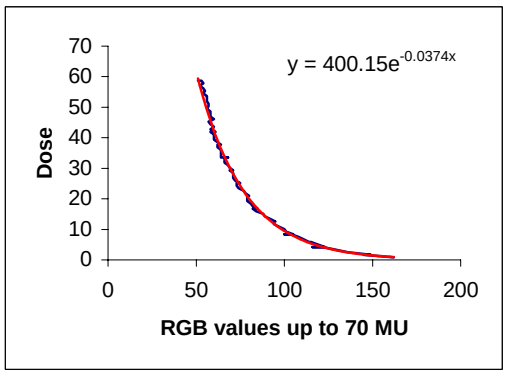

Up to 70 MU

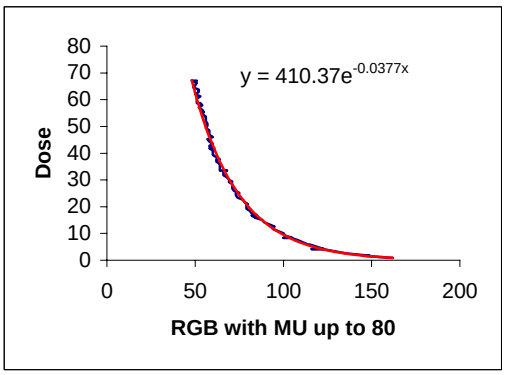

Up to 80 MU

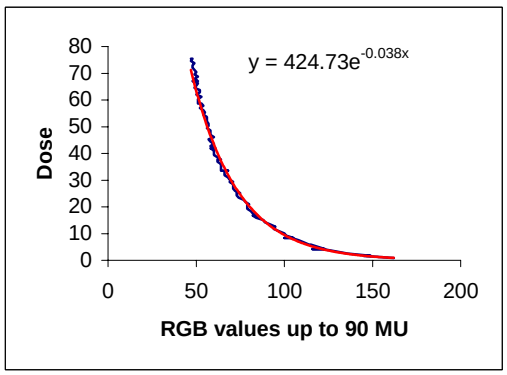

Up to 90 MU

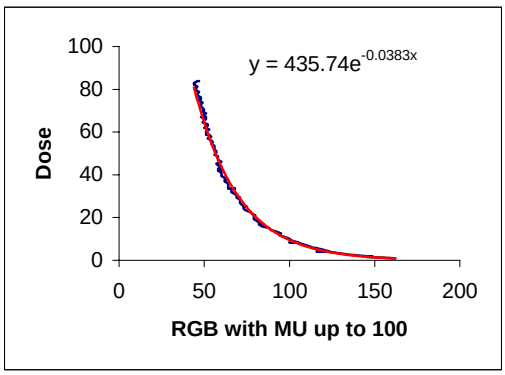

Up to 100 MU

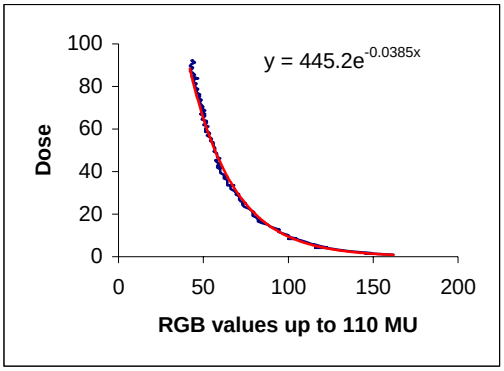

Up to 110 MU

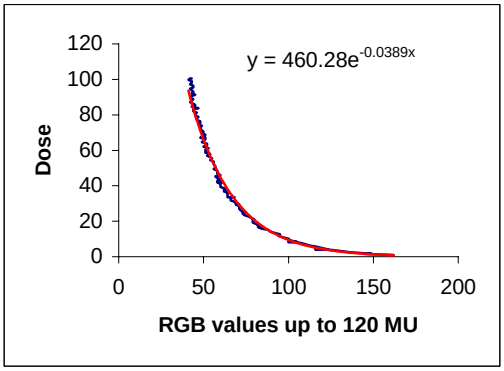

Up to 120 MU

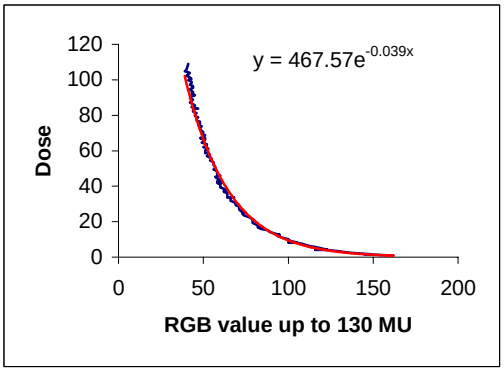

Up to 130 MU

6 MV curves

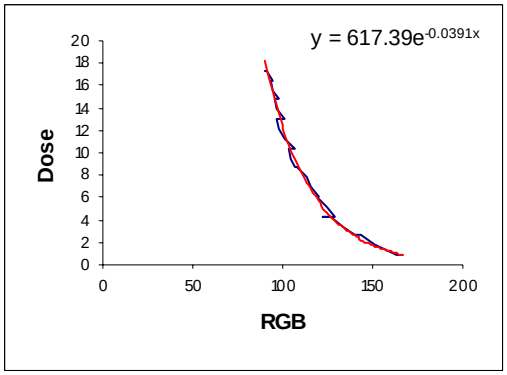

Up to 20 MU

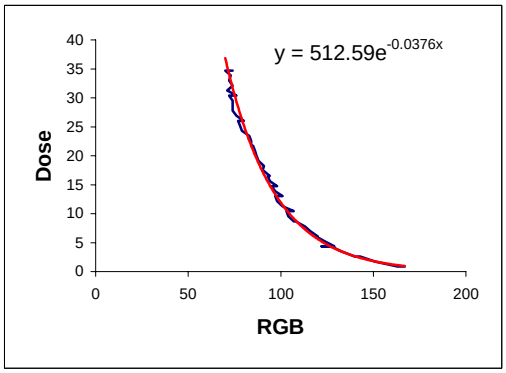

Up to 40 MU

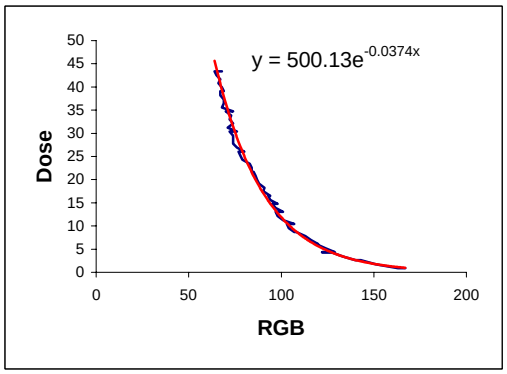

Up to 50 MU

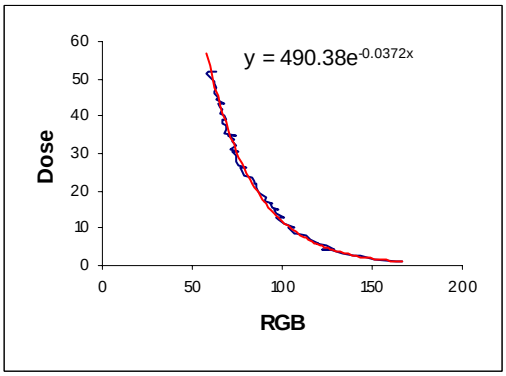

Up to 60 MU

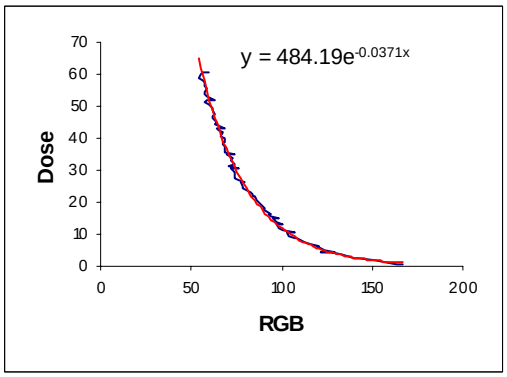

Up to 70 MU

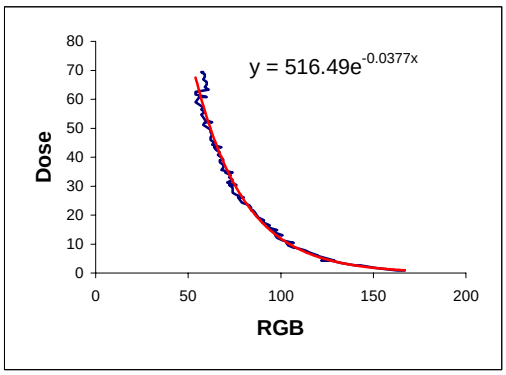

Up to 80 MU

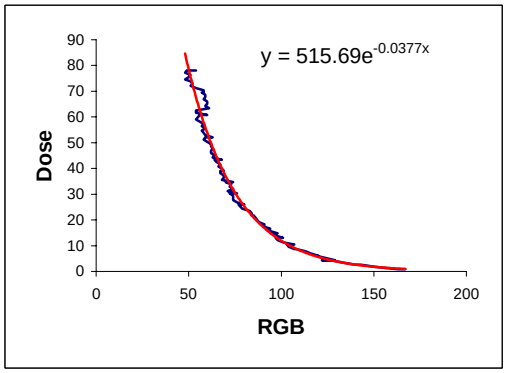

Up to 90 MU

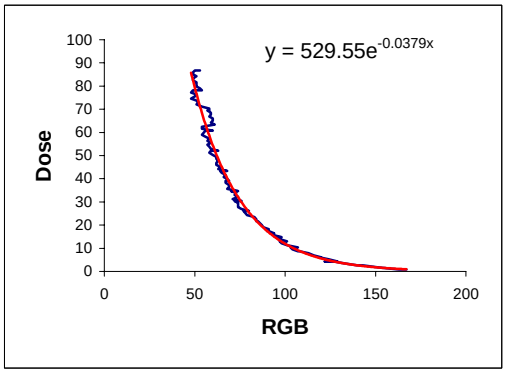

Up to 100 MU

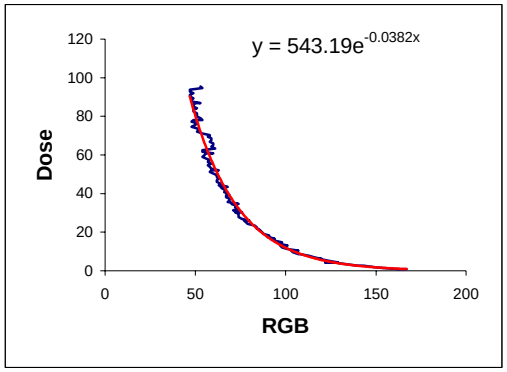

Up to 110 MU

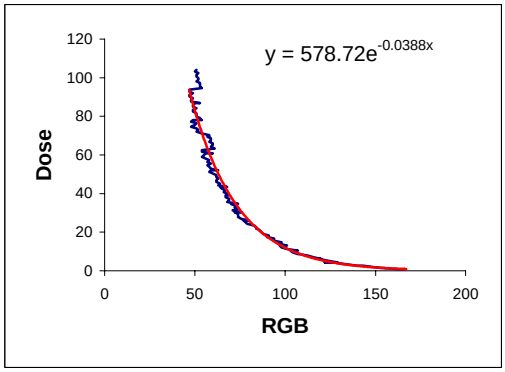

Up to 120 MU

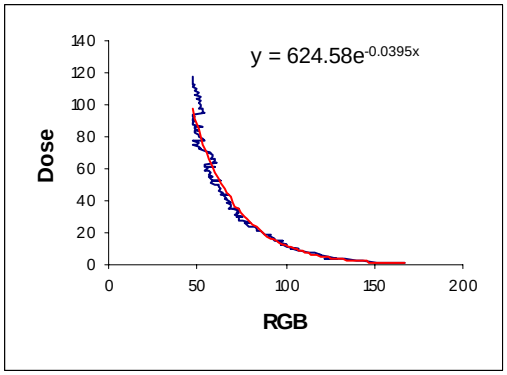

Up to 135 MU

10 MV curves

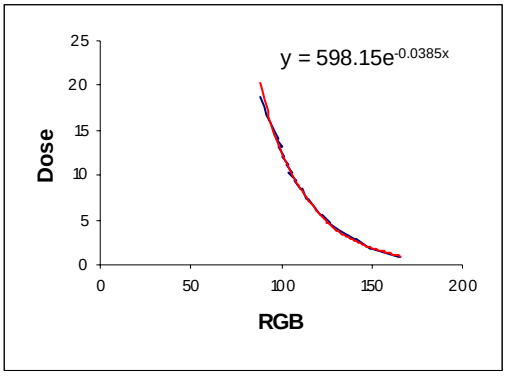

Up to 20 MU

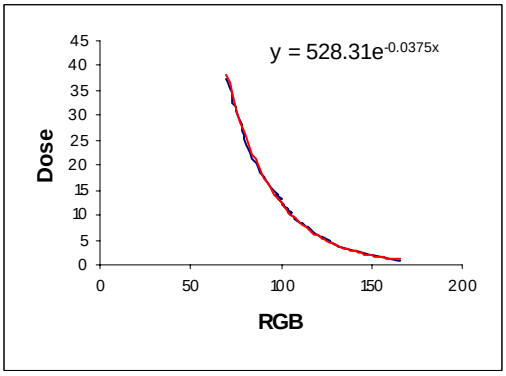

Up to 40 MU

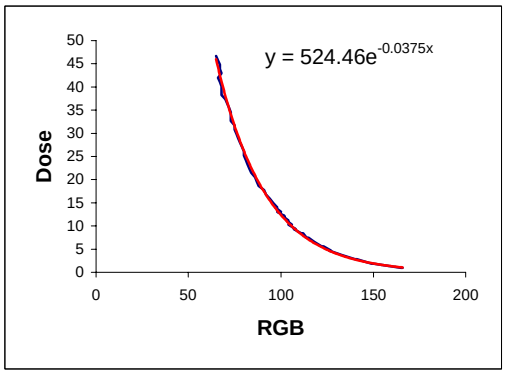

Up to 50 MU

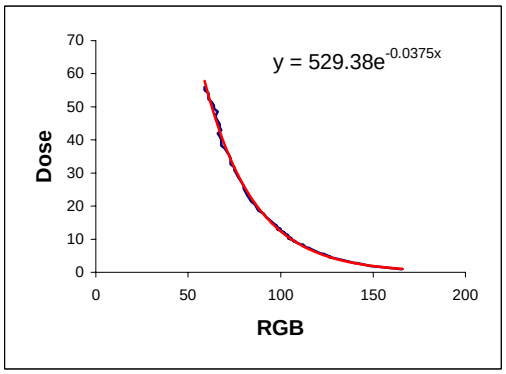

Up to 60 MU

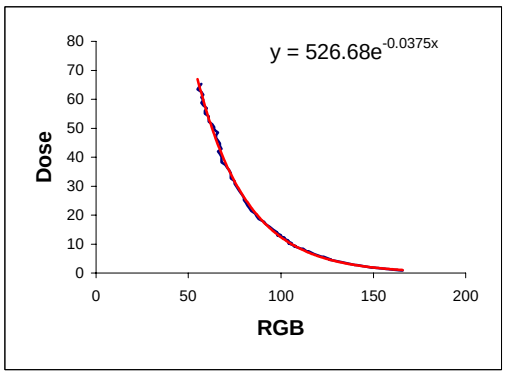

Up to 70 MU

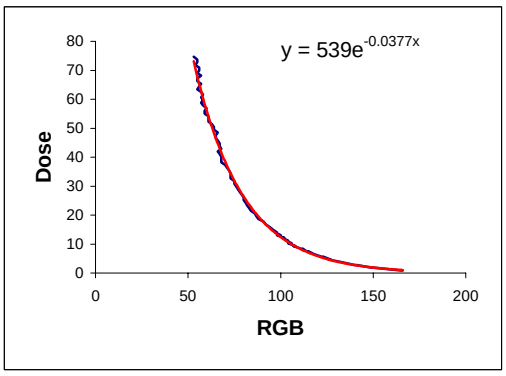

Up to 80 MU

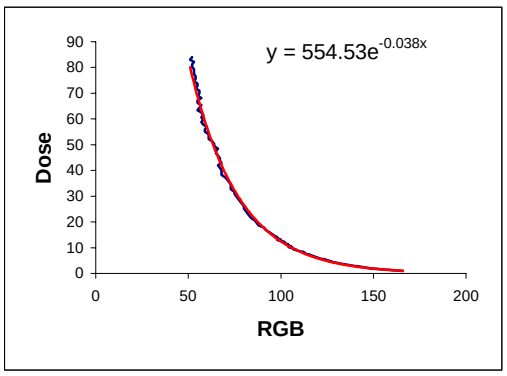

Up to 90 MU

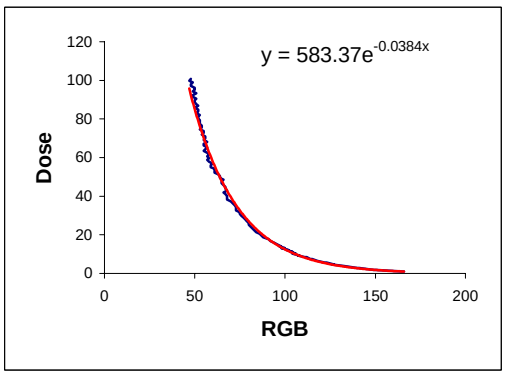

Up to 108 MU

Graph below shows comparison of the calibration curves for three different energies using the data points measured.

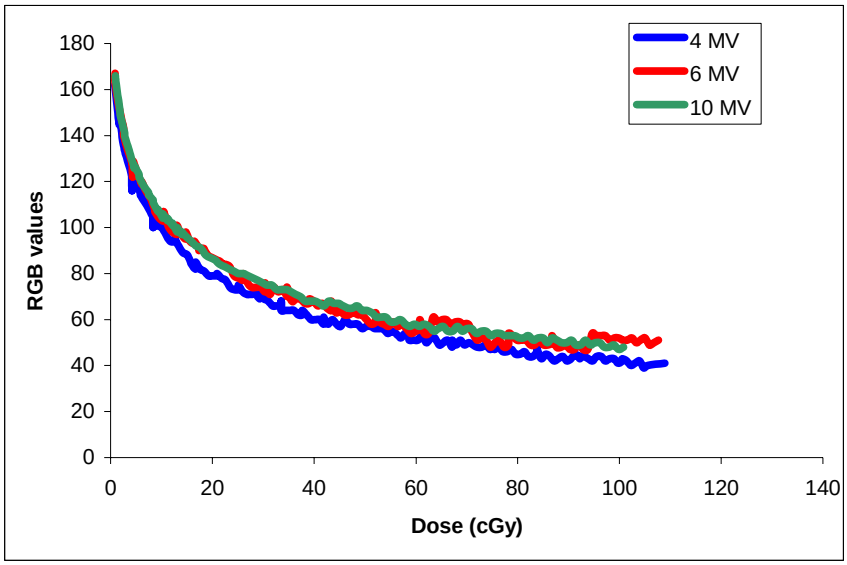

Graph below shows comparison of the calibration curves for three different energies using the data points calculated with the exponential equation for the maximum number of monitor units delivered, these are the curves actually used for CR plate's calibration in developed IMRT analysis program.

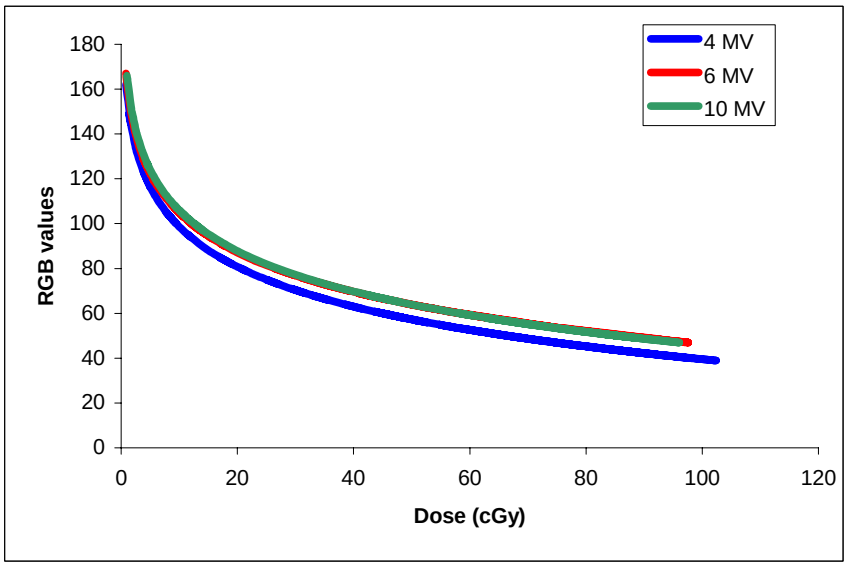

Vita

Ines-Ana Jurkovic is from Croatia, Europe. She studied at Faculty of Electrical Engineering and Computing, University of Zagreb, Croatia. She got her bachelor degree in electrical engineering in 1992. She got master's degree in nuclear engineering in 1998 at the Faculty of Electrical Engineering and Computing, University of Zagreb, Croatia. Since that time she was working as researcher and as a member of deterministic safety group using RELAP5 computer code, doing preparation of transient analysis used for training of the plant specific simulator, severe accident calculation, core calculation, environmental quality calculations, Departure from Nucleate Boiling rate calculation, etc. As emergency planner she was working in field of emergency preparedness and accident management, doing analysis of current status of infrastructure and equipment necessary in case of a radiological or nuclear emergency. She was involved in reviewing and developing national policy and planning basis definition, in the nuclear condition assessment through the accident classification and determination of the core conditions, release route and release conditions, research of the environmental pathways and consequences especially through the use of the sophisticated computer codes like MACCS and COSYMA.

As a Public Relation Officer she was working with IAEA fellows regarding their scientific and social activities, she was involved in training courses coordination and related responsibilities, communication tasks and activities. As consultant she was involved in Contingency and Operational Plan development (Radiation Incident), Dose and Shielding Calculations, Risk Analysis.

Other work experience in February-July 1998 includes work in the Department of the Environmental Quality, Louisiana Radiation Protection Division, USA, on emergency planning, response and preparedness issues.

Awards received include Award for Excellent Work in technical field from the Ecole Polyvalente Technique "Armand Corbeil", Canada, 1985; "Josip Lončar" award from the Faculty of Electrical Engineering and Computing, Croatia, 1993; Honorary Mayor-President award from the city of Baton Rouge, Louisiana, 1998; Certificate of Appreciation for providing the opportunity to exchange the knowledge and experience of the State of Louisiana and the Republic of Croatia, The Department of Environmental Quality, Louisiana, USA, 1998; Certificate of Appreciation for the contribution as a speaker to the 9th annual National Radiological Emergency Preparedness (NREP) conference, Baton Rouge, USA, 1999; First Place award on the Young Author Contest, 3rd International Conference on Nuclear Option in Countries with Small and Medium Electricity Grids, Croatia, 2000.

She published numerous papers at various conferences. Mostly in area of nuclear engineering, specifically dealing with the safety analysis. She was a member of European Nuclear Society (ENS), Croatian Nuclear Society (HND), Croatian Technical Support Center for the case of the nuclear accident, President of the Croatian Nuclear Society (HND) Young Generation Network, HND Public Relation officer, Member of the HND conferences Organizing Committee, etc.

Having started in fall 2002, she has been taking the medical physics program (Master's Degree) at Louisiana State University, Baton Rouge Louisiana. She expects to graduate in December 2004.